

WAVE PROPAGATION IN PERIODIC ACOUSTIC
METAMATERIALS: FROM 1D TO 3D

Thesis by
Gunho Kim

In Partial Fulfillment of the Requirements for the
Degree of
Doctor of Philosophy in Mechanical Engineering

The logo for the California Institute of Technology (Caltech), featuring the word "Caltech" in a bold, orange, sans-serif font.

CALIFORNIA INSTITUTE OF TECHNOLOGY
Pasadena, California

2023
Defended January 13, 2023

© 2023

Gunho Kim

ORCID: 0000-0003-1796-0908

All rights reserved

ACKNOWLEDGEMENTS

I would like to express my gratitude to my Ph.D. advisor, Professor Chiara Daraio. Thank you for guiding me throughout my scientific explorations, providing me with a large degree of freedom, helping me become a more independent researcher, and sharing your valuable insights with me throughout the journey.

I would also like to extend my gratitude to Professor Mikhail G. Shapiro for his guidance and for serving as the Chair of my Thesis Committee. You always welcomed me and made me feel like I'm one of your own group members. I am also grateful to Professor Julia Greer and Professor Domniki Asimaki for serving on my thesis committee, and to Professor Guruswami Ravichandran for serving on my candidacy committee.

To Dr. Paolo Celli, Dr. Antonio Palermo, and Dr. Carlos M. Portela, your support and encouragement helped make my transition to graduate school smooth and successful, and I am grateful to have had them as mentors. Your students are equally fortunate as I was to have such dedicated and talented individuals guiding them. I extend my sincere gratitude to Dr. Max Kudisch, Dr. Jinwoong Cha, Dr. Israel Kellersztein, and Dr. Sai Sharan Injeti for your invaluable contributions to my academic journey. Academic discussions with you all have been instrumental in shaping my research and understanding of the field.

Thank you to Dr. Claire Rabut, Bill Ling, and Dr. Di Wu for sharing your knowledge and expertise in collaboration with me. It would have been impossible for me to complete my projects without your help. I am also grateful to Kaila for being a great mentee during the summer of 2021 and throughout the following year.

I would like to thank everyone in the Daraio group, not only for the expertise and mentorship you have provided me, but also for being great labmates over the past five years. I am especially grateful to my office mates in B255, and to Carolina for her administrative support.

My life has been much more joyful thanks to my dearest friends in the MCE department, Nachi, Widi, Taeyong, Leah, Alex, Adrian, and Shi Ning. Thank you all for making the Gates-Thomas Laboratory feel like not only a workplace but also my second home. I have greatly enjoyed every moment spent with you all. It has been a pleasure being a part of Caltech's Korean community. I deeply wish for all of you to achieve your goals and aspirations in this foreign soil.

So-yoon, I love you. You have been a great part of my life for the last five years in both personal and academic lives. I look forward to continuing our journey together wherever it may lead us. To my dad, mom, and my sister, I thank you for your never-ending, unyielding love and support. I am truly lucky to have you as my family.

ABSTRACT

Wave propagation in periodic structures has been studied for centuries; for example, Newton derived the velocity of sound based on a linear lattice. Recently, advanced manufacturing techniques have led to the fabrication of geometrically complex architected materials with acoustic properties unattainable by their constituent materials. Such rationally designed structures are often called acoustic metamaterials and they can be engineered to transmit, block, amplify, or redirect acoustic waves. Subwavelength building blocks, typically periodic (but not necessarily so), can be assembled into effectively continuous materials to manipulate dispersive properties of vibrational waves in ways that differ substantially in conventional media. This thesis investigates rationally designed acoustic metamaterials, ranging from 1D to 3D, and how acoustic wave propagation can be controlled by these artificially structured composite materials for ultrasound-related biomedical applications.

I first explore 1D wave propagation in acoustic metamaterials to study the basic mechanics and relevant analysis skills. Bio-inspired helical mechanical metamaterials are designed and their normal modes are investigated. I demonstrate the ability to vary the acoustic properties of the helical metamaterials by perturbing the geometrical structure and mass distribution. By locally adding eccentric and denser elements in the unit cells, I change the moment of inertia of the system and introduce centro-asymmetry. This allows me to control the degree of mode coupling and the width of subwavelength band gaps in the dispersion relation, which are the product of enhanced local resonance hybridization.

Then I study 2D wave propagation in microlattice acoustic metamaterials for ultrasound manipulation. When coupled with pressure waves in the surrounding fluid, the dynamic behavior of microlattices in the long wavelength limit can be explained in the context of Biot's theory of poroelasticity. I exploit elastoacoustic wave propagation within 3D-printed polymeric microlattices to design a gradient refractive index lens for underwater wave focusing. A modified Luneburg lens index profile adapted for ultrasonic wave lensing is demonstrated via the finite element method and underwater testing, showcasing a computationally efficient poroelasticity-based design approach that enables accelerated design of acoustic wave manipulation devices.

Lastly, I show that tailorable 3D wave propagation can be achieved based on the

findings from the previous chapters. Functional ultrasound imaging enables sensitive, high-resolution imaging of neural activity in freely behaving animals and human patients. However, the skull acts as an aberrant and absorbing layer for sound waves, leading to most functional ultrasound experiments being conducted after skull removal. A microscale 2-photon polymerization technique is adopted to fabricate a conformal acoustic window with a high stiffness-to-density ratio and sonotransparency. Long-term biocompatibility and lasting signal sensitivity are demonstrated over a long period of time (> 4 months) by conducting ultrasound imaging in mouse models implanted with the metamaterial skull prosthesis.

PUBLISHED CONTENT AND CONTRIBUTIONS

This thesis has been directly adapted from:

- 1) G. Kim, C.M. Portela, P. Celli, A. Palermo, & C. Daraio. "Poroelastic Microlattices for Underwater Wave Focusing". *Extreme Mechanics Letters* **49**, 101499, (2021), <https://doi.org/10.1063/5.0106740>.
CONTRIBUTIONS: Participated in the conception of the project, designed and characterized the models via finite element analysis, fabricated the samples, conducted the transmission experiments, analyzed the data, and wrote the manuscript.
- 2) G. Kim, K.M.Y. Coimbra, & C. Daraio. "Mode Hybridization in DNA-Inspired Helical Metamaterials with Variable Centro-asymmetry". *Applied Physics Letters* **121**, 072201 (2022), <https://doi.org/10.1016/j.apl.2021.101499>.
CONTRIBUTIONS: Conceived the project and generated the idea, designed and characterized the models via finite element analysis, fabricated the samples, conducted the transmission experiments, analyzed the data, and wrote the manuscript.
- 3) G. Kim, C. Rabut, B. Ling, M.G. Shapiro, & C. Daraio. "Conformal Acoustic Window for the Skull Based on Microscale Metamaterials". *In preparation*.
CONTRIBUTIONS: Participated in the conception of the project, designed and characterized the models via finite element analysis, fabricated the samples, conducted the mechanical characterization both under quasi-static and dynamic loading, participated in the animal experiments, analyzed the data, and wrote the manuscript.

TABLE OF CONTENTS

Acknowledgements	iii
Abstract	v
Published Content and Contributions	vii
Table of Contents	viii
List of Illustrations	x
List of Tables	xx
Nomenclature	xxi
Chapter I: Introduction	1
1.1 Research objectives	1
1.2 Research motivation	1
1.3 Research approach, methods, and challenges	4
1.4 Chapter outlook	6
Chapter II: Acoustic metamaterials	13
2.1 Chapter preamble	13
2.2 1D Mass and Spring System and dispersion relation	13
2.3 Expansion to higher dimensions	17
2.4 Acoustic metamaterials and material parameters	21
2.5 Types of acoustic metamaterials	22
Chapter III: 1D wave propagation in acoustic metamaterials: helical metamaterials and mode hybridization	36
3.1 Chapter summary	36
3.2 Introduction	36
3.3 DNA-inspired design of the helical metamaterials (HMMs)	37
3.4 Effect of centrosymmetry on the acoustic properties of the HMMs	39
3.5 Experimental validation of the acoustic band gap	46
3.6 Conclusions	49
Chapter IV: 2D wave propagation in acoustic metamaterials: water-saturated beam microlattices	52
4.1 Chapter summary	52
4.2 Introduction	53
4.3 Effective refractive index of the water-filled microlattices	54
4.4 Dispersion relation of the water-filled microlattices	60
4.5 Gradient-index Luneburg lens design	66
4.6 Underwater experiments of the Luneburg lens	69
4.7 Conclusions	70
Chapter V: 3D wave propagation in acoustic metamaterials: plate microlattices in water environment	72
5.1 Chapter Summary	72
5.2 Introduction	73

5.3	Concept	75
5.4	Quasi-static characterization of the metaskull	77
5.5	Dynamic characterization of the metaskull	83
5.6	In vivo experiments for cranial window characterization	93
5.7	Survival test	97
5.8	Conclusions	98
Chapter VI: Summary and Outlook		104
6.1	Summary	104
6.2	Open questions and future work	105

LIST OF ILLUSTRATIONS

<i>Number</i>	<i>Page</i>
2.1 Monoatomic infinite 1-dimensional mass and spring chain. a , Schematics of 1d monoatomic chain. b , The dispersion curve of 1D monoatomic chain in the first Brillouin zone. ω_0 is the cutoff frequency, defined as $\sqrt{K/M}$	13
2.2 Diatomic infinite 1-dimensional mass and spring chain. a , Schematics of 1d diatomic chain. b , The dispersion curve of 1D diatomic chain in the first Brillouin zone.	16
2.3 Normal modes of 1D monoatomic and diatomic chains. a , Normal mode of 1d monoatomic chain. b , First normal mode of 1d diatomic chain. c , Second normal mode of 1d diatomic chain.	17
2.4 2D periodic acoustic metamaterials a , The direct lattices with \vec{a}_1, \vec{a}_2 as primitive vectors. b , The reciprocal lattices of the triangular Bravais lattice with \vec{b}_1, \vec{b}_2 as primitive vectors.	18
2.5 3D acoustic metamaterials a , The direct lattices (FCC) with $\vec{a}_1, \vec{a}_2,$ and \vec{a}_3 as primitive vectors. b , The reciprocal lattices (BCC) of the triangular Bravais lattice with $\vec{b}_1, \vec{b}_2,$ and \vec{b}_3 as primitive vectors.	19
2.6 Irreducible Brillouin zone and corresponding dispersion curve. a , Schematics of 1d monoatomic chain. b , The dispersion curve of 1D monoatomic chain in the first Brillouin zone. ω_0 is the cutoff frequency, defined as $\sqrt{K/M}$	20
2.7 Phononic crystals a , Kinematic sculpture as an example of phononic crystals. Transmission plot shows attenuations in specific direction [11]. b , Array of lead spheres coated with silicone rubber as an example of phononic crystals. Attenuation dips in the transmission curve coincide with the band gaps in the dispersion curve [2]. c , Pressure profiles show the focusing of sound in the presence of phononic crystals [5]	23

- 2.8 **Membrane-based acoustic metamaterials a**, The first four mode shapes of the membrane unit without external loading [21]. **b**, Schematic of the 2D metamaterial layer composed of chambers divided by membranes [22]. **c**, Simulated and measured transmission curves with respect to the mode shapes at the eigenfrequencies [23]. 24
- 2.9 **Acoustic metamaterials with Helmholtz resonators a**, Schematics of Helmholtz resonator-based acoustic metamaterials. The effective stiffness of the metamaterials is negative at specific frequency range [7]. **b**, Schematic views of an acoustic metamaterial plate periodically embedded with resonators [28]. **c**, Acoustic metamaterials can be composed of different configurations using multiple Helmholtz resonators [29]. 25
- 2.10 **Acoustic metamaterials with negative parameters a**, The effective mass of the mass-in-mass lattice becomes negative across the narrow frequency range, and it affects the attenuation coefficients of the acoustic metamaterials [32]. **b**, The effective modulus of the split hollow sphere is below zero around 5 kHz, significantly affecting the wave properties [33]. 26
- 2.11 **Chiral acoustic metamaterials a**, Various configurations of 2D chiral acoustic metamaterials [37]. **b**, Microscale 3D chiral acoustic metamaterials tested for ultrasound transmission [38]. **c**, Chiral acoustic metamaterials show distinctive wave characteristics with respect to the tacticity of the structure [39]. 27
- 2.12 **Nonreciprocal acoustic metamaterials a**, Schematic of nonreciprocal behavior, which is enabled with piezoelectric materials driven by nonlinear electric circuit [49]. **b**, Electrically controlled magnets form nonreciprocal acoustic metamaterials. Spatio-temporal modulation shifts the original dispersion curves in k -space [50]. 28
- 2.13 **Active acoustic metamaterials a**, Schematic of active nonreciprocal acoustic metamaterials activated by piezo-switch driven by electric circuit [51]. **b**, 3D-printed octet lattices are magnetically actuated to change their configuration and also wave properties [52]. **c**, Individual Helmholtz resonators are actuated by hydraulic force to alter their resonance frequency [30]. 29

- 3.1 **Schematic of the samples' geometry and vibrational modes.** **a**, HMMs are inspired by Bouligand structures and the shape and aspect ratio of DNA molecules. **b**, Normal modes of HMMs excited by a plane wave in the z -direction: longitudinal (left: isometric, right: side view), torsional (left: isometric, right: top view), and degenerate rotational mode (left: isometric, right: side view). Coordinate system indicates the coordinates of the isometric view. Black lines show the reference positions. **c**, Truncated unit cells show different deformation behavior of the connecting beams for each mode. The color shows volumetric strain distribution, where red indicates expansion and blue represents compression. 38
- 3.2 **Varying centro-asymmetry of the HMMs and its effects on the dispersion curves.** **a, b, and c**, Top views of the HMMs model, which consists of two different materials (light gray: VeroWhite, black: stainless steel) with increasing centro-asymmetry. The white cross shows the center axis of the HMMs and the red point shows the center of mass of the top beam. **d, e, and f**, Corresponding dispersion curves with normalized frequency as a function of wavenumber. The height of the unit cell a_{HMM} is 8 cm. Blue crosses, black circles, and red asterisks represent the longitudinal mode, the torsional mode, and the rotational mode, respectively. Orange points indicate the transitional modes between different types of normal modes, while the dashed purple lines represent the solution from the ladder-like analytical model. 41
- 3.3 **Effects of added mass to the mode hybridization of the HMMs.** Dispersion curves of the **a**, centrosymmetric HMMs with same material inserts as the base material, **b**, centrosymmetric HMMs with heavier stainless steel inserts, and **c**, fully centro-asymmetric HMMs with heavier stainless steel inserts. The longitudinal modes (blue) and the transitional modes (orange) are highlighted to show the evolution of longitudinal band gaps. The color of the torsional mode (black) and the rotational modes (red) are suppressed in the background. . . . 42

- 3.4 **Dispersion curves of the HMMs with increasing degree of centrosymmetry.** **a**, 50-50 (centrosymmetric), **b**, 43.25-56.25, **c**, 37.5-62.5, **d**, 31.25-68.75, **e**, 25-75, **f**, 18.75-81.25, **g**, 12.5-87.5, **h**, 6.25-93.75, and **i**, 0-100 (fully centro-asymmetric) material distribution. The longitudinal modes (blue) and the transitional modes (orange) are highlighted to show the evolution of longitudinal band gaps. . . . 43
- 3.5 **The analytical model and corresponding unit cell.** **a**, A ladder-like meta chain model with a mass M , stiffness K , moment of inertia J , torsional rigidity C , and coupling stiffness γ . **b**, A representative volume element of the HMMs used for the analytical model. . . . 44
- 3.6 **Experimental setup and samples.** **a**, Schematic diagram and picture of the experimental setup for transmission measurements. **b**, 3D-printed samples with added stainless steel inserts for varying centro-asymmetry. (i) 50-50 material distribution on both ends (centrosymmetric, 6.25 : 6.25 mm length ratio). (ii) 25-75 material distribution (moderately centro-asymmetric, 3.125 : 9.375 mm length ratio). (iii) 0-100 material distribution (fully centro-asymmetric, 0 : 12.5 mm length ratio). Pink boxes indicate where the heavy inserts are positioned. . . . 46
- 3.7 **Experimental transmission curves coinciding with numerical dispersion curves.** **a**, Numerically predicted evolution of the longitudinal band gap (blue region) with increasing degree of centrosymmetry. **b**, Experimentally measured transmission curves (orange) are plotted with the longitudinal branch (blue dots) that is filtered from the dispersion curve of the (i) centrosymmetric, (ii) moderately centro-asymmetric, and (iii) fully centro-asymmetric HMMs. Plots are highlighted with blue shades indicating the longitudinal band gaps predicted from the numerical simulation and red shades showing the transmission dips (< -15 dB). . . . 48

- 4.1 **Wave speeds and refractive indices of water-saturated micro-lattices.** **a**, Fast pressure wave speed (c_{p1} , solid lines) and slow pressure wave speed (c_{p2} , dotted lines), and **b**, effective refractive index ($n = c_w/c_{p1}$) of water-saturated polymeric lattices with respect to porosity for different types of lattices: octet (yellow), isotropic (blue), diamond (red), and Kelvin (green) trusses. The speed of sound in water, $c_w = 1481$ m/s, is shown as reference in **a** (dashed black horizontal line). The excitation frequency of the acoustic wave is fixed at 300 kHz, which is below the estimated viscous Biot frequencies. . . . 59
- 4.2 **Experimental setup and analytical, numerical, and experimental dispersion curves.** **a**, Experimental setup with **b**, the picture (scale bar: 5 cm) and **c**, the 3D model of the measurement system. The model represents the cut plane (yellow) and the drill hole (red) of the test sample. **d**, Experimentally reconstructed dispersion curve (grey-scale colormap, normalized between 0 and 1) with the prediction from Biot theory (solid blue line) extrapolated above the viscous critical frequency (dashed blue line). The linear dispersion curve of water wave (black line) is plotted as a reference. (Inset) The microscope image of the unit cell (scale bar: 1 mm). **e**, Numerically calculated dispersion relation with longitudinally polarized in-phase modes highlighted in red, others in gray. 60
- 4.3 (a) Reference pressure amplitude with frequency centered at 800 kHz. (b) Pressure output before (red) and after (blue) normalization. . . . 63
- 4.4 **Convergence study.** Discretized meshes of the numerical model for the unit cell of **a**, octet lattice with surrounding water and **b**, equivalent poroelastic medium. **c**, The error (blue) and computation time (orange) of the eigenfrequency solver of the water-saturated octet lattice as a function of number of DOFs. The error at $\text{DOF} = 38102$ is 2245.81 %, which is not shown in the plot. 64
- 4.5 **Pressure acoustics simulation for Luneburg lens.** **a**, Discretized Luneburg lens with continuous (red curve) and discrete (yellow circles) refractive index profiles. Pressure acoustics simulations of Luneburg lens with **b**, the continuous profile, and with **c**, the discrete layers, with poroelastic properties corresponding to the effective refractive indices selected (scale bar: 5 cm). 66

- 4.6 **Optimization of Luneburg lens profile for underwater wave focusing.** **a**, Spherical aberration minimization using adaptive gradient descent optimization. **b**, Ray trajectory simulation of underwater Luneburg lens with optimized refractive index profile. 67
- 4.7 **Experimental results of the 3D-printed GRIN Luneburg lens.** **a**, Top-view photograph of the 3D printed Luneburg lens. The insets show optical microscopy images and corresponding models of unit cells from two different regions (scale bar: 0.5 mm). **b**, Normalized pressure intensity in the output plane, **c**, along the centerline, and **d**, across the focal point. Experimental data were measured from four different scan planes along the lens. 68
- 5.1 **Design and structure of the metaskull.** **a**, Concept schematic illustrating ultrasound brain imaging through the metaskull. A 3D model of the inner structures of the metamaterials shows a periodic tessellation of honeycomb unit cells, with $h = 37 \mu\text{m}$, $w = 32.3 \mu\text{m}$, $th = 7.5 \mu\text{m}$, and $tw = 4.5 \mu\text{m}$. **b**, The metaskull can fit an arbitrarily shaped region in a curved parietal lobe of the mouse skull. **c**, The metaskulls are fabricated with a microscale 2-photon polymerization technique. SEM images of the sample of the metaskull from the top and isometric views. Scale bars: **b**, 1 cm; **c**, 200 μm (left), 100 μm (bottom right), and 20 μm (top right). 76

- 5.2 **Quasi-static mechanical characterization of the metaskull meta-materials.** **a**, Optical microscopy image of a metaskull sample for compression testing, along with the probe tip of the measurement system. **b**, Von Mises stress distribution within the FE model compressed with a $50\ \mu\text{m} \times 50\ \mu\text{m}$ square-faced probe tip. A quarter of the model is shown for the cross-sectional views. Side-view images show the stress concentration around the drainage holes. **c**, Stress-strain curves showing the single loading-unloading cycle of the honeycomb plate-lattices and a PMP film under indentation. Dashed lines indicate the slopes at the onset of the unloading curve, which are used to calculate the effective Young's moduli. **d**, The average and standard deviation of the Young's modulus obtained from experiments, for both the honeycomb plate-lattices and a PMP film. Red lines indicate the prediction from the numerical simulation or known material properties. **e**, The theoretical upper bound for the modulus of a two-phase, isotropic material (gray) crossed by an isoline matching the acoustic impedance of the brain (blue), both as a function of the Young's modulus and density of the constituent solid. The acoustic impedance of the brain is constant at $1.52\ \text{MRayl}$ and follows a relation, $Z = \sqrt{\rho E}$. The normalized Young's modulus and relative density are normalized with the Young's modulus and density of IP-S, respectively. 78
- 5.3 **Quasi-static mechanical testing.** **a**, Sets of 5 independent stress-strain curves of the metaskull ($148\ \mu\text{m}$) and a PMP film ($125\ \mu\text{m}$) tested with the indentation experiment setup. **b**, Bar graph shows the distribution, average, and standard deviation of the effective Young's modulus derived from the measurement data. 79
- 5.4 **Characterization of the boundary effect.** **a**, The FE model for the compression simulation of a monolithic PMP film. The von Mises stress distribution within the film under $1\ \mu\text{m}$ indentation is shown on the cross sections of the model. **b**, Effective compressive modulus (blue, square), and the number of degrees of freedom (red, circle) as functions of the radius of the model. Beyond $r = 150\ \mu\text{m}$ (black, dashed), the value of the modulus saturates while the computation cost increases significantly. 80

- 5.5 **Characterization of the geometric nonlinearity.** The applied stress as a function of deformation displacement for both geometrically linear (red, square) and nonlinear (blue, circle) cases. The discrepancy between two cases gets negligible for small deformation. 81
- 5.6 **Effect of the drainage holes to the structural integrity.** **a**, The FE compression model with horizontal drainage holes showing the von Mises stress distribution on the cross sections. **b**, The FE model without the drainage holes shows less concentrated stress within the metamaterials. 82
- 5.7 **Characterization of dynamic mechanical properties of the metaskulls.** **a**, FE model for the ultrasonic wave propagation at 15 and 30 MHz through 4 unit cells of the honeycomb plate-lattices in water. (Left) Pressure distribution within the water surrounding the metaskulls and the air inside the cavities. (Right) The volumetric strain distribution within the honeycomb metamaterials. **b**, The dispersion curves of the honeycomb metamaterials in both $\Gamma - A$ and $\Gamma - 0.2L$ directions. Curves' colors indicate the longitudinal polarization of each mode (blue: pressure mode, red: shear mode, and purple: hybridized mode). **c**, Experimental transmission coefficients of the metaskull samples with varying thickness averaged between 13.75 and 17.5 MHz, shown with error bars. The slope of the linear regression plot (blue, solid, $r^2 = 0.99$) is -83.0 dB/cm, whereas the attenuation coefficient of a 125- μm -thick PMP film (black, dashed) is -36.6 dB/cm. **d**, Both experimentally measured (dotted) and numerically derived (solid) transmission curves of a PMP film (black, dotted) and the metaskulls with varying thickness with respect to frequency. 85
- 5.8 **Frequency dependent pressure and volumetric strain distribution.** **a**, The FE models for transmission simulation showing the input and output pressure fields, and the metaskull. The acoustic pressure and volumetric strain distribution at 30 MHz show more steep attenuation of the traveling waves. **b**, The pressure (blue) and volumetric strain (red) profiles along the vertical axis at 15 and 30 MHz. The envelopes (green) imply different attenuation characteristics at different frequencies. 87

- 5.9 **Effect of the viscosity of air and the viscoelasticity of the solid to the transmission.** **a**, (Top) The acoustic pressure and the volumetric strain profiles when the viscoelasticity of the solid is ignored. (Bottom) The profiles with the isotropic loss factor, η , at 0.075. For both plots, the profiles with or without the air inside the cavity of the metamaterials are not distinguishable. **b**, The magnified views of the parts of the profiles from the left panel showing the attenuation due to the viscosity of air. 88
- 5.10 **Thermoviscous dissipation with respect to the direction of the drainage holes.** **a**, The acoustic pressure (left) and the thermoviscous energy dissipation (right) distributions within the air inside the cavities of the horizontally holed metamaterials. The pressure distribution is normalized by the pressure of the input waves. **b**, The acoustic pressure (left) and the thermoviscous energy dissipation (right) distributions within the air inside the cavities of the vertically holed metamaterials. 89
- 5.11 **Angle-dependent dispersion curves of the metaskull.** **a**, Wavevectors of the plane waves are shown with respect to the irreducible Brillouin zone of the honeycomb unit cell. **b**, The dispersion curve in the $\Gamma - A$ direction, parallel to the z -axis. **c**, The dispersion curves of the plane waves with gradually increased tilting against the z -axis toward the x -axis, and **d**, toward the y -axis. 90
- 5.12 **Angle-dependent transmission curves of the metaskull.** Numerically calculated transmission curves of the metaskull with different number of layers at 15 MHz with respect to the incident angle of the pressure waves in $\Gamma - 0.2L$ direction. 92
- 5.13 **Side-by-side comparison of different skull replacement material for high sensitive cerebral power Doppler imaging in mice (N = 4).** **a**, Cerebral power Doppler imaging of one mouse through the intact skull, after craniotomy without any material, and through a layer of PMP (125 μm) or metaskulls (111, 148, 185, 259, and 333 μm) (Representative mouse). **b**, Standardized total intensity of the power Doppler images with respect to the skull replacement material. **c**, Standardized SNR of the power Doppler in i. the cortex and ii. the deeper structures. Scale bar: 5mm. PD = Power Doppler. 94

- 5.14 **Longitudinal fUSI study in mice after metaskull implantation. a,** Longitudinal study protocol: mice are implanted with the metaskull (148 μm) at day 0. They are then examined at day 10, 20, 34, . . . during which visually evoked activity is recorded. **b,** Power Doppler images are acquired around coronal plane B-2.2 mm showing the structure of the vascular network (top, hot colors) and the activated LGN following visual stimulation (bottom, cold colors) 97

LIST OF TABLES

<i>Number</i>	<i>Page</i>
3.1 Effective mechanical parameters of the HMMs. Wave speeds from the dispersion curves are calculated under long wavelength assumption. Corresponding effective stiffness and mass of the RVE of the HMMs for longitudinal modes and torsional modes are listed below.	44
5.1 Literatures with the characterization of PMP, and PMP films as a cranial window.	75
5.2 Resultant stresses under compression. σ_{lin} and σ_{nlin} indicate the resultant stresses under the deformation, Δz , assuming geometric linearity and nonlinearity, respectively. The error is calculated as $Error = (\sigma_{lin} - \sigma_{nlin})/\sigma_{lin} \times 100\%$	81
5.3 Wavevectors in the Brillouin zone, corresponding angles, and the resulting transmission characteristics. A The wavevectors in the hexagonal irreducible Brillouin zone and the corresponding incident angles of the plane acoustic waves. The center frequency, f_c , and the bandwidth, Δf , are acquired from the dispersion curves in Fig. 5.11. The transmission coefficients are derived from the FE transmission models with 9-unit-cell metaskulls (Fig. 5.12).	93

NOMENCLATURE

Bouligand. A layered and rotated microstructure composed of multiple lamellae, which is frequently found in naturally designed materials. Adjacent lamellae are progressively rotated with respect to their neighbors. It is found in various natural structures, for example, inside the exoskeleton of crustacean.

Bregma. The point or area of the skull where the sagittal and coronal sutures joining the parietal and frontal bones come together.

Darcy's law. An equation that describes the flow of a fluid through a porous medium, which is analogous to Ohm's law in electrostatics. It describes the linear relation between the volume flow rate of the fluid and the pressure difference via the hydraulic conductivity.

Dispersion. The phenomenon in which the phase velocity of a wave depends on its frequency. A medium having this common property may be termed a dispersive medium.

Finite element method (FEM). A method for numerically solving differential equations arising in engineering and mathematical modeling. Studying or analyzing a phenomenon with FEM is often referred to as finite element analysis (FEA).

Representative volume element (RVE). The smallest volume over which a measurement can be made that will yield a value representative of the whole. In the case of periodic materials, one simply chooses a periodic unit cell whose property of interest can include mechanical properties such as elastic moduli.

Ultrasound. Sound waves with frequencies higher than the upper audible limit of human hearing. This limit varies from person to person and is approximately 20 kilohertz (20,000 hertz) in healthy young adults. Ultrasound devices operate with frequencies from 20 kHz up to several gigahertz.

Chapter 1

INTRODUCTION

1.1 Research objectives

This thesis discusses the mechanics and design of acoustic metamaterials, materials whose dynamic characteristics are derived geometrically, either from the periodicity of a unit element or from the periodic arrangement of resonant features at the subwavelength scale. These materials have the ability to tailor their wave properties, offering new opportunities to create effective media that outperform conventional materials. The main goals of this work are to (1) explore, study, and design acoustic metamaterials with respect to acoustic waves propagating through them in increasing dimensions, (2) characterize their unique acoustic properties using various analysis methods, and (3) model, fabricate, and analyze acoustic metamaterials using advanced manufacturing technologies for biomedical applications. The behavior of these materials is characterized using the finite element method, and the predictions are validated through experimental measurements. Additionally, I demonstrate that acoustic metamaterials have the potential to be used for the manipulation of ultrasound waves, specifically for lensing and brain imaging.

1.2 Research motivation**Architected materials with unprecedented acoustic characteristics**

Acoustics is a study of sound and vibrational waves and their propagation. These types of waves are present in many aspects of our daily lives, including human verbal communication, structural vibration [1], and seismic waves [2, 3]. Acoustics has been extensively studied for centuries from a civil engineering perspective, as it plays a crucial role in developing non-destructive methods for identifying defects in skyscrapers [4] and designing building components that can effectively withstand earthquakes [3, 5]. Acoustic waves with frequencies beyond the range of human hearing are called ultrasound waves, and they are frequently used in various therapeutic ultrasound technologies for medicine and industry [6, 7]. However, it can be challenging to control the propagation of ultrasound waves, since they have high frequency, between 20 kHz and 40 MHz, which can be easily attenuated or distorted by the medium. Moreover, ultrasound waves with small wavelengths effectively interact with microscale scatterers or resonators that require advanced

manufacturing technologies to fabricate. The motivation for the study of acoustic metamaterials is driven by the desire to develop new materials that can control the way that sound waves propagate through them.

Acoustic metamaterials are artificially created structures for controlling sound propagation, and they consist of either periodically tessellated unit cells, or arrays of subwavelength resonators that respond to specific frequencies, or both. These metamaterials are made up of small "meta-atoms" that behave like a continuous material with unusual properties when they are combined in large quantities. The study of waves propagating through periodic structures has a long history, but it was not until the development of photonic [8, 9] and phononic crystals [10–12] that researchers began to fully understand the potential for using engineered structures to control wave properties. Research in this area has expanded rapidly as it became possible to create structures using relatively simple building blocks on a subwavelength scale [10, 13–15]. These acoustic metamaterials can behave similarly to continuous materials, but have properties that differ significantly from those of conventional materials. Periodicity in acoustic materials can influence the way that waves propagate through them in a number of ways by affecting its stiffness [16–18] and mass [19–22], which in turn can affect the way that waves propagate through it. In addition, the periodicity of the microstructure can cause the waves to scatter and interfere with itself in a way that modifies the overall wave behavior [23–25].

Research on acoustic metamaterials focuses on the study of materials and/or geometries that can be designed to exhibit specific acoustic properties, such as the ability to guide [26–28], focus [11, 29, 30], absorb [31–34], and reflect [35–37] sound waves, or negative refraction [13, 26, 38]. This research may involve theoretical modeling, computational simulations, and experimental testing to understand the properties and potential applications of these materials. Some of the areas of study within the research on acoustic metamaterials include the design of metamaterials with specific wave propagation properties, the development of new manufacturing techniques for producing metamaterials [39–41], and the exploration of potential applications for these materials in fields, including, but not limited to noise control [42], sensors [43], non-destructive testing [1, 44, 45], ultrasound imaging [46, 47], medical devices [48, 49], drug delivery [50, 51], and cancer therapy [52–54].

Current obstacles in ultrasound industry and research

Ultrasound is widely used in medical industry and biomedical research due to its various advantages [7, 55–64]. It is a non-invasive and portable imaging modality, which allows for quick and easy imaging in various settings. The real-time imaging capabilities of ultrasound make it useful for imaging organs that move, such as the heart and blood vessels. Additionally, it is relatively inexpensive compared to other imaging modalities such as CT and MRI. It has a wide range of applications including diagnostic imaging [55, 60], guiding procedures [59], monitoring and therapeutic applications [57]. Furthermore, it is a relatively safe imaging modality as it does not involve ionizing radiation and has no known long-term risks. The combination of these characteristics make ultrasound a valuable tool for the medical industry and for biomedical research.

The ultrasound industry and research is currently facing a number of obstacles. For advanced treatments and applications, phased-array transducer must be adopted as they enable the precise control of the wavefront, however, its widespread adoption and usage can be restricted by its cost [65]. Another obstacle of ultrasound is the limited penetration depth, which can restrict its utility in certain applications such as internal organs imaging [66]. Additionally, ultrasound images tend to have lower resolution than other imaging modalities, making it harder to detect small abnormalities or structures [67, 68]. The diagnostic accuracy of ultrasound is limited for cases such as small tumors, lung or heart conditions, leading to false positive or negative results. Furthermore, ultrasound images are often qualitative rather than quantitative, therefore certain physiological parameters such as blood flow cannot be accurately measured. Another limitation is the safety concerns that arise from excessive exposure to high-intensity ultrasound waves, which can lead to heating and tissue damage [69]. Finally, ultrasound waves do not penetrate well through air, limiting their use for lung imaging [70].

Overcoming the obstacles using acoustic metamaterials

Exceptional and controllable acoustic properties of acoustic metamaterials can help overcome some of the current obstacles in the ultrasound industry. Acoustic metamaterials can be utilized in various ways to improve several aspects of ultrasound imaging, by focusing plane pressure waves, and by enhancing the transmission, resolution, and diagnostic accuracy [71]. For example, the metamaterials can be engineered to focus and direct ultrasound waves by either controlling the speed or the phase of the waves. This will make ultrasound equipment simpler and more

cost-effective by achieving the focusing capability without the need of expensive phased array transducers [46, 72, 73]. Moreover, ultrasound wave propagation can be improved by acoustic metamaterials to enhance penetration through air, biological tissue, or even aberrating layers by calculating and offsetting the expected attenuation or reflecting [48, 51, 74–76]. Traditional ultrasound systems rely on the transmission and reflection of sound waves through tissue to generate images, but the resolution of these images can be limited by the properties of the tissue and the size of the ultrasound transducer [77]. Acoustic metamaterials can improve ultrasound imaging by allowing for super-resolution imaging. This is achieved by reducing the intensity of ultrasound waves and increasing the contrast resolution to the subwavelength level. [44, 78, 79]. Last but not least, acoustic metamaterials can also make it possible to deliver drugs to previously inaccessible locations [50, 51, 80], and improve cancer therapy through the use of therapeutic ultrasound for medical treatment [47, 52–54].

1.3 Research approach, methods, and challenges

Research Approach

In this thesis, we implement three research approaches to corroborate each other's findings. First, we build a finite element model to design the metamaterials and estimate their acoustic behaviors. Among various designs with their distinctive dynamic characteristics, ones with interesting aspects with realizable geometrical and materialistic configuration are chosen. Then, we construct analytical form of the problem that describes basic acoustic behaviors, mainly in the lower frequency range of the dispersion curves assuming the long-wave approximation. Lastly, we fabricate the finite-sized metamaterial samples and measure their transmission coefficients or quasi-static properties. The experimental results are analyzed and compared to the simulation results.

Methods

To solve the problem analytically, we construct characteristic equations of the system from the equations of motion and the force balance equation. The dispersion curves in the irreducible Brillouin zone are numerically derived from the characteristic equations by sweeping the input frequency range using MATLAB.

A finite element method is performed via a commercial software (COMSOL Multiphysics). We start by building the most basic volume element, i.e., unit cell, of the structure that can represent the whole system by tessellation. Then, we feed mate-

rial inputs and apply initial or boundary conditions based on the problem settings. For example, we impose Bloch-Floquet periodic boundary conditions to assume infinitely periodic unit cells in certain directions. The mesh for the finite element model is generated based on the geometry and the input conditions. The study is chosen based on the physics of the problems we are interested in, for example, frequency or eigenfrequency study are chosen for dynamic loading conditions.

To validate these analytical and numerical results, experiments are conducted mainly for mechanical characterization, including quasi-static compression tests or transmission measurements. Geometrically sophisticated samples can be fabricated using 3D printing, followed by extra machining for fine-tuning if needed. Vibration measurement set-up includes piezoelectric transducers in Hz to sub-MHz range for exciting and sending vibration signals, and laser Doppler vibrometer for receiving and recording the output signals. Underwater measurement set-up has piezoelectric transducers that are acoustically matched to water, paired with acoustically-matched hydrophone for picking up the transmitted signal. Arbitrary signals can be generated and sent by function generators, which are then gathered by an oscilloscope for the data acquisition and analysis. MATLAB codes are used to operate and control each equipment and to collect data. Further analysis regarding the experimentally unachievable geometries or the detailed data unobtainable from the experiments are solved with more sophisticated finite element analysis.

Challenges

The limitations of the analytical approach is that the characteristic equation formulation for the problems with complex geometries or boundary conditions is nearly impossible. Only a few geometries can be represented as the ensemble of masses and springs are very small in number, especially when the problem is in 3D. The analytical method is used in this thesis to solve the representative behavior of the model under simplifying assumptions.

The finite element analysis is a powerful and versatile tool that can construct and solve multidimensional problems with sophisticated geometries. However, the computation power of the processor limits the models that can be dealt with. Even the simple finite element model consists of thousands of degrees of freedom, and efficient and accelerated solvers were not easily accessible until recently. In addition, incorrect understanding of the physics and erroneous setting of the initial or boundary conditions of the problems may lead to solutions that is not feasible, so deep

knowledge of the governing physics is essential for the user to run successful simulations.

Lastly, experimental approach is adopted to validate the analytical or numerical predictions and demonstrate potential applications. It is a strong tool to convince the readers of the theoretical work with actual samples and measurements. Nevertheless, it is not always easy to construct an experimental setup that can best test the samples due to many reasons, including but not limited to, the choice of materials, structures, testing methods, or resources. Proper choice of experimental methods is critical for the experimental data to be trustworthy.

1.4 Chapter outlook

In Chapter 2, I described the basic mechanics of a simple acoustic metamaterial model. I formulated the equations of motion of simple models, 1-dimensional infinite monoatomic and diatomic chains, and solved their dispersion relations. These harmonic chain models are composed of masses and springs that are only allowed to move in a single axis. By calculating the dispersion curves in their irreducible Brillouin zone, I derived some of the essential physical quantities including the group and phase velocities and band gap. I also briefly introduced more complicated acoustic metamaterials in 2D and 3D as well.

In Chapter 3, I studied 1D wave propagation in acoustic metamaterials to understand the mode shapes and their hybridization for the analysis of the dispersion curve. Acoustic metamaterials with chirality, referred to as helical metamaterials (HMMs), showed unique acoustic characteristics arising from their geometry. I designed the metamaterials' geometry to accommodate varying centro-asymmetry with uneven distribution of denser masses. I examined the corresponding dispersion curves, which revealed increased mode coupling and subwavelength band gap formation with greater centro-asymmetry. I experimentally validated the acoustic characteristics of the HMMs by measuring the transmission coefficients.

In Chapter 4, I investigated 2D wave propagation in acoustic metamaterials to understand how to effectively control the direction of wave propagation, specifically ultrasound, and identified the key factors that determined the success of this control. To achieve this, I studied the characteristics of water-saturated polymeric microlattices in the context of Biot theory and leveraged my findings to realize a water-filled microlattice GRIN lens. I showed that the traditional Luneburg lens could be effectively configured as a discretized GRIN lens with a modified index profile for

underwater wave focusing. I verified my design using a computationally efficient poroelastic model combined with a pressure acoustics study. I performed underwater experiments using the 3D-printed GRIN lens, showing matching pressure output profiles from both experimental and numerical results.

In Chapter 5, I focused on 3D wave propagation in acoustic metamaterials to successfully develop a microlattice device for living animals based on the understandings from previous chapters. I aimed to create metamaterials that could be customized to replace skull and serve as a protective layer for the brain and a transparent window for ultrasonic waves. To achieve both quasi-static mechanical robustness and acoustic transparency in the ultrasonic regime, I designed metamaterials with structural features in the micrometer scale, arranged in honeycomb plate lattices, which I fabricated using 2-photon polymerization. The metamaterial cranial window was designed to be impedance matched with biological tissue, to enable low loss transmission of ultrasonic waves for imaging brain activity in small animals (~ 15 MHz). To demonstrate the long-term stability, I performed longitudinal brain imaging experiments in vivo via Doppler ultrasound imaging with visual stimulation.

References

1. Kino, G. Acoustic imaging for nondestructive evaluation. *Proceedings of the IEEE* **67**, 510–525 (Apr. 1979).
2. Sabatier, J. M., Bass, H. E., Bolen, L. N. & Attenborough, K. Acoustically induced seismic waves. *The Journal of the Acoustical Society of America* **80**, 646–649 (1986).
3. Kausel, E. & Assimaki, D. Seismic Simulation of Inelastic Soils via Frequency-Dependent Moduli and Damping. *Journal of Engineering Mechanics* **128**, 34–47 (Jan. 2002).
4. Bøving, K. G. *NDE Handbook: Non-Destructive Examination Methods for Condition Monitoring* (Elsevier, 2014).
5. Cardoso, R., Lopes, M. & Bento, R. *EARTHQUAKE RESISTANT STRUCTURES OF PORTUGUESE OLD ‘POMBALINO’ BUILDINGS* in (Vancouver, B.C., Canada, Aug. 2004).
6. Merton, D. A. Diagnostic Medical Ultrasound Technology. *Journal of Diagnostic Medical Sonography* **13**, 10S–23S (1997).
7. Bourdeau, R. W. *et al.* Acoustic reporter genes for noninvasive imaging of microorganisms in mammalian hosts. *Nature* **553**, 86–90 (2018).
8. Yablonovitch, E. Photonic Crystals. *Journal of Modern Optics* **41**, 173–194 (1994).

9. Joannopoulos, J. D., Villeneuve, P. R. & Fan, S. Photonic crystals. *Solid State Communications* **102**, 165–173 (1997).
10. Liu, Z. *et al.* Locally Resonant Sonic Materials. *Science* **289**, 1734–1736 (2000).
11. Yang, S. *et al.* Focusing of Sound in a 3D Phononic Crystal. *Physical Review Letters* **93**, 024301 (2004).
12. Page, J. H. *et al.* Phononic crystals. *physica status solidi (b)* **241**, 3454–3462 (2004).
13. Li, J. & Chan, C. T. Double-negative acoustic metamaterial. *Physical Review E* **70**, 055602 (2004).
14. Lai, Y., Wu, Y., Sheng, P. & Zhang, Z.-Q. Hybrid elastic solids. *Nature Materials* **10**, 620–624 (2011).
15. Hu, X., Ho, K.-M., Chan, C. T. & Zi, J. Homogenization of acoustic metamaterials of Helmholtz resonators in fluid. *Physical Review B* **77**, 172301 (2008).
16. Chronopoulos, D., Antoniadis, I. & Ampatzidis, T. Enhanced acoustic insulation properties of composite metamaterials having embedded negative stiffness inclusions. *Extreme Mechanics Letters* **12**, 48–54 (2017).
17. Liu, K., Zegard, T., Pratapa, P. P. & Paulino, G. H. Unraveling tensegrity tessellations for metamaterials with tunable stiffness and bandgaps. *Journal of the Mechanics and Physics of Solids* **131**, 147–166 (2019).
18. Wang, Y. & Sigmund, O. Quasiperiodic mechanical metamaterials with extreme isotropic stiffness. *Extreme Mechanics Letters* **34**, 100596 (2020).
19. Sheng, P., Mei, J., Liu, Z. & Wen, W. Dynamic mass density and acoustic metamaterials. *Physica B: Condensed Matter* **394**, 256–261 (2007).
20. Cheng, Y., Xu, J. Y. & Liu, X. J. One-dimensional structured ultrasonic metamaterials with simultaneously negative dynamic density and modulus. *Physical Review B* **77**, 045134 (2008).
21. Singh, R., Rockstuhl, C. & Zhang, W. Strong influence of packing density in terahertz metamaterials. *Applied Physics Letters* **97**, 241108 (2010).
22. Oh, J. H., Kwon, Y. E., Lee, H. J. & Kim, Y. Y. Elastic metamaterials for independent realization of negativity in density and stiffness. *Scientific Reports* **6**, 23630 (2016).
23. Gorishnyy, T., Ullal, C. K., Maldovan, M., Fytas, G. & Thomas, E. L. Hypersonic Phononic Crystals. *Physical Review Letters* **94**, 115501 (2005).
24. Qiu, C., Liu, Z., Mei, J. & Ke, M. The layer multiple-scattering method for calculating transmission coefficients of 2D phononic crystals. *Solid State Communications* **134**, 765–770 (2005).

25. Olsson, R. H. & El-Kady, I. Microfabricated phononic crystal devices and applications. *Measurement Science and Technology* **20**, 012002 (2008).
26. Xie, Y., Popa, B.-I., Zigoneanu, L. & Cummer, S. A. Measurement of a Broadband Negative Index with Space-Coiling Acoustic Metamaterials. *Physical Review Letters* **110**, 175501 (2013).
27. Celli, P. & Gonella, S. Manipulating waves with LEGO® bricks: A versatile experimental platform for metamaterial architectures. *Applied Physics Letters* **107**, 081901 (2015).
28. Liu, G.-S. *et al.* Acoustic waveguide with virtual soft boundary based on metamaterials. *Scientific Reports* **10**, 981 (2020).
29. Zhang, X. Acoustic resonant transmission through acoustic gratings with very narrow slits: Multiple-scattering numerical simulations. *Physical Review B* **71**, 241102 (2005).
30. Su, X., Norris, A. N., Cushing, C. W., Haberman, M. R. & Wilson, P. S. Broadband focusing of underwater sound using a transparent pentamode lens. *The Journal of the Acoustical Society of America* **141**, 4408–4417 (2017).
31. Pinton, G. *et al.* Attenuation, scattering, and absorption of ultrasound in the skull bone. *Medical Physics* **39**, 299–307 (2012).
32. Mei, J. *et al.* Dark acoustic metamaterials as super absorbers for low-frequency sound. *Nature Communications* **3**, 756 (2012).
33. Tang, Y. *et al.* Hybrid acoustic metamaterial as super absorber for broadband low-frequency sound. *Scientific Reports* **7**, 43340 (2017).
34. Li, Z., Wang, Z., Guo, Z., Wang, X. & Liang, X. Ultra-broadband sound absorption of a hierarchical acoustic metamaterial at high temperatures. *Applied Physics Letters* **118**, 161903 (2021).
35. Molerón, M., Serra-Garcia, M. & Daraio, C. Visco-thermal effects in acoustic metamaterials: from total transmission to total reflection and high absorption. *New Journal of Physics* **18**, 033003 (2016).
36. Palma, G., Mao, H., Burghignoli, L., Göransson, P. & Iemma, U. Acoustic Metamaterials in Aeronautics. *Applied Sciences* **8**, 971 (2018).
37. Park, C. M. & Lee, S. H. Zero-reflection acoustic metamaterial with a negative refractive index. *Scientific Reports* **9**, 3372 (2019).
38. Brunet, T. *et al.* Soft 3D acoustic metamaterial with negative index. *Nature Materials* **14**, 384–388 (2015).
39. Kennedy, J. *et al.* The Influence of Additive Manufacturing Processes on the Performance of a Periodic Acoustic Metamaterial. *International Journal of Polymer Science* **2019**, e7029143 (2019).

40. Kumar, S. & Lee, H. P. The Present and Future Role of Acoustic Metamaterials for Architectural and Urban Noise Mitigations. *Acoustics* **1**, 590–607 (2019).
41. Hedayati, R. & Bodaghi, M. Acoustic Metamaterials and Acoustic Foams: Recent Advances. *Applied Sciences* **12**, 3096 (2022).
42. Gao, N. *et al.* Acoustic Metamaterials for Noise Reduction: A Review. *Advanced Materials Technologies* **7**, 2100698 (2022).
43. Bogue, R. Sensing with metamaterials: a review of recent developments. *Sensor Review* **37**, 305–311 (2017).
44. Molerón, M. & Daraio, C. Acoustic metamaterial for subwavelength edge detection. *Nature Communications* **6**, 8037 (2015).
45. Ozevin, D. & Tol, S. in *The Rise of Smart Cities* (eds Alavi, A. H., Feng, M. Q., Jiao, P. & Sharif-Khodaei, Z.) 115–137 (Butterworth-Heinemann, 2022).
46. Zhang, S., Yin, L. & Fang, N. Focusing Ultrasound with an Acoustic Metamaterial Network. *Physical Review Letters* **102**, 194301 (2009).
47. Chen, H. *et al.* Ultrasound acoustic metamaterials with double-negative parameters. *Journal of Applied Physics* **119**, 204902 (2016).
48. Craig, S. R., Welch, P. J. & Shi, C. Non-Hermitian complementary acoustic metamaterials for lossy barriers. *Applied Physics Letters* **115**, 051903 (2019).
49. Craig, S. R., Welch, P. J. & Shi, C. Non-Hermitian Complementary Acoustic Metamaterials for Imaging Through Skull With Imperfections. *Frontiers in Mechanical Engineering* **6** (2020).
50. Sirsi, S. R. & Borden, M. A. State-of-the-art materials for ultrasound-triggered drug delivery. *Advanced Drug Delivery Reviews. Ultrasound triggered drug delivery* **72**, 3–14 (2014).
51. Boissenot, T., Bordat, A., Fattal, E. & Tsapis, N. Ultrasound-triggered drug delivery for cancer treatment using drug delivery systems: From theoretical considerations to practical applications. *Journal of Controlled Release* **241**, 144–163. (2023) (2016).
52. Kremkau, F. W. Cancer therapy with ultrasound: A historical review. *Journal of Clinical Ultrasound* **7**, 287–300 (1979).
53. Wood, A. K. W. & Sehgal, C. M. A Review of Low-Intensity Ultrasound for Cancer Therapy. *Ultrasound in Medicine & Biology* **41**, 905–928 (2015).
54. Hsiao, Y.-H., Kuo, S.-J., Tsai, H.-D., Chou, M.-C. & Yeh, G.-P. Clinical Application of High-intensity Focused Ultrasound in Cancer Therapy. *Journal of Cancer* **7**, 225–231 (2016).
55. Fenster, A. & Downey, D. 3-D ultrasound imaging: a review. *IEEE Engineering in Medicine and Biology Magazine* **15**, 41–51 (1996).

56. Sato, T., Shapiro, M. G. & Tsao, D. Y. Ultrasonic Neuromodulation Causes Widespread Cortical Activation via an Indirect Auditory Mechanism. *Neuron* **98**, 1031–1041.e5 (2018).
57. Baker, K. G., Robertson, V. J. & Duck, F. A. A Review of Therapeutic Ultrasound: Biophysical Effects. *Physical Therapy* **81**, 1351–1358 (2001).
58. Chung, B. & Preston Wiley, J. Extracorporeal Shockwave Therapy. *Sports Medicine* **32**, 851–865 (2002).
59. Marhofer, P., Greher, M. & Kapral, S. Ultrasound guidance in regional anaesthesia†. *BJA: British Journal of Anaesthesia* **94**, 7–17 (2005).
60. Wells, P. N. T. Ultrasound imaging. *Physics in Medicine & Biology* **51**, R83 (2006).
61. Mo, L. & Cobbold, R. A nonstationary signal simulation model for continuous wave and pulsed Doppler ultrasound. *IEEE Transactions on Ultrasonics, Ferroelectrics, and Frequency Control* **36**, 522–530 (1989).
62. Bergel, A., Deffieux, T., Dmené, C., Tanter, M. & Cohen, I. Local hippocampal fast gamma rhythms precede brain-wide hyperemic patterns during spontaneous rodent REM sleep. *Nature Communications* **9**, 5364 (2018).
63. Jiang, X. *et al.* A Review of Low-Intensity Pulsed Ultrasound for Therapeutic Applications. *IEEE Transactions on Biomedical Engineering* **66**, 2704–2718 (2019).
64. Shapiro, M. G. *et al.* Biogenic gas nanostructures as ultrasonic molecular reporters. *Nature Nanotechnology* **9**, 311–316 (2014).
65. Lee, J.-H. & Choi, S.-W. A parametric study of ultrasonic beam profiles for a linear phased array transducer. *IEEE Transactions on Ultrasonics, Ferroelectrics, and Frequency Control* **47**, 644–650 (2000).
66. Moros, E. G., Fan, X. & Straube, W. L. An investigation of penetration depth control using parallel opposed ultrasound arrays and a scanning reflector. *The Journal of the Acoustical Society of America* **101**, 1734–1741 (1997).
67. Huisman, T. A. G. M. Intracranial hemorrhage: ultrasound, CT and MRI findings. *European Radiology* **15**, 434–440 (2005).
68. Kao, L. Y. *et al.* Beyond Ultrasound: CT and MRI of Ectopic Pregnancy. *American Journal of Roentgenology* **202**, 904–911 (2014).
69. Ter Haar, > & Coussios, C. High intensity focused ultrasound: Physical principles and devices. *International Journal of Hyperthermia* **23**, 89–104 (2007).
70. Gargani, L. Lung ultrasound: a new tool for the cardiologist. *Cardiovascular Ultrasound* **9**, 6. ISSN: 1476-7120 (2011).
71. Cummer, S. A., Christensen, J. & Alù, A. Controlling sound with acoustic metamaterials. *Nature Reviews Materials* **1** (2016).

72. Ambati, M., Fang, N., Sun, C. & Zhang, X. Surface resonant states and super-lensing in acoustic metamaterials. *Physical Review B* **75**, 195447 (2007).
73. Popa, B.-I., Shinde, D., Konneker, A. & Cummer, S. A. Active acoustic metamaterials reconfigurable in real time. *Physical Review B* **91**, 220303 (2015).
74. Naify, C. J., Chang, C.-M., McKnight, G. & Nutt, S. Transmission loss and dynamic response of membrane-type locally resonant acoustic metamaterials. *Journal of Applied Physics* **108**, 114905 (2010).
75. Park, J. J., Lee, K. J. B., Wright, O. B., Jung, M. K. & Lee, S. H. Giant Acoustic Concentration by Extraordinary Transmission in Zero-Mass Metamaterials. *Physical Review Letters* **110**, 244302 (2013).
76. Fleury, R. & Alù, A. Extraordinary Sound Transmission through Density-Near-Zero Ultranarrow Channels. *Physical Review Letters* **111**, 055501 (2013).
77. Kremkau, F. W. & Taylor, K. J. Artifacts in ultrasound imaging. *Journal of Ultrasound in Medicine* **5**, 227–237 (1986).
78. Liu, A., Zhou, X., Huang, G. & Hu, G. Super-resolution imaging by resonant tunneling in anisotropic acoustic metamaterials. *The Journal of the Acoustical Society of America* **132**, 2800–2806 (2012).
79. Laureti, S. *et al.* Trapped air metamaterial concept for ultrasonic sub-wavelength imaging in water. *Scientific Reports* **10**, 10601 (2020).
80. Szablowski, J. O., Bar-Zion, A. & Shapiro, M. G. Achieving Spatial and Molecular Specificity with Ultrasound-Targeted Biomolecular Nanotherapeutics. *Accounts of Chemical Research* **52**, 2427–2434 (2019).

ACOUSTIC METAMATERIALS

2.1 Chapter preamble

Acoustic metamaterials (AMMs) are architected materials with unique acoustic properties that can control and manipulate the transmission of sound waves. These materials have the potential to revolutionize a wide range of applications, from noise reduction and vibration damping to ultrasonic imaging and sound insulation. In this chapter, we will introduce the basic concepts of acoustic metamaterials, including their 1D chain models for basic theoretical understanding. We will also explore the different types and mechanisms of acoustic metamaterials and their manufacturing techniques.

2.2 1D Mass and Spring System and dispersion relation

To analytically approach AMMs, one can generate simple models consisting of masses and springs, which represent an unit component and its interaction with neighboring components [1]. The most basic model would be a 1-dimensional (1D) chain of masses and springs with identical mass and spring constant. A one-dimensional monoatomic harmonic crystal is a structure consisting of an infinite chain of masses, labeled as M , that interact with one another through harmonic springs with a spring constant of K . The distance between these masses when they are at rest is defined as a (Fig. 2.1a).

The motion of atom " n " in the absence of external forces can be described by the

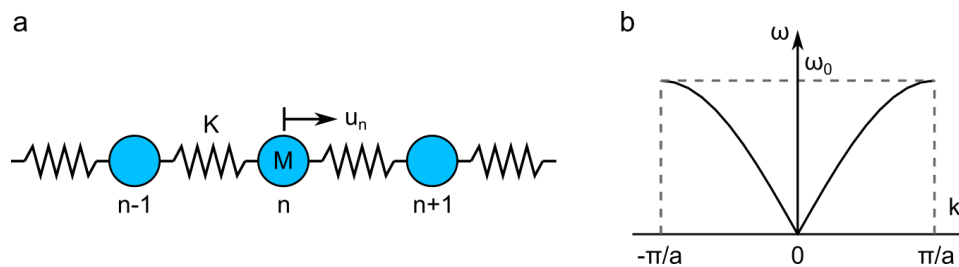


Figure 2.1: Monoatomic infinite 1-dimensional mass and spring chain. **a**, Schematics of 1d monoatomic chain. **b**, The dispersion curve of 1D monoatomic chain in the first Brillouin zone. ω_0 is the cutoff frequency, defined as $\sqrt{K/M}$.

following equation:

$$M \frac{d^2 u_n}{dt^2} = K(u_{n+1} - u_n) - K(u_n - u_{n-1}).$$

The equation mentioned describes the displacement, u_n , of mass "n" relative to its rest position. The first term on the right-hand side of the equation represents the force on mass "n" exerted by the spring on its right, while the second term represents the force exerted by the spring on its left. The behavior of a one-dimensional monoatomic harmonic crystal can be analyzed by solving this equation:

$$M \frac{d^2 u_n}{dt^2} = K(u_{n+1} - 2u_n + u_{n-1}).$$

We look for the solutions to the above equation in the form of propagating waves:

$$u_n = A e^{ikna} e^{i\omega t},$$

where k is a wave number and ω is an angular frequency. Upon inserting a harmonic solution into the equation of motion, we obtain an expression that relates the angular frequency to the wave number,

$$\omega^2 = -\frac{K}{M} \left(e^{\frac{ika}{2}} - e^{-\frac{ika}{2}} \right)^2.$$

By using Euler's formula and the fact that the angular frequency, ω , is a positive value, we can derive the dispersion relation for propagating waves in a one-dimensional harmonic crystal,

$$\omega(k) = \omega_0 \left| \sin k \frac{a}{2} \right|.$$

The upper limit for the angular frequency, ω_0 , is given by $\omega_0 = 2\sqrt{\frac{K}{M}}$. In a monoatomic crystal, the wavelength, $\lambda = \frac{2\pi}{k}$, of waves larger than $2a$ is equivalent to that of waves smaller than $2a$, so the dispersion relation only needs to be represented in the symmetrical interval of $k \in \left[-\frac{\pi}{a}, \frac{\pi}{a}\right]$. This interval is known as the first Brillouin zone of the one-dimensional monoatomic periodic crystal.

The velocity at which the phase of a wave with wave vector k and angular frequency ω propagates is given by the following equation:

$$v_\phi = \frac{\omega}{k}.$$

The group velocity is the velocity at which a wave packet, which is a superposition of propagating waves with different wave numbers over some interval, travels. To understand this concept, consider the superposition of two waves with angular frequencies ω_1 and ω_2 , and wave vectors k_1 and k_2 . If we set $\omega_1 = \omega - \frac{\Delta\omega}{2}$ and $\omega_2 = \omega + \frac{\Delta\omega}{2}$, and $k_1 = k - \frac{\Delta k}{2}$ and $k_2 = k + \frac{\Delta k}{2}$, and assume that both waves have the same amplitude A , then the superposition of these waves leads to the displacement field at mass "n":

$$u_n^s = 2Ae^{ikna} e^{i\omega t} \cos\left(\frac{\Delta k}{2}na + \frac{\Delta\omega}{2}t\right).$$

The first part of the right-hand side of the above equation represents a traveling wave that is modulated by the cosine term, where the latter term represents a beat pulse. The velocity at which this modulation travels is known as the group velocity, and is given by the following equation:

$$v_g = \frac{\Delta\omega}{\Delta k}.$$

In the limit of very small differences in wave number and frequency, the group velocity can be represented as a derivative of the dispersion relation,

$$v_g = \frac{d\omega(k)}{dk}.$$

For a one-dimensional harmonic crystal, the group velocity is expressed as $v_g = \omega_0 \frac{a}{2} \cos k \frac{a}{2}$.

One can picture the 1D diatomic harmonic crystal with alternating masses as shown in Fig. 2.2. The equations of motion of two adjacent odd and even atoms are

$$\begin{aligned} M_1 \ddot{u}_{2n} &= K(u_{2n+1} - u_{2n} + u_{2n-1}), \\ M_2 \ddot{u}_{2n+1} &= K(u_{2n+2} - u_{2n+1} + u_{2n}). \end{aligned}$$

We seek for solutions in the form of propagating waves with different amplitudes for odd and even atoms, as their masses are different.

$$\begin{aligned} u_{2n} &= Ae^{i\omega t} e^{ik2na}, \\ u_{2n+1} &= Be^{i\omega t} e^{ik(2n+1)a}. \end{aligned}$$

The set of two linear equations, in terms of A and B , obtained by inserting the solutions in the form of propagating waves with different amplitudes for odd and

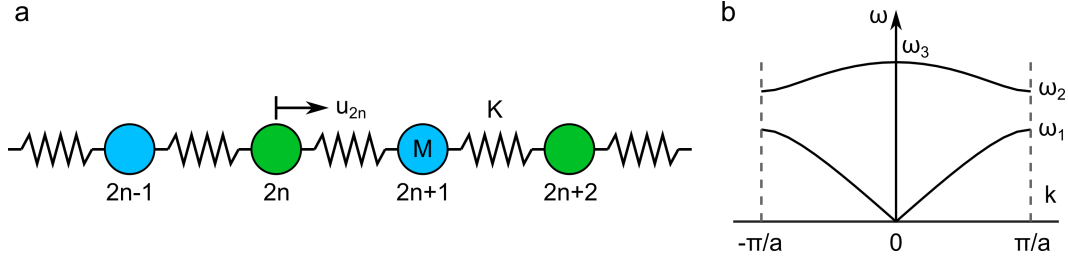


Figure 2.2: Diatomic infinite 1-dimensional mass and spring chain. **a**, Schematics of 1d diatomic chain. **b**, The dispersion curve of 1D diatomic chain in the first Brillouin zone.

even atoms into the equations of motion is:

$$\begin{aligned} (2K - M_1\omega^2)A - 2K \cos kaB &= 0, \\ -2K \cos kaA + (2K - M_2\omega^2)B &= 0. \end{aligned}$$

To find the nontrivial solutions (i.e., where $A \neq 0, B \neq 0$) for this set of equations, we must set the determinant of the matrix composed of the linear coefficients A and B equal to zero. This is an eigenvalue problem in ω^2 , and the resulting equation is:

$$\begin{vmatrix} 2K - M_1\omega^2 & -2K \cos ka \\ -2K \cos ka & 2K - M_2\omega^2 \end{vmatrix} = 0.$$

Setting $\xi = \omega^2$, the above condition takes the form of the quadratic equation:

$$\xi^2 - 2K \left(\frac{1}{M_1} + \frac{1}{M_2} \right) \xi + \frac{4K^2}{M_1M_2} \sin^2 ka = 0,$$

which admits two solutions:

$$\omega^2 = \xi = K \left(\frac{1}{M_1} + \frac{1}{M_2} \right) \pm \sqrt{K^2 \left(\frac{1}{M_1} + \frac{1}{M_2} \right)^2 - \frac{4K^2}{M_1M_2} \sin^2 ka}.$$

The solutions to this equation are periodic in wave number k with a period of π/a . These solutions are depicted in the band structures of Fig. 2.2 over the interval $k \in [0, \pi/2a]$, which is the smallest interval (also known as the irreducible Brillouin zone) for representing the band structure. The complete band structure can be reconstructed by using mirror symmetry with respect to a vertical line passing through the origin.

The frequencies ω_1 , ω_2 , and ω_3 are related to the constants K , M_1 , and M_2 as follows: $\omega_1 = \sqrt{2\frac{K}{M_1}}$, $\omega_2 = \sqrt{2\frac{K}{M_2}}$, and $\omega_3 = \sqrt{2K(\frac{1}{M_1} + \frac{1}{M_2})}$. These frequencies

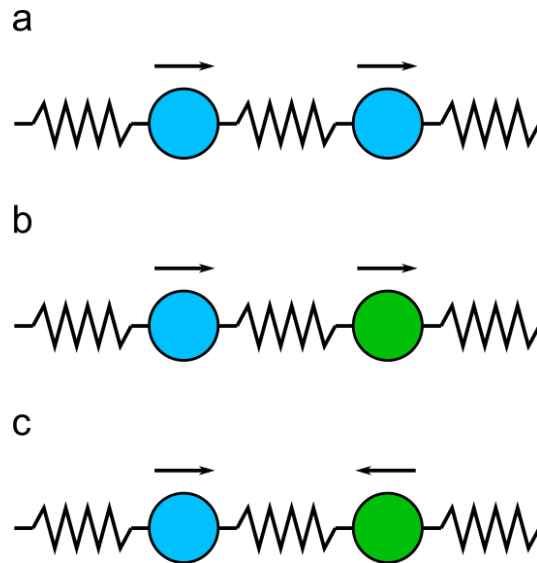


Figure 2.3: Normal modes of 1D monoatomic and diatomic chains. **a**, Normal mode of 1d monoatomic chain. **b**, First normal mode of 1d diatomic chain. **c**, Second normal mode of 1d diatomic chain.

are associated with a band structure, which is divided into two branches for a one-dimensional diatomic crystal that contains two atoms. The two branches are separated by a gap in the frequency range $[\omega_1, \omega_2]$. This gap, also known as a forbidden band or band gap, allows for the existence of complex wavenumber solutions and results in the formation of evanescent waves that decay exponentially.

In a 1D harmonic monoatomic crystal, all of the masses vibrate in sync with one another in a single normal mode (as shown in Figure 2.3a). This normal mode can occur at frequencies below the cutoff frequency, ω_0 . On the other hand, a 1D diatomic chain can have two normal modes (depicted in Figure 2.3). The acoustic branch, which occurs at frequencies below ω_1 , represents a mode where two masses vibrate in phase with each other. The optical branch, which falls between ω_2 and ω_3 , corresponds to a mode where the two masses vibrate out of phase with each other.

2.3 Expansion to higher dimensions

Acoustic metamaterials in 2D and 3D exhibit unique phenomena that are not seen in 1D crystals. Experimentally, 2D crystals typically use rod-shaped structures as the scattering units, while 3D crystals are made up of spheres. Theoretical investigations of periodic acoustic metamaterials often involve studying crystals with scattering units that are simply empty spaces within a matrix. There are various methods of

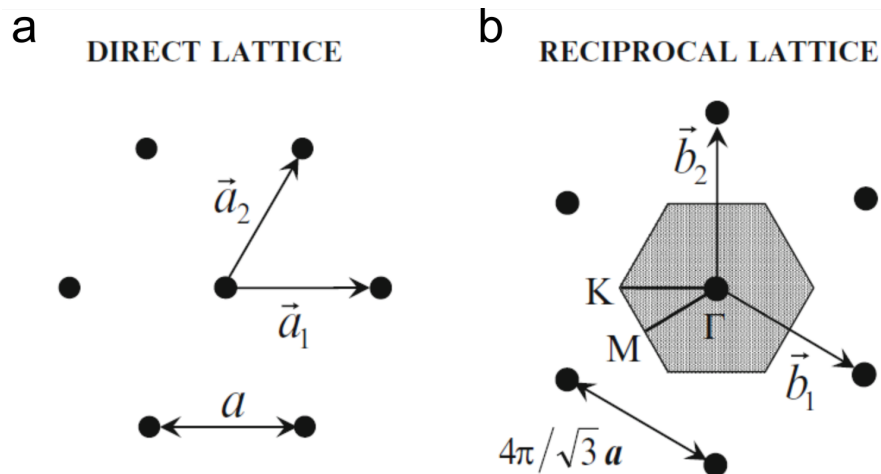


Figure 2.4: 2D periodic acoustic metamaterials **a**, The direct lattices with \vec{a}_1, \vec{a}_2 as primitive vectors. **b**, The reciprocal lattices of the triangular Bravais lattice with \vec{b}_1, \vec{b}_2 as primitive vectors.

creating acoustic metamaterials both theoretically and experimentally, by altering the materials used for the scattering units and host matrix. However, one consistent requirement is that the size of the scattering unit (rod or sphere) and the lattice constant must be similar to the wavelength of the incident radiation in order for the crystal's unique properties to affect the wave passing through it. In other words, the frequency range in which the crystal operates is determined by the size of the scattering unit and the lattice constant. An exception to this rule is resonant sonic materials, which have been shown to have a significant impact on the propagating radiation, even when the wavelength is much larger than the size of the structure [2].

The regular pattern of scattering units in acoustic metamaterials causes multiple scatterings of acoustic or elastic waves, resulting in Bragg reflections. These reflections result in a range of frequencies where waves can propagate through the crystal (pass bands) or be blocked in one or all directions (stop bands or complete band gaps). The width of the band gap is determined by the crystal structure and increases when there is a greater density contrast between the scattering unit material and the host matrix material. Even larger band gaps can be obtained by switching from a liquid to a solid host matrix, such as from water to epoxy, which can support both longitudinal and transverse polarizations [3].

An example of a 2D acoustic metamaterials is a crystal made of cylinders arranged in a triangular Bravais lattice, where the points are at the vertices of equilateral triangles. The diagram in Figure 2.4 shows the direct and reciprocal lattices, with

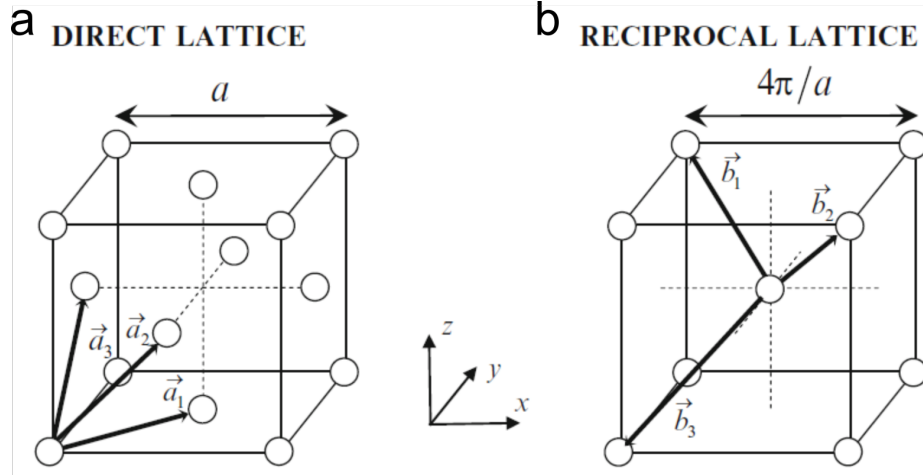


Figure 2.5: 3D acoustic metamaterials **a**, The direct lattices (FCC) with \vec{a}_1 , \vec{a}_2 , and \vec{a}_3 as primitive vectors. **b**, The reciprocal lattices (BCC) of the triangular Bravais lattice with \vec{b}_1 , \vec{b}_2 , and \vec{b}_3 as primitive vectors.

corresponding primitive vectors \vec{a}_1 , \vec{a}_2 and \vec{b}_1 , \vec{b}_2 . Since $|\vec{a}_1| = |\vec{a}_2| = a$, where a is the lattice constant, it can be deduced from the reciprocal lattice vectors definition $\vec{a}_i \cdot \vec{b}_j = 2\pi\delta_{ij}$ that $|\vec{b}_1| = |\vec{b}_2| = 4\pi/\sqrt{3}a$, where δ_{ij} is the Kronecker delta symbol. By calculating the components of \vec{b}_1 and \vec{b}_2 , it can be shown that the reciprocal lattice of a triangular lattice is also a triangular lattice, but rotated by 30° in relation to the direct lattice. Both direct and reciprocal lattices have six-fold symmetry. The first Brillouin zone is shaped like a hexagon, with two main symmetry directions referred to as ΓM and ΓK as shown in Fig. 2.4.

An example of a 3D crystal is a collection of spheres arranged in a face-centered cubic (FCC) structure, which is created by adding a sphere to the center of each face of a cubic unit cell. This structure has a high degree of symmetry, and as such, acoustic metamaterials with this structure have been widely studied both theoretically and experimentally. The direct lattice of the FCC structure and its corresponding reciprocal lattice, which is a body-centered cubic (BCC) crystal structure as illustrated in Fig. 2.5. The sets of primitive vectors \vec{a}_1 , \vec{a}_2 , \vec{a}_3 and \vec{b}_1 , \vec{b}_2 , \vec{b}_3 for both lattices are also displayed. It is evident from the illustration that, with this specific choice of primitive vectors for the direct lattice, $|\vec{a}_1| = |\vec{a}_2| = |\vec{a}_3| = a/\sqrt{2}$, and $|\vec{b}_1| = |\vec{b}_2| = |\vec{b}_3| = 2\sqrt{3}\pi/a$, where a is the length of the cube edge in the direct lattice.

The first Brillouin zone of the FCC lattice is a truncated octahedron and, which is equivalent to the Wigner-Seitz cell of the BCC lattice. It is illustrated in Fig. 2.5a

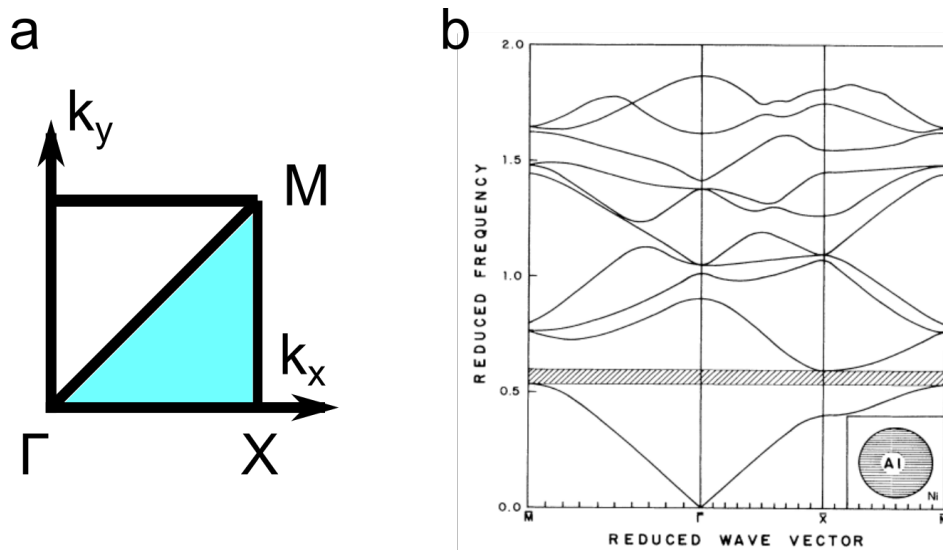


Figure 2.6: Irreducible Brillouin zone and corresponding dispersion curve. a, Schematics of 1d monoatomic chain. **b,** The dispersion curve of 1D monoatomic chain in the first Brillouin zone. ω_0 is the cutoff frequency, defined as $\sqrt{K/M}$.

along with its high symmetry directions. Using the coordinate system in Fig. 2.5b, the coordinates of the high symmetry points (in units of $2\pi/a$) are: Γ (0, 0, 0), X (1, 0, 0), L ($1/2, 1/2, 1/2$), W ($1/2, 1, 0$), and K ($3/4, 3/4, 0$). It can be observed that the direction ΓL is the same as the direction known as [111], which is along the body diagonal of the conventional FCC unit cell, as shown in Fig. 2.5.

The dispersion curve of one of the early examples of 2D acoustic metamaterials is shown in Fig. 2.6 [4]. This system consists of a group of straight, infinite cylinders made of an isotropic solid "a", which is embedded in an elastic, and isotropic background "b". The system has symmetry in the direction parallel to the cylinders (z -direction) and is periodic in the plane perpendicular to the cylinders (transverse plane), this causes waves to be restricted to the transverse plane. The dispersion curve for the first ten phononic bands of aluminum alloy rods in a nickel alloy matrix is shown in figure (Fig. 2.6b). The plots depict the relationship between the normalized frequency ($\omega a/2\pi c_0$) and the normalized Bloch wave vector ($ka/2\pi$), with a being the size of the lattice and c_0 being the speed of transverse wave in the composite material.

The dispersion curve of a 2D crystal shows a phononic band gap between the first two branches, which was found by examining the interior of the irreducible triangle ΓXM of the Brillouin zone (see Fig. 2.6a), as well as its periphery. This gap is present throughout the entire zone, which means that vibrations parallel to the

cylinders cannot travel through the transverse plane. For this crystal, the phononic band gap arises from the periodicity [2, 5, 6], however, other geometrical factors including the placement of resonators can create a forbidden band [7–9], along with the mode hybridization between separate branches causing avoided crossing [10].

2.4 Acoustic metamaterials and material parameters

Acoustics describes how sound waves travel through fluids, such as air or water. One goal of acoustics is to understand how to control the propagation of sound waves, which can be achieved through the use of acoustic metamaterials. In order to control sound waves effectively with acoustic metamaterials, it is necessary to understand the material parameters that influence wave propagation. Linear acoustics is a branch of acoustics that deals with small, low-intensity sound waves that can be described as traveling waves of pressure. One important equation in linear acoustics is based on Newton’s second law of motion, which relates the velocity of a particle, v , to the pressure of a sound wave, p . This equation helps to describe how sound waves propagate through a medium:

$$\rho \frac{\partial v}{\partial t} = -\nabla p.$$

In the context of acoustics, the fluid mass density, ρ , is a key factor that influences the way sound waves propagate through a medium. The continuity equation is a mathematical expression that describes how the motion of a non-flowing, non-viscous fluid is related to its compression and expansion. When analyzing the propagation of acoustic waves, it is often assumed that the process is isentropic, meaning that thermal effects can be neglected and the entropy remains constant. Under these assumptions, the continuity equation can be used to describe the behavior of sound waves in a fluid as follows,

$$\frac{\partial p}{\partial t} + K \nabla \cdot v = 0.$$

The bulk modulus, K , is another factor that plays a role in determining how sound waves propagate through a fluid. It is a measure of the stiffness of the fluid under compression, and it is one of the two key material constants that are needed to describe the behavior of sound waves in a medium. When the equations that describe the fluid mass density and the bulk modulus are combined, it is possible to

derive the scalar wave equation, which describes the pressure, p , of a sound wave as it travels through a fluid:

$$\frac{\partial^2 p}{\partial t^2} = \frac{K}{\rho} \nabla^2 p.$$

The velocity of an acoustic wave, c , is determined by the ratio of the bulk modulus to the fluid mass density as $c = \sqrt{K/\rho}$. The acoustic wave impedance, Z , which describes the relationship between pressure and velocity in a wave, is equal to the square root of the product of the bulk modulus and the fluid mass density ($Z = p/v = \sqrt{K\rho}$). These two parameters, ρ and K are therefore critical in determining the way that sound waves propagate through a medium, and they are the primary focus when designing acoustic metamaterials. It is worth noting that these parameters are similar to the electric permittivity and magnetic permeability, which are the key factors that control the propagation of electromagnetic waves. This analogy has allowed researchers in the field of acoustic metamaterials to borrow concepts and techniques from the field of electromagnetic metamaterials.

2.5 Types of acoustic metamaterials

There are several types of acoustic metamaterials reported since the first report of the first artificial acoustic metamaterial utilized small rubber-coated spheres [2] to create resonant structures that were much smaller than the wavelength of the incident sound waves.

Phononic crystals

Phononic crystals (PCs) are periodic structures that manipulate the propagation of sound waves similar to how photonic crystals [12–14] manipulate the propagation of light. These structures are made of an array of periodic obstacles called scatterers arranged in a regular pattern [2, 5, 6]. The size, shape, and spacing of the scatterers determine the properties of the phononic crystal. When a sound wave encounters a PC, Bragg scattering occurs. This is when the sound wave is reflected by the PC's periodic structure, similar to how X-rays are reflected by a crystal lattice [15]. The reflection occurs when the spacing between the scatterers is equal to a multiple of half the wavelength of the incident sound wave, creating a bandgap, a range of frequencies that the PC does not transmit. This allows the PC to selectively filter and manipulate sound waves. PCs can also exhibit absolute band gaps in their band structure, frequency ranges in which waves cannot travel, similar to photonic

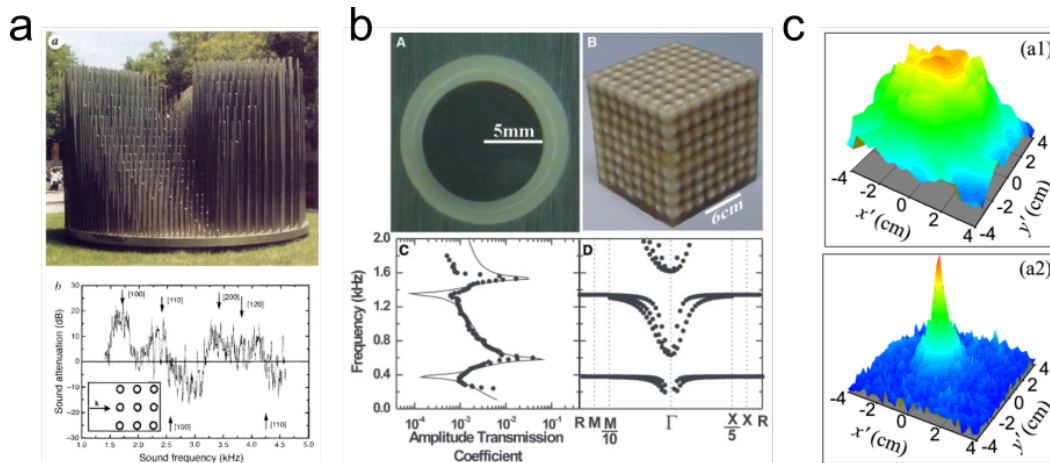


Figure 2.7: Phononic crystals **a**, Kinematic sculpture as an example of phononic crystals. Transmission plot shows attenuations in specific direction [11]. **b**, Array of lead spheres coated with silicone rubber as an example of phononic crystals. Attenuation dips in the transmission curve coincide with the band gaps in the dispersion curve [2]. **c**, Pressure profiles show the focusing of sound in the presence of phononic crystals [5]

band gaps in electromagnetic waves [12]. As a result, PCs can be used in various applications such as noise and vibration isolation [2, 11], acoustic wave guiding [16, 17], and acoustic filters [18, 19]. Additionally, the band structure of PCs can display dispersion curves with a negative slope, leading to negative refraction [5, 20].

Membrane-type acoustic metamaterials

Membrane-type acoustic metamaterials (MAMs) are made of thin, flexible membranes or sheets, typically made of polymer or rubber, suspended within a frame or structure [21–24]. MAMs can be designed and fabricated in various ways to fit specific applications and desired properties. For example, the size, shape, and thickness of the membranes can be adjusted to tune the resonant frequency of the metamaterial, and the spacing between the membranes can be changed to control the interaction with sound waves [21, 25, 26]. MAMs are lightweight and compact materials that can isolate sound at low frequencies beyond the limits of traditional materials, and have the potential to create a new generation of acoustic materials and sensor devices specialized in noise reduction [27].

Helmholtz resonators

Helmholtz resonator-based acoustic metamaterials (HRAMs) use Helmholtz resonators to interact with sound waves in a specific manner [7, 8, 28, 30]. A Helmholtz

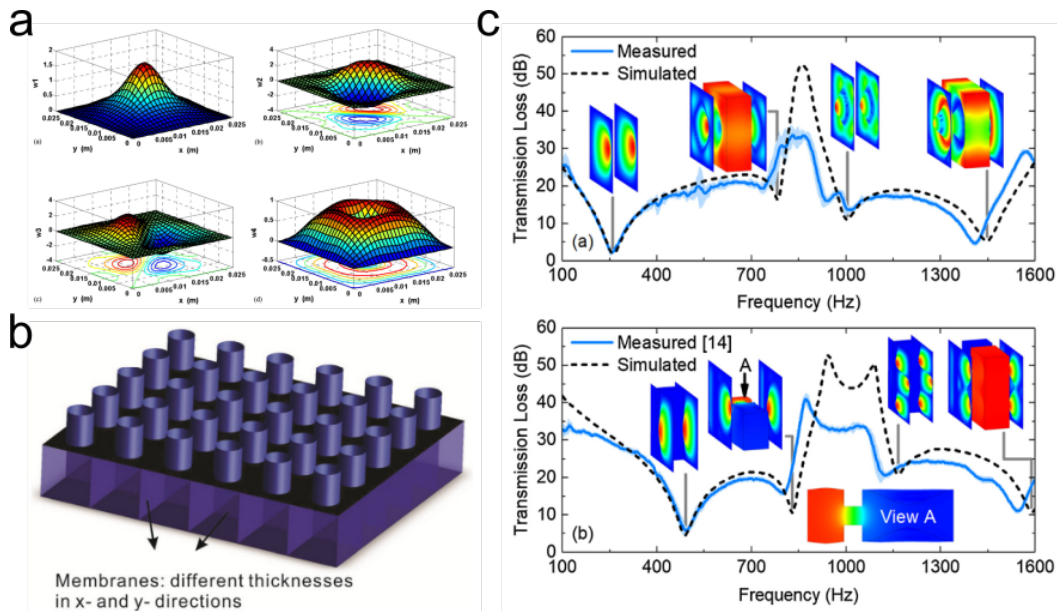


Figure 2.8: Membrane-based acoustic metamaterials **a**, The first four mode shapes of the membrane unit without external loading [21]. **b**, Schematic of the 2D metamaterial layer composed of chambers divided by membranes [22]. **c**, Simulated and measured transmission curves with respect to the mode shapes at the eigenfrequencies [23]

resonator is a small air-filled cavity connected to a tube or pipe that absorbs or reflects sound waves in a specific way when they pass through it. HRAMs are made by arranging a number of Helmholtz resonators in a specific pattern or configuration, such as a regular grid or a more complex pattern [29]. HRAMs have the ability to interact with sound waves in a very attenuative way, allowing them to be used for a variety of applications, including absorbing [28, 30] specific frequencies of sound, and creating "acoustic black holes," areas where sound waves are completely absorbed [31].

Negative parameters

The concept of negative mass [9, 24, 32, 34, 35] and/or negative stiffness [33, 36] can be introduced to design acoustic metamaterials. In general, mass and stiffness are properties that describe how a material responds to external forces. Mass refers to the amount of matter in an object, and stiffness refers to the resistance of an object to being deformed when it is subjected to a force. In the case of acoustic metamaterials, these properties can be engineered to be negative, which can result in unusual wave propagation behavior. For example, a material with negative mass

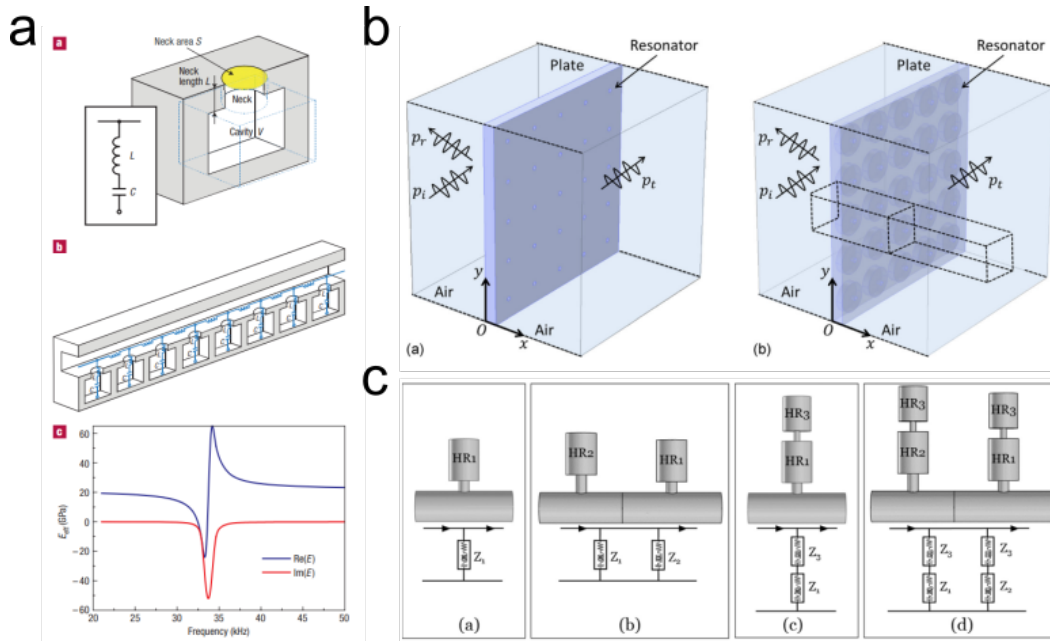


Figure 2.9: Acoustic metamaterials with Helmholtz resonators **a**, Schematics of Helmholtz resonator-based acoustic metamaterials. The effective stiffness of the metamaterials is negative at specific frequency range [7]. **b**, Schematic views of an acoustic metamaterial plate periodically embedded with resonators [28]. **c**, Acoustic metamaterials can be composed of different configurations using multiple Helmholtz resonators [29].

will accelerate in the opposite direction of an applied force, while a material with negative stiffness will become more deformable when subjected to a force.

Negative mass can be achieved through the use of resonant elements or structures that are designed to have negative effective mass [7, 9, 32, 35]. These resonant elements can interact with incident sound waves in such a way that they effectively have negative mass. A material with negative mass can mitigate the reflection of sound waves [[40], or achieve superlensing of acoustic waves [9]. On the other hand, negative stiffness can be achieved through the use of resonant elements or structures that are designed to have negative effective stiffness [33, 34, 36]. These resonant elements can interact with incident sound waves in such a way that they effectively have negative stiffness. Acoustic metamaterials with negative stiffness have the potential to be used in a variety of applications with their unusual absorption properties [28].

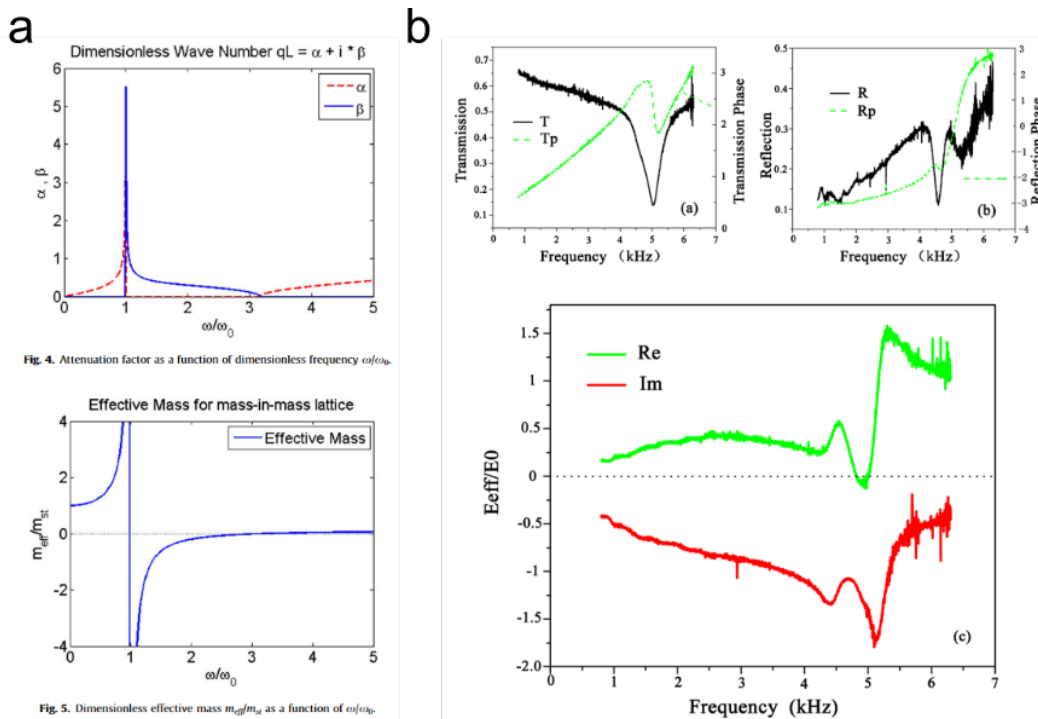


Figure 2.10: Acoustic metamaterials with negative parameters **a**, The effective mass of the mass-in-mass lattice becomes negative across the narrow frequency range, and it affects the attenuation coefficients of the acoustic metamaterials [32]. **b**, The effective modulus of the split hollow sphere is below zero around 5 kHz, significantly affecting the wave properties [33].

Chirality

Chiral acoustic metamaterials are materials that exhibit specific acoustic properties related to their chirality, or handedness, which is the property of a material or object that is not superimposable on its mirror image. Chiral materials have demonstrated a number of unique properties that make them useful in various industrial applications [41]. They have been shown to support band gap and mode tunability [37, 42], as well as exhibit negative thermal expansion [43, 44] and high impact absorption [45]. These properties make them suitable for use in applications such as airfoil stability [46] and catheters [47]. Recently, 3D chiral mechanical metamaterials have been developed and their dynamic properties have been studied, revealing distinctive wave modes [38, 48]. The role of centrosymmetry in chiral metamaterials and its impact on wave propagation has also been investigated [39].

Nonreciprocity

One area of active acoustic metamaterials research is the development of non-reciprocal metamaterials, which allow for the breaking of time-reversal symmetry

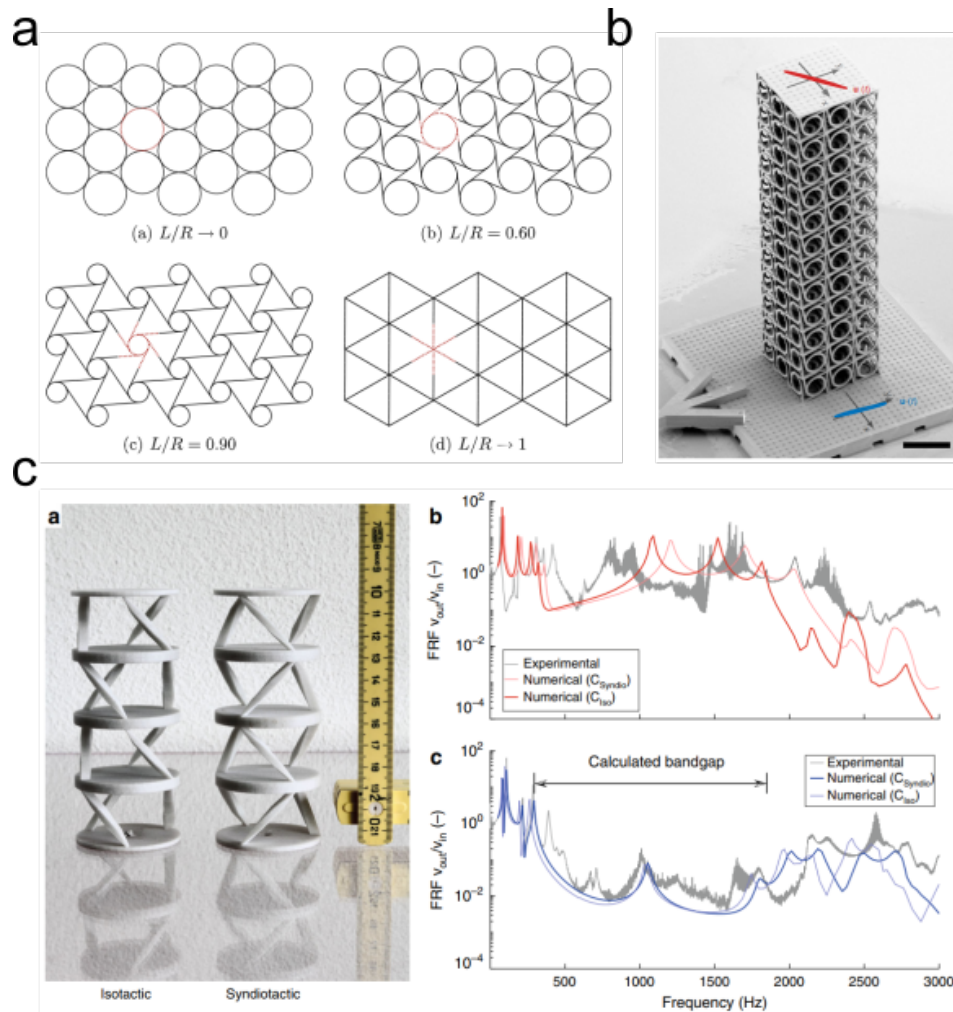


Figure 2.11: Chiral acoustic metamaterials **a**, Various configurations of 2D chiral acoustic metamaterials [37]. **b**, Microscale 3D chiral acoustic metamaterials tested for ultrasound transmission [38]. **c**, Chiral acoustic metamaterials show distinctive wave characteristics with respect to the tacticity of the structure [39].

[49] and enable one-way propagation and isolation [50, 51]. Nonreciprocity is the property of a material or system that behaves differently when sound waves propagate through it in opposite directions, such as a material that is transparent to sound waves in one direction but highly reflective to sound waves in the opposite direction. This can be achieved by designing the material with asymmetric structures or elements that interact differently with sound waves based on the direction of propagation. In conventional materials, sound travels symmetrically, meaning that it is possible to transmit a signal from one location to another and transmit the same intensity of sound in the opposite direction due to the time-reversibility of wave propagation in these materials. Non-reciprocal metamaterials can enable full-duplex sound

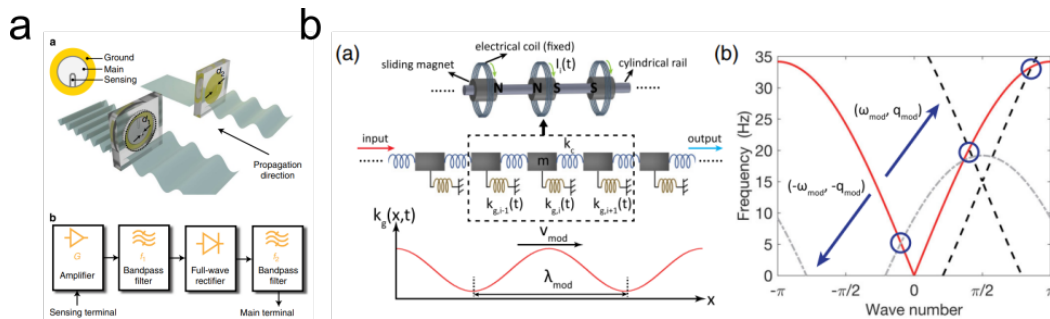


Figure 2.12: Nonreciprocal acoustic metamaterials **a**, Schematic of nonreciprocal behavior, which is enabled with piezoelectric materials driven by nonlinear electric circuit [49]. **b**, Electrically controlled magnets form nonreciprocal acoustic metamaterials. Spatio-temporal modulation shifts the original dispersion curves in k -space [50].

communication [53], where it is possible to transmit and receive acoustic signals from the same transducer on the same frequency channel. Non-reciprocal acoustic metamaterials have the potential to be used in applications such as directional transparency [54] or to develop more efficient sonar [55].

Active acoustic metamaterials

There has been a growing interest in active acoustic metamaterials, which have the potential to address the limitations of traditional metamaterials and enhance their effectiveness in various applications. These materials typically contain elements that can move or change shape in response to external stimuli, such as an electric current [51] or a magnetic field [52], and can be controlled or external pneumatic actuation [30]. Active unit cells, which provide energy to an incoming wave and feedback to the acoustic system, have been used in designs to create metamaterials with unique acoustic properties. These designs allow for reconfigurability and real-time tunability, and can be made using active transducers [56], micro or nanoelectromechanical systems [57, 58], piezoelectric materials [59], and electrically loaded acoustic elements [60].

Manufacturing techniques

There are a variety of new manufacturing techniques that are being developed for producing metamaterials, including:

- 3D printing [61]: This technique allows for the rapid prototyping and production of metamaterials with complex shapes and structures. 3D printing can

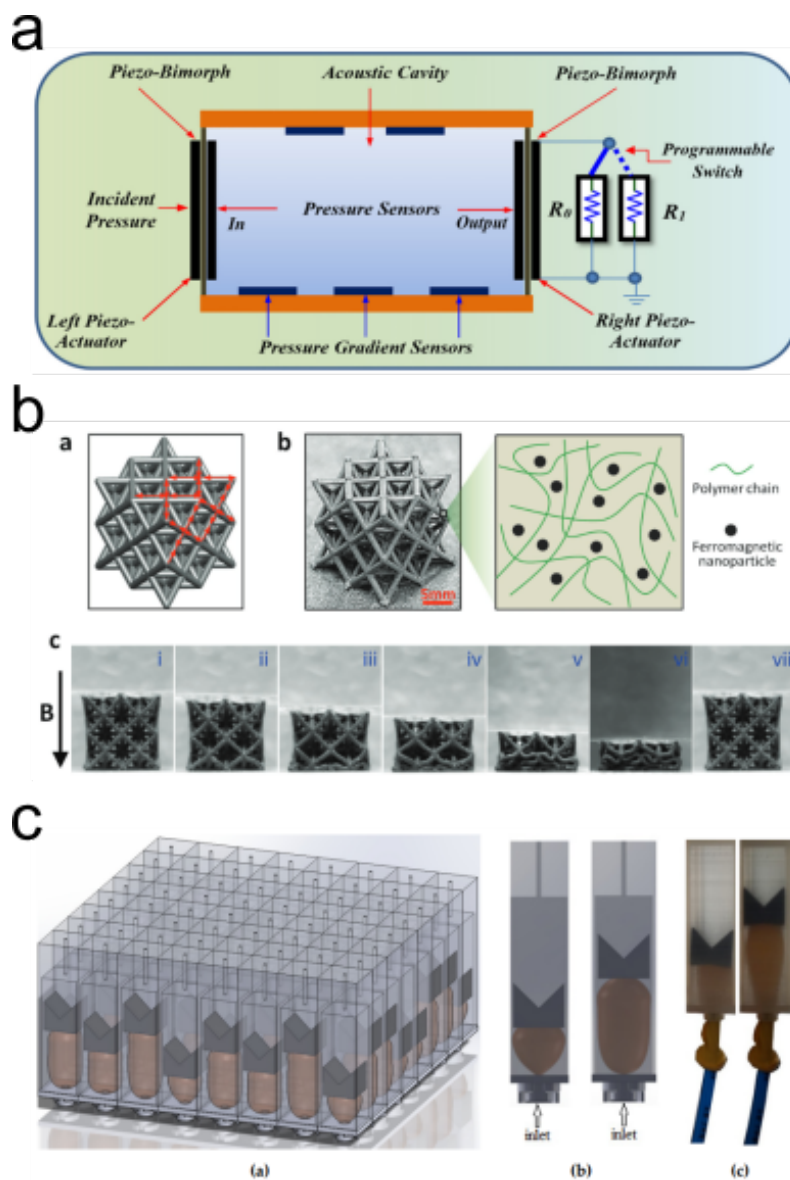


Figure 2.13: Active acoustic metamaterials **a**, Schematic of active nonreciprocal acoustic metamaterials activated by piezo-switch driven by electric circuit [51]. **b**, 3D-printed octet lattices are magnetically actuated to change their configuration and also wave properties [52]. **c**, Individual Helmholtz resonators are actuated by hydraulic force to alter their resonance frequency [30].

be used to produce metamaterials made from a variety of materials, including metals, plastics, and ceramics.

- Nanolithography [57, 58]: This technique involves the use of specialized tools and processes to pattern materials at the nanoscale, which can be used to create metamaterials with subwavelength features.
- Self-assembly [62, 63]: This technique involves the use of materials that can spontaneously organize themselves into specific structures or patterns, which can be used to create metamaterials with specific properties.
- Electrospinning [64, 65]: This technique involves the use of an electric field to spin a polymer solution into fibers, which can be used to create metamaterials with a variety of shapes and structures.
- Soft lithography [66]: This technique involves the use of a mold or stamp to transfer patterns onto a soft material, which can then be used to create metamaterials with specific shapes and features.

Permissions

Figure 2.4(a,b) obtained from [1]. Permission to reproduce the figures is not required for non-commercial and educational use.

Figure 2.5(a,b) obtained from [1]. Permission to reproduce the figures is not required for non-commercial and educational use.

Figure 2.6(b) obtained from [4]. Permission to reproduce the figures is not required for non-commercial and educational use.

Figure 2.7(a-c) obtained from [2, 5, 11]. Permission to reproduce the figures is not required for non-commercial and educational use.

Figure 2.8(a-c) obtained from [21–24]. Permission to reproduce the figures is not required for non-commercial and educational use.

Figure 2.9(a-c) obtained from [7, 28, 29]. Permission to reproduce the figures is not required for non-commercial and educational use.

Figure 2.10(a,b) obtained from [32, 33]. Permission to reproduce the figures is not required for non-commercial and educational use.

Figure 2.11(a-c) obtained from [37–39]. Permission to reproduce the figures is not required for non-commercial and educational use.

Figure 2.12(a,b) obtained from [49, 50]. Permission to reproduce the figures is not required for non-commercial and educational use.

Figure 2.13(a-c) obtained from [30, 51, 52]. Permission to reproduce the figures is not required for non-commercial and educational use.

References

1. Pierre A. Deymier, L. D. in *Acoustic Metamaterials and Phononic Crystals* (ed Deymier, P. A.) 13–44 (Springer, 2013).
2. Liu, Z. *et al.* Locally Resonant Sonic Materials. *Science* **289**, 1734–1736 (2000).
3. Page, J. *et al.* in *Wave Scattering in Complex Media: From Theory to Applications* (eds Tiggelen, B. A. & Skipetrov, S. E.) 283–307 (Kluwer Academic Publishers: NATO Science Series, 2003).
4. Kushwaha, M. S., Halevi, P., Dobrzynski, L. & Djafari-Rouhani, B. Acoustic band structure of periodic elastic composites. *Physical Review Letters* **71**, 2022–2025 (1993).
5. Yang, S. *et al.* Focusing of Sound in a 3D Phononic Crystal. *Physical Review Letters* **93**, 024301 (2004).
6. Page, J. H. *et al.* Phononic crystals. *physica status solidi (b)* **241**, 3454–3462 (2004).
7. Fang, N. *et al.* Ultrasonic metamaterials with negative modulus. *Nature Materials* **5**, 452–456 (2006).
8. Hu, X., Ho, K.-M., Chan, C. T. & Zi, J. Homogenization of acoustic metamaterials of Helmholtz resonators in fluid. *Physical Review B* **77**, 172301 (2008).
9. Ambati, M., Fang, N., Sun, C. & Zhang, X. Surface resonant states and super-lensing in acoustic metamaterials. *Physical Review B* **75**, 195447 (2007).
10. Mace, B. R. & Manconi, E. Wave motion and dispersion phenomena: Veering, locking and strong coupling effects. *The Journal of the Acoustical Society of America* **131**, 1015–1028 (2012).
11. Martínez-Sala, R. *et al.* Sound attenuation by sculpture. *Nature* **378**, 241 (1995).
12. Yablonovitch, E. Photonic Crystals. *Journal of Modern Optics* **41**, 173–194 (1994).
13. Joannopoulos, J. D., Villeneuve, P. R. & Fan, S. Photonic crystals. *Solid State Communications* **102**, 165–173 (1997).

14. Elser, D. *et al.* Reduction of Guided Acoustic Wave Brillouin Scattering in Photonic Crystal Fibers. *Physical Review Letters* **97**, 133901 (2006).
15. Bragg, W. H. & Bragg, S. W. L. *X-rays and Crystal Structure* (G. Bell and Sons, Limited, 1915).
16. Khelif, A., Choujaa, A., Benchabane, S., Djafari-Rouhani, B. & Laude, V. Guiding and bending of acoustic waves in highly confined phononic crystal waveguides. *Applied Physics Letters* **84**, 4400–4402 (2004).
17. Otsuka, P. H. *et al.* Broadband evolution of phononic-crystal-waveguide eigenstates in real- and k-spaces. *Scientific Reports* **3**, 3351 (2013).
18. Qiu, C., Liu, Z., Mei, J. & Shi, J. Mode-selecting acoustic filter by using resonant tunneling of two-dimensional double phononic crystals. *Applied Physics Letters* **87**, 104101 (2005).
19. Ji, P., Hu, W. & Yang, J. Development of an acoustic filter for parametric loudspeaker using phononic crystals. *Ultrasonics* **67**, 160–167 (2016).
20. Ke, M. *et al.* Negative-refraction imaging with two-dimensional phononic crystals. *Physical Review B* **72**, 064306 (2005).
21. Zhang, Y., Wen, J., Xiao, Y., Wen, X. & Wang, J. Theoretical investigation of the sound attenuation of membrane-type acoustic metamaterials. *Physics Letters A* **376**, 1489–1494 (2012).
22. Huang, T.-Y., Shen, C. & Jing, Y. Membrane- and plate-type acoustic metamaterials. *The Journal of the Acoustical Society of America* **139**, 3240–3250 (2016).
23. Ang, L. Y. L., Koh, Y. K. & Lee, H. P. Plate-type acoustic metamaterials: Evaluation of a large-scale design adopting modularity for customizable acoustical performance. *Applied Acoustics* **149**, 156–170 (2019).
24. Yang, Z., Mei, J., Yang, M., Chan, N. H. & Sheng, P. Membrane-Type Acoustic Metamaterial with Negative Dynamic Mass. *Physical Review Letters* **101**, 204301 (2008).
25. Naify, C. J., Chang, C.-M., McKnight, G. & Nutt, S. Transmission loss and dynamic response of membrane-type locally resonant acoustic metamaterials. *Journal of Applied Physics* **108**, 114905 (2010).
26. Wang, X., Zhao, H., Luo, X. & Huang, Z. Membrane-constrained acoustic metamaterials for low frequency sound insulation. *Applied Physics Letters* **108**, 041905 (2016).
27. Gao, N. *et al.* Acoustic Metamaterials for Noise Reduction: A Review. *Advanced Materials Technologies* **7**, 2100698 (2022).
28. Yamamoto, T. Acoustic metamaterial plate embedded with Helmholtz resonators for extraordinary sound transmission loss. *Journal of Applied Physics* **123**, 215110 (2018).

29. Jena, D. P., Dandsena, J. & Jayakumari, V. G. Demonstration of effective acoustic properties of different configurations of Helmholtz resonators. *Applied Acoustics* **155**, 371–382 (2019).
30. Hedayati, R. & Lakshmanan, S. Pneumatically-Actuated Acoustic Metamaterials Based on Helmholtz Resonators. *Materials* **13**, 1456 (2020).
31. Pelat, A., Gautier, F., Conlon, S. C. & Semperlotti, F. The acoustic black hole: A review of theory and applications. *Journal of Sound and Vibration* **476**, 115316 (2020).
32. Huang, H. H., Sun, C. T. & Huang, G. L. On the negative effective mass density in acoustic metamaterials. *International Journal of Engineering Science* **47**, 610–617 (2009).
33. Ding, C. (, Hao, L. (& Zhao, X. (Two-dimensional acoustic metamaterial with negative modulus. *Journal of Applied Physics* **108**, 074911 (2010).
34. Lee, S. H., Park, C. M., Seo, Y. M., Wang, Z. G. & Kim, C. K. Acoustic metamaterial with negative modulus. *Journal of Physics: Condensed Matter* **21**, 175704 (2009).
35. Man, X., Luo, Z., Liu, J. & Xia, B. Hilbert fractal acoustic metamaterials with negative mass density and bulk modulus on subwavelength scale. *Materials & Design* **180**, 107911 (2019).
36. Lee, S. H. & Wright, O. B. Origin of negative density and modulus in acoustic metamaterials. *Physical Review B* **93**, 024302 (2016).
37. Spadoni, A., Ruzzene, M., Gonella, S. & Scarpa, F. Phononic properties of hexagonal chiral lattices. *Wave Motion* **46**, 435–450 (2009).
38. Frenzel, T., Köpfler, J., Jung, E., Kadic, M. & Wegener, M. Ultrasound experiments on acoustical activity in chiral mechanical metamaterials. *Nature Communications* **10**, 1–6 (2019).
39. Bergamini, A. *et al.* Tacticity in chiral phononic crystals. *Nature Communications* **10**, 1–8 (2019).
40. Park, C. M. & Lee, S. H. Zero-reflection acoustic metamaterial with a negative refractive index. *Scientific Reports* **9**, 3372 (2019).
41. Wu, W. *et al.* Mechanical design and multifunctional applications of chiral mechanical metamaterials: A review. *Materials & Design* **180**, 107950 (2019).
42. Spadoni, A. & Ruzzene, M. Structural and Acoustic Behavior of Chiral Truss-Core Beams. *Journal of Vibration and Acoustics* **128**, 616–626 (2006).
43. Lakes, R. Cellular solid structures with unbounded thermal expansion. *Journal of Materials Science Letters* **15**, 475–477 (1996).
44. Ha, C. S., Hestekin, E., Li, J., Plesha, M. E. & Lakes, R. S. Controllable thermal expansion of large magnitude in chiral negative Poisson's ratio lattices. *physica status solidi (b)* **252**, 1431–1434 (2015).

45. Spadoni, A., Ruzzene, M. & Scarpa, F. Global and local linear buckling behavior of a chiral cellular structure. *physica status solidi (b)* **242**, 695–709 (2005).
46. Bornengo, D., Scarpa, F. & Remillat, C. Evaluation of hexagonal chiral structure for morphing airfoil concept. *Proceedings of the Institution of Mechanical Engineers, Part G: Journal of Aerospace Engineering* **219**, 185–192 (2005).
47. Wu, W. *et al.* Mechanical properties of hierarchical anti-tetrachiral metastructures. *Extreme Mechanics Letters* **16**, 18–32 (2017).
48. Frenzel, T., Kadic, M. & Wegener, M. Three-dimensional mechanical metamaterials with a twist. *Science* **358**, 1072–1074 (2017).
49. Popa, B.-I. & Cummer, S. A. Non-reciprocal and highly nonlinear active acoustic metamaterials. *Nature Communications* **5**, 3398 (2014).
50. Wang, Y. *et al.* Observation of Nonreciprocal Wave Propagation in a Dynamic Phononic Lattice. *Physical Review Letters* **121**, 194301 (2018).
51. Baz, A. Active nonreciprocal acoustic metamaterials using a switching controller. *The Journal of the Acoustical Society of America* **143**, 1376–1384 (2018).
52. Yu, K., Fang, N. X., Huang, G. & Wang, Q. Magnetoactive Acoustic Metamaterials. *Advanced Materials* **30**, 1706348 (2018).
53. Alu, A., Wiederhold, C., Quan, L. & Sounas, D. Non-reciprocal acoustic metamaterials for full-duplex communications and imaging. *The Journal of the Acoustical Society of America* **142**, 2682–2682 (2017).
54. Raval, S., Petrover, K. & Baz, A. Experimental characterization of a one-dimensional nonreciprocal acoustic metamaterial with anti-parallel diodes. *Journal of Applied Physics* **129**, 074502 (2021).
55. Adlakha, R., Moghaddaszadeh, M., Attarzadeh, M. A., Aref, A. & Nouh, M. Frequency selective wave beaming in nonreciprocal acoustic phased arrays. *Scientific Reports* **10**, 21339 (2020).
56. Lani, S. W., Wasequr Rashid, M., Hasler, J., Sabra, K. G. & Levent Degertekin, F. Capacitive micromachined ultrasonic transducer arrays as tunable acoustic metamaterials. *Applied Physics Letters* **104**, 051914 (2014).
57. Cha, J., Kim, K. W. & Daraio, C. Experimental realization of on-chip topological nanoelectromechanical metamaterials. *Nature* **564**, 229–233 (2018).
58. Cha, J. & Daraio, C. Electrical tuning of elastic wave propagation in nanomechanical lattices at MHz frequencies. *Nature Nanotechnology* **13**, 1016–1020 (2018).
59. Jin, Y., Bonello, B. & Pan, Y. Acoustic metamaterials with piezoelectric resonant structures. *Journal of Physics D: Applied Physics* **47**, 245301 (2014).

60. Fleury, R., Sounas, D. & Alù, A. An invisible acoustic sensor based on parity-time symmetry. *Nature Communications* **6**, 5905 (2015).
61. Hedayati, R. & Bodaghi, M. Acoustic Metamaterials and Acoustic Foams: Recent Advances. *Applied Sciences* **12**, 3096 (2022).
62. Brunet, T., Leng, J. & Mondain-Monval, O. Soft Acoustic Metamaterials. *Science* **342**, 323–324 (2013).
63. Khanolkar, A. *et al.* A self-assembled metamaterial for Lamb waves. *Applied Physics Letters* **107**, 071903 (2015).
64. Liu, H. & Zuo, B. Structure and Sound Absorption Properties of Spiral Vane Electrospun PVA/PEO Nanofiber Membranes. *Applied Sciences* **8**, 296 (2018).
65. Wang, Y., Guo, J., Fang, Y., Zhang, X. & Yu, H. Ultralight Metamaterial for Sound Absorption Based on Miura-Ori Tessellation Structures. *Advanced Engineering Materials* **23**, 2100563 (2021).
66. Choi, C., Bansal, S., Münzenrieder, N. & Subramanian, S. Fabricating and Assembling Acoustic Metamaterials and Phononic Crystals. *Advanced Engineering Materials* **23**, 2000988 (2021).

Chapter 3

1D WAVE PROPAGATION IN ACOUSTIC METAMATERIALS: HELICAL METAMATERIALS AND MODE HYBRIDIZATION

This chapter is adapted from:

G. Kim, K.M.Y. Coimbra, & C. Daraio. "Mode Hybridization in DNA-Inspired Helical Metamaterials with Variable Centro-asymmetry". *Applied Physics Letters* **121**, 072201 (2022).

CONTRIBUTIONS: Conceived the project and generated the idea, designed and characterized the models via finite element analysis, fabricated the samples, conducted the transmission experiments, analyzed the data, and wrote the manuscript.

3.1 Chapter summary

This chapter presents an extensive study of 1D wave propagation in acoustic metamaterials. Through this research, a comprehensive understanding of the dispersion curves and mode shapes of the vibrational modes of the helical metamaterials has been developed.

Specifically, we study helical acoustic metamaterials and demonstrate the ability to vary the materials' dispersion properties by controlling geometrical structure and mass distribution. By locally adding eccentric, higher density elements in the unit cells, we perturb the moment of inertia of the system and introduce centro-asymmetry. This allows controlling the degree of mode coupling and the width of subwavelength band gaps in the dispersion relation, which are the product of enhanced local resonance hybridization. We characterize the distinct normal modes in our metamaterials using finite element simulations and analytically quantify the coupling between each mode. The evolution of acoustic band gaps induced by the increasing level of centro-asymmetry is experimentally validated with 3D-printed structures.

3.2 Introduction

Phononic crystals (PCs) and acoustic metamaterials (MMs) are rationally designed structured materials that can be engineered to control the propagation of acoustic and elastic waves. Traveling waves are reflected [1–3], transmitted [4], or guided [5,

6], depending on the geometry [7, 8], stiffness [9, 10], and structural composition [11]. Frequency bands of forbidden wave propagation (band gaps) can be created by introducing Bragg scattering phenomena [12, 13] or resonant structures [14, 15]. Variations in the geometry or elastic modulus, achieved with electrical [16], piezoelectric [17], and mechanical stimuli [7, 10] or via enhanced coupling between different vibrational modes [18], have been used to manipulate the location and width of band gaps.

PCs and MMs have been shown to present large controllability of their vibration and sound attenuation with structural elements that undergo deformations, like deflection or buckling [7, 19]. Among these, chiral materials have been recently shown to support band gap and mode tunability [20, 21], and they have also been studied for their unique mechanical properties [22], like negative thermal expansion [23, 24] and high impact absorption [25]. Chiral materials can be suggested as solutions for a number of industrial applications [22], like airfoil stability [26] and catheters [27]. Recently, a new design of 3D chiral mechanical metamaterials has emerged and their dynamic properties have been characterized, showing distinctive wave modes, such as lifted degeneracy of two circularly polarized eigenmodes [28, 29]. The role of centrosymmetry in chiral metamaterials and its effects on wave propagating properties have also been investigated in the context of tacticity [30].

In this chapter, we studied the dynamic characteristics of 3D-printed, chiral materials with a helicoidal shape (herein defined as helical metamaterials, or HMMs). The HMMs were fabricated using a single acrylic polymer with added masses. We designed their architecture to accommodate for centro-asymmetry, which allows for mode coupling and subwavelength band gap formation. Leveraging these characteristics, we provided experimental evidence for the control of the HMMs' modal response and frequency band gaps, making them a promising new class of materials for vibration isolation.

3.3 DNA-inspired design of the helical metamaterials (HMMs)

Inspired by the helicoidal configuration of Bouligand structures [31, 32] and DNA [33] (Fig. 3.1a), we designed and studied a chiral structure consisting of horizontal beams, with radius $r_{hor} = 2.5$ mm and length $l_{hor} = 25$ mm, connected by thin, linear elastic pillars, with radius $r_{ver} = 1.25$ mm and length $l_{ver} = 6.6$ mm. These HMMs can be represented by a classical mass-spring system, where the horizontal beams function as discrete "masses" and the connecting pillars function as "springs". To

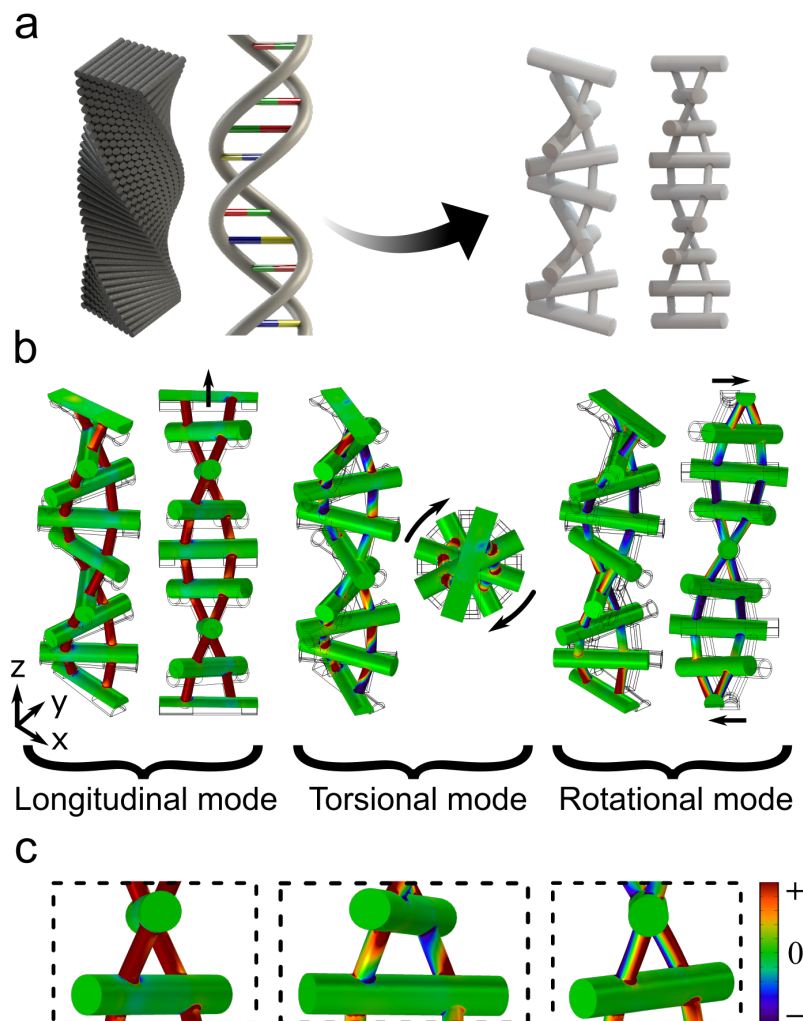


Figure 3.1: Schematic of the samples' geometry and vibrational modes. **a**, HMMs are inspired by Bouligand structures and the shape and aspect ratio of DNA molecules. **b**, Normal modes of HMMs excited by a plane wave in the z -direction: longitudinal (left: isometric, right: side view), torsional (left: isometric, right: top view), and degenerate rotational mode (left: isometric, right: side view). Coordinate system indicates the coordinates of the isometric view. Black lines show the reference positions. **c**, Truncated unit cells show different deformation behavior of the connecting beams for each mode. The color shows volumetric strain distribution, where red indicates expansion and blue represents compression.

ensure linear elastic interactions, we designed pillars that were 10 times lighter than the horizontal masses. Two connecting pillars, spaced 6.25 mm apart, were included between each beam for structural stability. To induce chirality, we rotated each mass-beam 45° with respect to its adjacent beam. We implemented the finite element method (FEM), to numerically analyze the normal modes of our metamaterials (COMSOL Multiphysics[®]). The normal modes of the HMMs excited by a plane wave traveling in the z -direction are shown in Fig. 3.1b. The colors in Fig. 3.1b,c represent volumetric strain distribution, which shows that the deformation is mostly concentrated on the connecting pillars. The longitudinal mode represents the motion parallel to the vertical axis, whereas the torsional mode generates a propagating twist. The strain distribution shows that the connecting pillars undergo tension and compression for the longitudinal mode, whereas they twist under the torsional mode. Because of the structure's chiral nature, expansion and compression of the longitudinal mode stimulate the torsional behavior of the HMMs, and vice versa. The rotational mode corresponds to a flexural mode, which bends the connecting pillars as they deform, while the chirality induces a propagating rotational wave around the central axis.

3.4 Effect of centrosymmetry on the acoustic properties of the HMMs

Dispersion curves of centro-asymmetric HMMs

To analyze the effects of centrosymmetry on the acoustic characteristics of the HMMs, we adjusted the center of mass of the horizontal beams, by inserting high-density stainless steel cylinders ($\rho = 7800 \text{ kg/m}^3$) in pre-cut holes on the beams' core. These high-density inserts are roughly 7 times heavier than the base material used for the beams and connecting pillars (VeroWhite, $\rho = 1165 \text{ kg/m}^3$, Stratasys[™]). When additional high-density inserts are arranged in one end of the beams, the beam's overall center of mass (red point) shifts further away from the central axis (white cross) of the HMMs (Fig. 3.2a-c). In all examples, we maintained the total mass and volume of the samples constant, by only re-positioning the steel inserts. We derived the respective dispersion curves with normalized frequency and wavenumber (Fig. 3.2d-f) using the FE model under the 1D Bloch periodic boundary condition. The frequency is normalized by the characteristic frequency of the longitudinal mode, which is the square root of the compressive stiffness divided by the mass of the horizontal cylinder. The wavenumber ranges from 0 to π/a_{HMM} , where a_{HMM} is the height of the unit cell ($a_{HMM} = 8 \text{ cm}$). The different colored lines represent different wave modes, which are determined numerically.

We used normalized volume-averaged displacements and curls to categorize the data points into longitudinal, torsional, and rotational modes. The blue line with \times markers represents the dispersion characteristics of longitudinal waves. We identified the longitudinal mode by filtering through the modes with the normalized z -displacements greater than $\sqrt{2/3}$. Unsurprisingly, we note that longitudinal waves travel at the fastest speed, in comparison to other modes. The torsional mode (black circles) is the second fastest wave propagating through the structure, which is filtered by the higher volume-averaged curls ($> 1/\sqrt{3}$) and the smaller volume-averaged displacements ($< 1/\sqrt{2}$) in the z -direction. The slowest rotational mode (red asterisks) splits into two orthogonal modes, which arise from the chirality of the structure. The rotational modes are characterized by the larger lateral displacements, greater than $1/\sqrt{3}$, perpendicular to the central axis. For right-handed HMMs, a flexural wave rotating in the counter-clockwise direction interacts with other modes and creates partial band gaps. A clockwise rotating flexural wave has minimal coupling with different modes and remains undisturbed even with strong centro-symmetry. Other data points which do not fall into above-mentioned categories are defined as transitional modes.

Dispersion curve analysis

In the centrosymmetric structure, no apparent coupling between the existing modes is observed in the low frequency range (Fig. 3.1d). As the structures become more centro-asymmetric, coupling between the different modes gets stronger and sub-wavelength longitudinal band gaps emerge due to local resonance of the constituent elements [34]. We adopted a ladder-like metamaterials model [35], to investigate the HMMs analytically and quantify the coupling spring constant γ between the longitudinal mode and the rest of the modes. The coupling constant gradually changes from 0 to 2.08 to 3.00 with increasing centro-asymmetry. We observed the widening of a longitudinal band gap with enhanced coupling. The analytical model captures the slope of two branches that forms the longitudinal band gap, and shows the veering phenomena between the longitudinal mode and the torsional mode [36]. However, the model is based on two parallel mass-spring chains that are only allowed to move in a single dimension, which explains why it cannot fully grasp the complexity of the numerical solution.

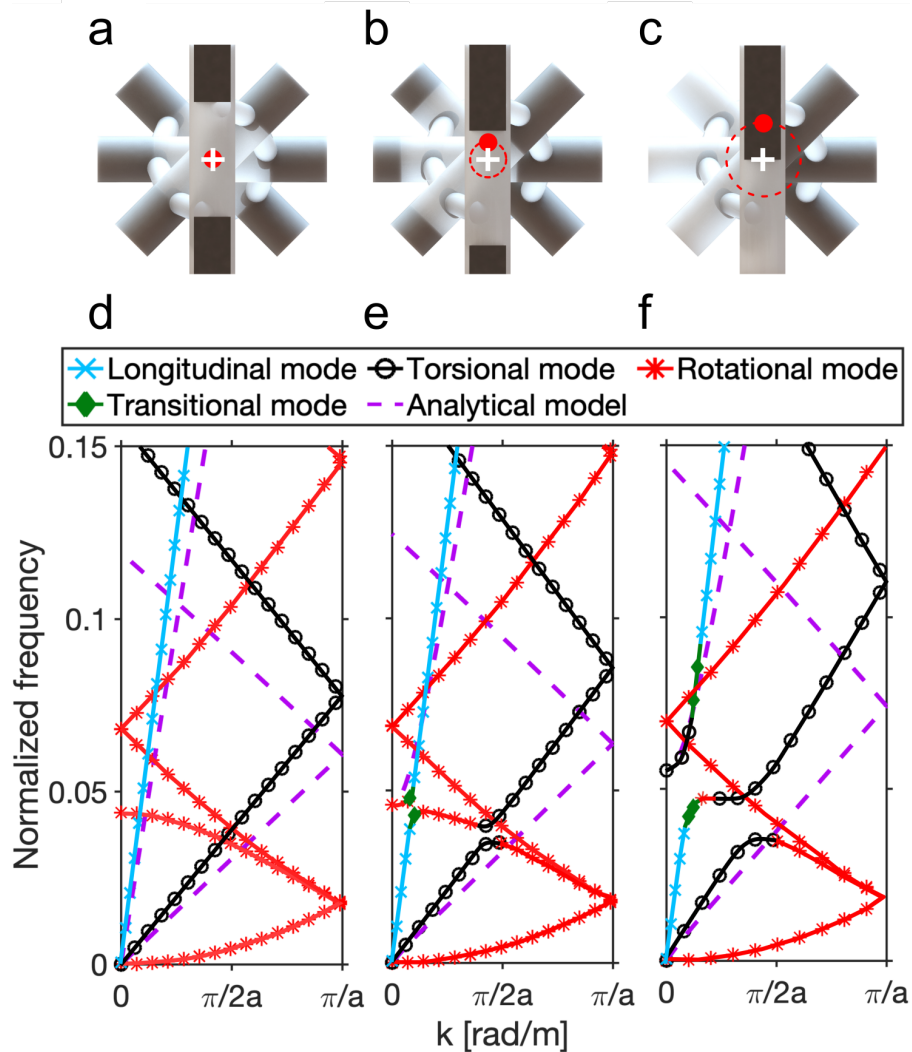


Figure 3.2: Varying centro-assembly of the HMMs and its effects on the dispersion curves. **a, b, and c,** Top views of the HMMs model, which consists of two different materials (light gray: VeroWhite, black: stainless steel) with increasing centro-assembly. The white cross shows the center axis of the HMMs and the red point shows the center of mass of the top beam. **d, e, and f,** Corresponding dispersion curves with normalized frequency as a function of wavenumber. The height of the unit cell a_{HMM} is 8 cm. Blue crosses, black circles, and red asterisks represent the longitudinal mode, the torsional mode, and the rotational mode, respectively. Orange points indicate the transitional modes between different types of normal modes, while the dashed purple lines represent the solution from the ladder-like analytical model.

Dispersion curves with increasing density of the inserts

We studied the dispersion curves of HMMs with inserts, varying their density and distribution, to characterize the hybridization mechanism (Fig. 3.3). Three different types of HMMs are investigated: (i) centrosymmetric HMMs with same material

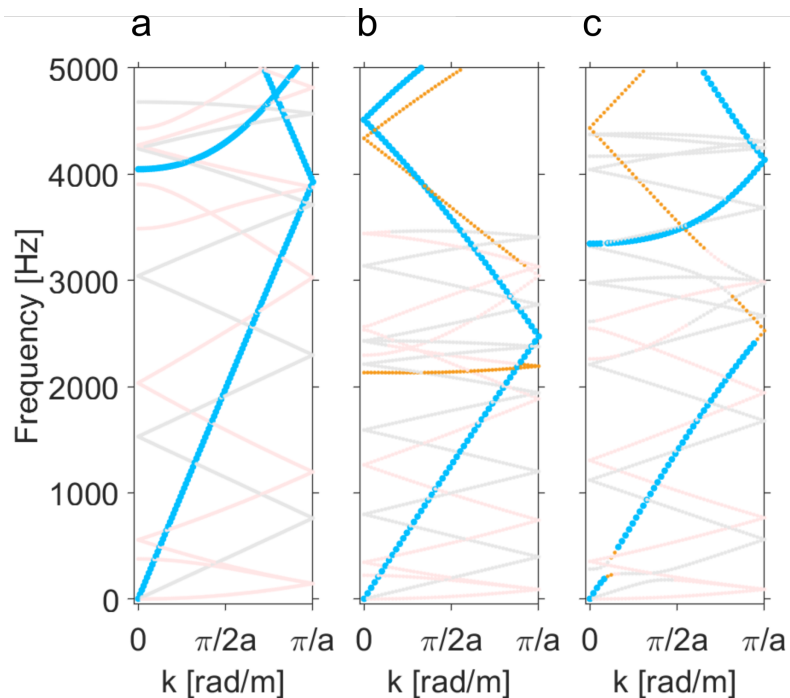


Figure 3.3: Effects of added mass to the mode hybridization of the HMMs. Dispersion curves of the **a**, centrosymmetric HMMs with same material inserts as the base material, **b**, centrosymmetric HMMs with heavier stainless steel inserts, and **c**, fully centro-asymmetric HMMs with heavier stainless steel inserts. The longitudinal modes (blue) and the transitional modes (orange) are highlighted to show the evolution of longitudinal band gaps. The color of the torsional mode (black) and the rotational modes (red) are suppressed in the background.

inserts as the base material, (ii) centrosymmetric HMMs with heavier stainless steel inserts, and (iii) fully centro-asymmetric HMMs with heavier stainless steel inserts. Both centrosymmetric cases show that the longitudinal mode is not hybridized with other modes in the low frequency regime, regardless of the inserts' density (Fig. 3.3a,b). A subwavelength band gap forms only when centro-asymmetry is introduced, at the point where the longitudinal branch first crosses the rotational branch. Such results imply that hybridization is induced by the asymmetric distribution of mass, and not by the increased mass of the inclusions. This mode hybridization leads to the longitudinal subwavelength band gap, which occurs due to the local resonance of the unit cell [14].

Dispersion curves with increasing degree of centro-asymmetry

To study the evolution of the longitudinal band gap with an increasing level of centro-asymmetry, we created finite element models with varying center of mass. The material distribution of stainless steel inserts change from 50-50 distribution

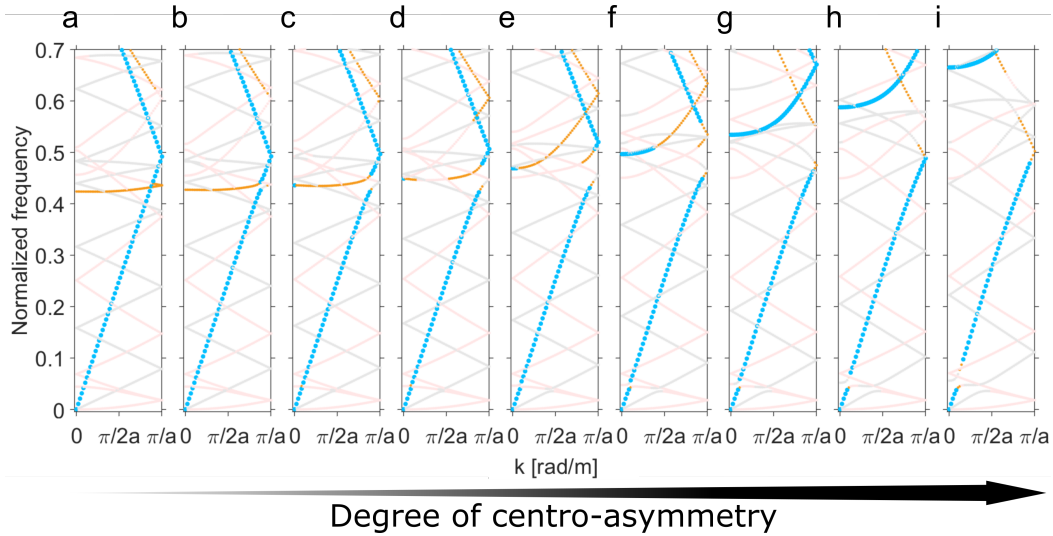


Figure 3.4: Dispersion curves of the HMMs with increasing degree of centro-asymmetry. **a**, 50-50 (centrosymmetric), **b**, 43.25-56.25, **c**, 37.5-62.5, **d**, 31.25-68.75, **e**, 25-75, **f**, 18.75-81.25, **g**, 12.5-87.5, **h**, 6.25-93.75, and **i**, 0-100 (fully centro-asymmetric) material distribution. The longitudinal modes (blue) and the transitional modes (orange) are highlighted to show the evolution of longitudinal band gaps.

(centrosymmetric) to 0-100 distribution (full centro-asymmetric) with intermediate steps. As the center of mass of the horizontal mass beams moves further away from the central axis of the HMMs, the longitudinal band gap shifts upward and widens as shown in Fig. 3.4. This is due to the stronger coupling between the longitudinal mode and the rest of the modes with increased degree of centro-asymmetry. When the HMMs are centro-symmetric (Fig. 3.4a), the longitudinal branch remains linear even though the transitional branch horizontally crosses the longitudinal branch at the frequency around 0.45. As the centro-asymmetry of the HMMs intensifies, the coupling between the transitional mode and the longitudinal mode gets stronger, creating the longitudinal band gap which widens as well (Fig. 3.4b-d). This trend becomes more complicated as the longitudinal mode couples with multiple transitional branches (Fig. 3.4e,f). With even higher degree of centro-asymmetry, an avoided crossing between two separate longitudinal branches forms the larger longitudinal band gap (Fig. 3.4g-i).

Ladder-like analytical model: Effective stiffness and mass

The effective stiffness and mass of both the longitudinal mode and the torsional mode of the helical metamaterials (HMMs) are derived from the long-wave properties of the representative volume element (RVE). The slope of the longitudinal branch and

Effective parameters	Longitudinal mode	Torsional mode
Wave speed, c [m/s], via long-wave approximation	422.18	65.77
Mass, M [kg]	1.65×10^{-3}	-
Moment of inertia, J [$\text{kg} \cdot \text{m}^2$]	-	1.30×10^{-7}
Stiffness, K [N/m]	2.93×10^6	-
Torsional stiffness, C [N·m/rad]	-	5.61

Table 3.1: Effective mechanical parameters of the HMMs. Wave speeds from the dispersion curves are calculated under long wavelength assumption. Corresponding effective stiffness and mass of the RVE of the HMMs for longitudinal modes and torsional modes are listed below.

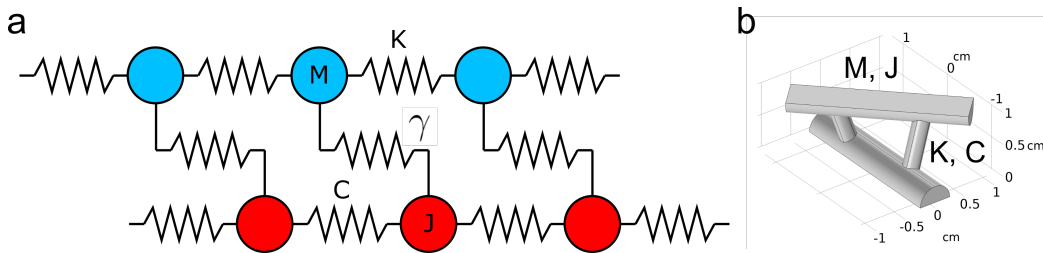


Figure 3.5: The analytical model and corresponding unit cell. **a**, A ladder-like meta chain model with a mass M , stiffness K , moment of inertia J , torsional rigidity C , and coupling stiffness γ . **b**, A representative volume element of the HMMs used for the analytical model.

the torsional branch at the origin of the dispersion curves (Fig. 3.2d) corresponds to the wave speed of each mode under long-wave approximation. The mass, M , and the moment of inertia with respect to the central axis, J , of a single horizontal beam are acquired by integrating the density (with or without a vector from the center axis) over volume. The effective longitudinal stiffness, K , and the torsional stiffness, herein denoted as C , of the unit cell is derived from the relation $c_l = a_{RVE} \sqrt{\frac{K}{M}}$ or $c_t = a_{RVE} \sqrt{\frac{C}{J}}$, where $a_{RVE} = 1$ cm. All the derived properties and corresponding wave speeds for the longitudinal mode and the torsional mode are tabulated in Table S1.

Derivation of the analytical model

We analyzed a parallel mass-spring model [35] (Fig. 3.5a) using the effective parameters of the RVE derived in the previous section. For direct comparison, we divided the torsional stiffness C and the moment of inertia J by a correction factor, $\frac{1}{2}r^2$, to match their units to N/m and kg, respectively. The radius of the vertical pillars, r , is used for the correction factor, based on the relation between the

moment of inertia of the vertical cylinder with its mass, $\frac{J}{m} = \frac{1}{2}r^2$. The characteristic frequencies are

$$\omega_1 = \sqrt{\frac{K}{M}}, \quad \omega_2 = \sqrt{\frac{J}{C}}. \quad (3.1)$$

The equations of motion of a parallel mass-spring model are

$$\begin{aligned} Mu_j + K(2u_j - u_{j-1} - u_{j+1}) + \gamma(u_j - v_j) &= 0, \\ Jv_j + C(2v_j - v_{j-1} - v_{j+1}) + \gamma(v_j - u_j) &= 0. \end{aligned} \quad (3.2)$$

Here, u_j and v_j represent the displacements of the j -th M and J , and are assumed to be in harmonic forms:

$$\begin{aligned} u_j(t) &= \tilde{u}(k(\omega))e^{i(kjd-\omega t)}, \\ v_j(t) &= \tilde{v}(k(\omega))e^{i(kjd-\omega t)}. \end{aligned} \quad (3.3)$$

For more concise derivation, we introduce non-dimensional parameters:

$$\delta_1 = \frac{J}{M}, \quad \delta_2 = \frac{C}{K}, \quad \text{and} \quad \delta_3 = \frac{\gamma}{K}. \quad (3.4)$$

We then insert the values of the effective parameters to the equations of motion, to derive the dispersion curves for the parallel mass-spring model. We can write the dispersion relation in terms of non-dimensional wavenumber $\kappa = kd$ and frequency $\Omega = \omega/\omega_1$:

$$\cos^2 \kappa + \frac{J_1}{2} \cos \kappa + \frac{J_2 - 2}{4} = 0. \quad (3.5)$$

J_1 and J_2 are the invariants of the dispersion relation and can be written as:

$$\begin{aligned} J_1 &= \frac{1}{\delta_2} [(\delta_1 + \delta_2)\Omega^2 - (4\delta_2 + \delta_3 + \delta_2\delta_3)], \\ J_2 &= 2 + \frac{1}{\delta_2} [\delta_1\Omega^4 - (2\delta_1 + 2\delta_2 + \delta_3 + \delta_1\delta_3)\Omega^2 + (4\delta_2 + 2\delta_3 + 2\delta_2\delta_3)] \end{aligned} \quad (3.6)$$

when $\delta_2 \neq 0$. The solutions for the dispersion relation may be written as

$$(\cos \mu)_{1,2} = \frac{1}{4} \left(-J_1 \pm \sqrt{8 + J_1^2 - 4J_2} \right). \quad (3.7)$$

The coupling coefficient γ is obtained so that the y -intercept of the upper branch of the analytical dispersion curves fits the edge of the longitudinal branch (at k

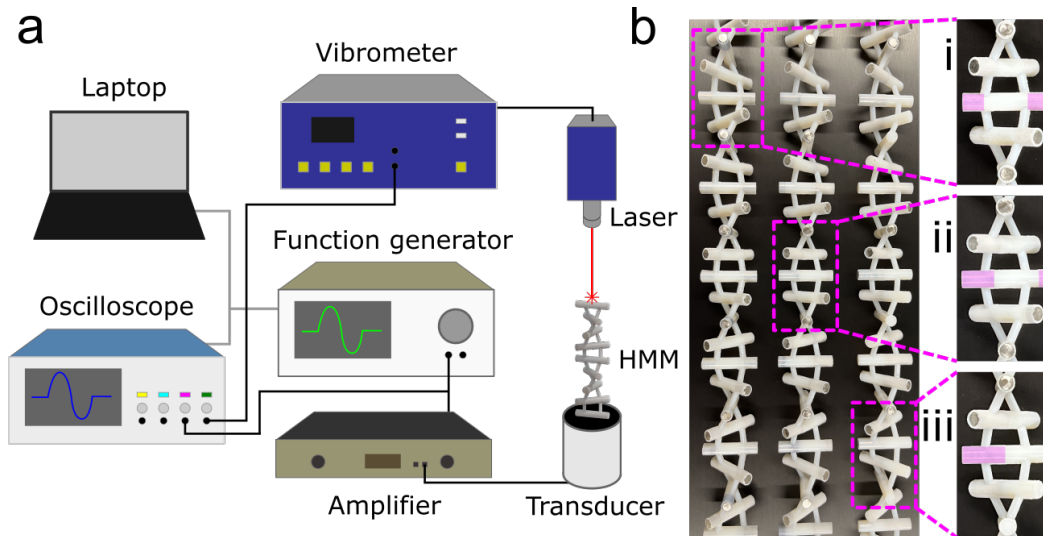


Figure 3.6: Experimental setup and samples. **a**, Schematic diagram and picture of the experimental setup for transmission measurements. **b**, 3D-printed samples with added stainless steel inserts for varying centro-asymmetry. (i) 50-50 material distribution on both ends (centrosymmetric, 6.25 : 6.25 mm length ratio). (ii) 25-75 material distribution (moderately centro-asymmetric, 3.125 : 9.375 mm length ratio). (iii) 0-100 material distribution (fully centro-asymmetric, 0 : 12.5 mm length ratio). Pink boxes indicate where the heavy inserts are positioned.

= 0) in the FE analysis. The dispersion curves of the parallel mass-spring model with varying coupling stiffness γ are plotted together with the numerical dispersion curves, in Fig. 3.2d-f. When $\gamma = 0$, the longitudinal mode and the torsional mode of the analytical model have no interaction, acting as two independent branches. However, as γ increases in value, we observe an avoided crossing from the two branches, which suggests increased coupling [36].

3.5 Experimental validation of the acoustic band gap

Experiment setup

To validate the numerical simulation results, we 3D-printed periodic HMMs with varying levels of centro-asymmetry and characterize them experimentally (Fig. 3.6(b)). We fabricated samples with 6 unit cells (= 48 cm) using a high-resolution PolyJet 3D printing technique (Stratasys Ltd., Connex 500). Due to the high aspect ratio of the samples, we used 2 minimally tensioned strings to hold the samples laterally from adjacent supports (Fig. 3.6a). The base structures are composed of VeroWhite acrylic photoresist, whose constituent properties are $E = 2.5$ GPa, $\nu = 0.33$ [37], and $\rho = 1165$ kg/m³. We measured the stiffness of the VeroWhite acrylic polymer from dynamic characterization, and the density using a regular

scale. For the dynamic characterization, we measured the longitudinal wave speed of cylindrical samples with finite length to derive the Young's modulus from the relation, $c_l = \sqrt{E/\rho}$. We used stainless steel mass inserts with $E = 200$ GPa, $\nu = 0.27$, and $\rho = 7800$ kg/m³. Relatively higher density of the stainless steel rods (4 mm in diameter) compared to the backbone polymer was critical for observing the mass effect more clearly. We used a piezoelectric transducer (Bruel & Kjaer, type 4810) to transmit the signal to the sample. Signals were generated by an arbitrary function generator (Keysight Technologies, 33522B), which was connected to a power amplifier (Bruel & Kjaer, type 2718). Hann-windowed 3-cycle sinusoidal pulses were used to excite the lattices at a central frequency $f = 3$ kHz. We measured the transmitted pulse on the top surface of the sample using a laser Doppler vibrometer (Polytec, CLV-2534), which was sent to an oscilloscope (Tektronix, DPO 3014). The function generator and the oscilloscope were connected to a PC, which enabled the integration of signal generation and data acquisition functionalities into a single MATLAB code.

Transmission analysis

Our FEM simulations predicted that the size of the longitudinal band gaps increases with higher levels of centro-asymmetry (Fig. 3.7a). The deviation at the 0.625 degree comes from a transition of the longitudinal mode's coupling behavior (Fig. 3.4). The transmission plots for the centrosymmetric case, the moderately centro-asymmetric case, and the fully centro-asymmetric case are shown in Fig. 3.7b. The overlaying blue dots represent the longitudinal mode extracted from the dispersion curves, and the blue boxes highlight the longitudinal band gaps identified through numerical simulations. The red boxes indicate where the transmission is less than -15 dB ($\sim 18\%$) from the experimental results. The experimental measurements showed that the band gaps are slightly shifted from the numerical simulations. The band gap of the longitudinal mode widens as the HMMs become more centro-asymmetric, which coincides with the prediction. However, the subwavelength band gaps at lower frequency range (< 500 Hz) were not observed experimentally because the fabricated samples are not sufficiently tall to attenuate longer wavelength inputs. The discrepancy between the numerical predictions and the test results originated from the presence of the torsional mode, which contributes to the longitudinal motion and can transfer the motion even within the longitudinal band gap. Fabrication errors (either during machining or 3D-printing) and the need for support strings [38], due to the long aspect ratio of the structures, may have interfered with the measurements.

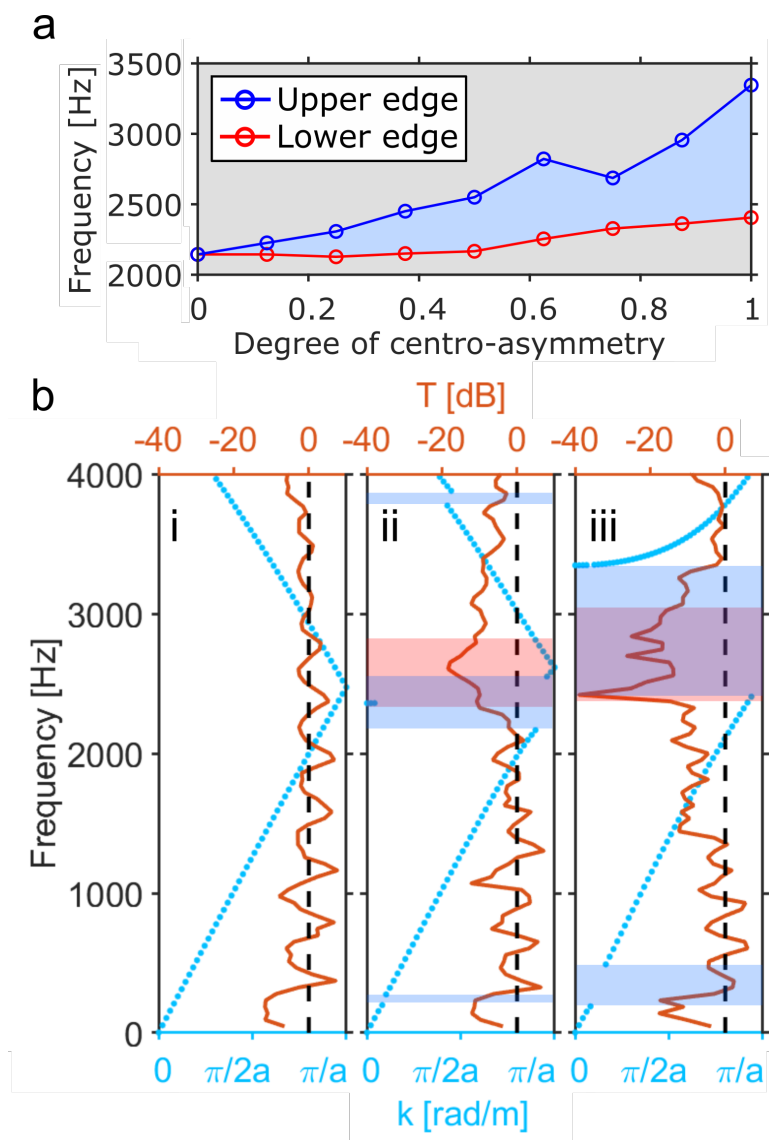


Figure 3.7: Experimental transmission curves coinciding with numerical dispersion curves. **a**, Numerically predicted evolution of the longitudinal band gap (blue region) with increasing degree of centro-asymmetry. **b**, Experimentally measured transmission curves (orange) are plotted with the longitudinal branch (blue dots) that is filtered from the dispersion curve of the (i) centrosymmetric, (ii) moderately centro-asymmetric, and (iii) fully centro-asymmetric HMMs. Plots are highlighted with blue shades indicating the longitudinal band gaps predicted from the numerical simulation and red shades showing the transmission dips (< -15 dB).

3.6 Conclusions

In summary, 1D wave propagation in acoustic metamaterials was analyzed through theoretical modeling, finite element analysis, and experimental validation. This chapter studied the mode hybridization induced by perturbed centrosymmetry in bio-inspired, helical metamaterials. FEM and analytical studies showed that the coupling intensity between independent modes grows with centro-asymmetry. We experimentally demonstrated the hybridization of propagating wave modes and the formation of partial band gaps. In the future, the rich physics of chirality in acoustic metamaterials can be further studied for the realization of devices with acoustic polarization [39], nonreciprocal wave propagation [40], and mechanical logic switches [41].

References

1. Martínez-Sala, R. *et al.* Sound attenuation by sculpture. *Nature* **378**, 241 (1995).
2. Pennec, Y., Vasseur, J. O., Djafari-Rouhani, B., Dobrzyński, L. & Deymier, P. A. Two-dimensional phononic crystals: Examples and applications. *Surface Science Reports* **65**, 229–291 (2010).
3. Hussein, M. I., Leamy, M. J. & Ruzzene, M. Dynamics of Phononic Materials and Structures: Historical Origins, Recent Progress, and Future Outlook. *Applied Mechanics Reviews* **66**. 040802 (2014).
4. Cummer, S. A., Christensen, J. & Alù, A. Controlling sound with acoustic metamaterials. *Nature Reviews Materials* **1** (2016).
5. Laude, V. Principles and properties of phononic crystal waveguides. *APL Materials* **9**, 80701 (2021).
6. Mekis, A. *et al.* High Transmission through Sharp Bends in Photonic Crystal Waveguides. *Phys. Rev. Lett.* **77**, 3787–3790 (1996).
7. Bertoldi, K. & Boyce, M. C. Mechanically triggered transformations of phononic band gaps in periodic elastomeric structures. *Phys. Rev. B* **77**, 052105 (2008).
8. Wang, P., Casadei, F., Shan, S., Weaver, J. C. & Bertoldi, K. Harnessing Buckling to Design Tunable Locally Resonant Acoustic Metamaterials. *Phys. Rev. Lett.* **113**, 014301 (2014).
9. Daraio, C., Nesterenko, V. F., Herbold, E. B. & Jin, S. Tunability of solitary wave properties in one-dimensional strongly nonlinear phononic crystals. *Phys. Rev. E* **73**, 026610 (2006).
10. Li, F., Chong, C., Yang, J., Kevrekidis, P. G. & Daraio, C. Wave transmission in time- and space-variant helicoidal phononic crystals. *Physical Review E - Statistical, Nonlinear, and Soft Matter Physics* **90**, 1–9 (2014).

11. Dong, E. *et al.* Bioinspired metagel with broadband tunable impedance matching. *Science Advances* **6**, eabb3641 (2020).
12. Sigalas, M. M. & Economou, E. N. Elastic and acoustic wave band structure. *Journal of Sound and Vibration* **158**, 377–382 (1992).
13. Sigalas, M. & Economou, E. N. Band Structure of Elastic Waves in Two Dimensional Systems. *Solid State Communications* **86**, 141–143 (1993).
14. Liu, Z. *et al.* Locally Resonant Sonic Materials. *Science* **289**, 1734–1736 (2000).
15. Fang, N. *et al.* Ultrasonic metamaterials with negative modulus. *Nature Materials* **5**, 452–456 (2006).
16. Xiao, S., Ma, G., Li, Y., Yang, Z. & Sheng, P. Active control of membrane-type acoustic metamaterial by electric field. *Applied Physics Letters* **106**, 91904 (2015).
17. Airoldi, L. & Ruzzene, M. Design of tunable acoustic metamaterials through periodic arrays of resonant shunted piezos. *New Journal of Physics* **13**, 113010 (2011).
18. Beli, D., Arruda, J. R. F. & Ruzzene, M. Wave propagation in elastic metamaterial beams and plates with interconnected resonators. *International Journal of Solids and Structures* **139-140**, 105–120 (2018).
19. Miniaci, M., Mazzotti, M., Amendola, A. & Fraternali, F. Effect of prestress on phononic band gaps induced by inertial amplification. *International Journal of Solids and Structures* **216**, 156–166 (2021).
20. Spadoni, A. & Ruzzene, M. Structural and Acoustic Behavior of Chiral Truss-Core Beams. *Journal of Vibration and Acoustics* **128**, 616–626 (2006).
21. Spadoni, A., Ruzzene, M., Gonella, S. & Scarpa, F. Phononic properties of hexagonal chiral lattices. *Wave Motion* **46**, 435–450 (2009).
22. Wu, W. *et al.* Mechanical design and multifunctional applications of chiral mechanical metamaterials: A review. *Materials & Design* **180**, 107950 (2019).
23. Lakes, R. Cellular solid structures with unbounded thermal expansion. *Journal of Materials Science Letters* **15**, 475–477 (1996).
24. Ha, C. S., Hestekin, E., Li, J., Plesha, M. E. & Lakes, R. S. Controllable thermal expansion of large magnitude in chiral negative Poisson's ratio lattices. *physica status solidi (b)* **252**, 1431–1434 (2015).
25. Spadoni, A., Ruzzene, M. & Scarpa, F. Global and local linear buckling behavior of a chiral cellular structure. *physica status solidi (b)* **242**, 695–709 (2005).
26. Bornengo, D., Scarpa, F. & Remillat, C. Evaluation of hexagonal chiral structure for morphing airfoil concept. *Proceedings of the Institution of Mechanical Engineers, Part G: Journal of Aerospace Engineering* **219**, 185–192 (2005).

27. Wu, W. *et al.* Mechanical properties of hierarchical anti-tetrachiral metastructures. *Extreme Mechanics Letters* **16**, 18–32 (2017).
28. Frenzel, T., Kadic, M. & Wegener, M. Three-dimensional mechanical metamaterials with a twist. *Science* **358**, 1072–1074 (2017).
29. Frenzel, T., Köpfler, J., Jung, E., Kadic, M. & Wegener, M. Ultrasound experiments on acoustical activity in chiral mechanical metamaterials. *Nature Communications* **10**, 1–6 (2019).
30. Bergamini, A. *et al.* Tacticity in chiral phononic crystals. *Nature Communications* **10**, 1–8 (2019).
31. Kellersztein, I., Cohen, S. R., Bar-On, B. & Wagner, H. D. The exoskeleton of scorpions' pincers: Structure and micro-mechanical properties. *Acta Biomaterialia* **94**, 565–573 (2019).
32. Greenfeld, I., Kellersztein, I. & Wagner, H. D. Nested helicoids in biological microstructures. *Nature Communications* **11**, 1–12 (2020).
33. Olsen, K. W. & Bohr, J. Transcription and the aspect ratio of DNA. *New Journal of Physics* **15** (2013).
34. A. Srikantha Phani, M. I. H. *Dynamics of lattice materials* (Wiley, 2017).
35. Hajarolasvadi, S. & Elbanna, A. E. Dispersion properties and dynamics of ladder-like meta-chains. *Extreme Mechanics Letters* **43**, 101133 (2021).
36. Mace, B. R. & Manconi, E. Wave motion and dispersion phenomena: Veering, locking and strong coupling effects. *The Journal of the Acoustical Society of America* **131**, 1015–1028 (2012).
37. Cui, S. *et al.* Mechanical Metamaterials Foams with Tunable Negative Poisson's Ratio for Enhanced Energy Absorption and Damage Resistance. *Materials* **11** (2018).
38. Pajunen, K., Celli, P. & Daraio, C. Prestrain-induced bandgap tuning in 3D-printed tensegrity-inspired lattice structures. *Extreme Mechanics Letters* **44**, 101236 (2021).
39. Pine, A. S. Direct Observation of Acoustical Activity in α Quartz. *Phys. Rev. B* **2**, 2049–2054 (1970).
40. Wang, Y. *et al.* Observation of Nonreciprocal Wave Propagation in a Dynamic Phononic Lattice. *Phys. Rev. Lett.* **121**, 194301 (2018).
41. Zheng, B. & Xu, J. Mechanical logic switches based on DNA-inspired acoustic metamaterials with ultrabroad low-frequency band gaps. *Journal of Physics D: Applied Physics* **50**, 465601 (2017).

*Chapter 4***2D WAVE PROPAGATION IN ACOUSTIC METAMATERIALS:
WATER-SATURATED BEAM MICROLATTICES**

This chapter is adapted from:

G. Kim, C.M. Portela, P. Celli, A. Palermo, & C. Daraio. "Poroelastic Microlattices for Underwater Wave Focusing". *Extreme Mechanics Letters* **49**, 101499, (2021).

CONTRIBUTIONS: Participated in the conception of the project, designed and characterized the models via finite element analysis, fabricated the samples, conducted the transmission experiments, analyzed the data, and wrote the manuscript.

4.1 Chapter summary

In the previous chapter, the basics of acoustic metamaterials and wave propagation along a single axis are covered. Building on that knowledge, this chapter explores the effects of expanding the dimension of wave propagation to 2D. We examine the potential for successful manipulation of wave propagation direction through the use of water-saturated microlattices with gradually changing beam diameter.

Microlattices, metamaterials with microscale architectures, can exhibit extreme quasi-static mechanical response and tailorable acoustic properties. When coupled with pressure waves in surrounding fluid, the dynamic behavior of microlattices in the long wavelength limit can be explained in the context of Biot's theory of poroelasticity. In this chapter, we exploit the elastoacoustic wave propagation within 3D-printed polymeric microlattices to incorporate a gradient of refractive index for underwater ultrasonic lensing. Experimentally and numerically derived dispersion curves allow the characterization of acoustic properties of a water-saturated elastic lattice. A modified Luneburg lens index profile adapted for underwater wave focusing is demonstrated via the finite element method and immersion testing, showcasing a computationally efficient poroelasticity-based design approach that enables accelerated design of acoustic wave manipulation devices. Our approach can be applied to the design of acoustic metamaterials for biomedical applications featuring focused ultrasound.

4.2 Introduction

Architected materials consisting of open cell structures with microscale beam elements, i.e., microlattices, can be designed to present desired quasi-static mechanical properties, like high stiffness-to-density ratio [1], ultra-low shear modulus [2], or negative Poisson's ratio [3]. In the dynamic regime, the microscopic features found in these materials enable unique responses in the ultrasonic range (above 20 kHz), including wave tunability [4, 5], wave focusing [6–8], or amplitude mitigation [9]. When immersed in a viscous fluid, their constitutive properties combined with their porosity lead to an interplay between elastic waves traveling in the microlattices and pressure waves in the surrounding fluid medium [10]. Such interplay leads to complex hybridization phenomena that support exotic responses such as the formation of acoustic band gaps [11] or the strong elasto-acoustic coupling that dominates the fluid's transport properties [12, 13]. As such, the selection of specific geometries and structural features allows engineering the propagation of waves in ways that would typically be unachievable with homogeneous or naturally existing materials.

Among various applications of microlattices in the ultrasonic regime, acoustic lensing is of practical importance for its potential use in medical imaging and treatment [14, 15]. In particular, by introducing a gradient of refractive index, one can enable focusing of waves with simple manipulation of geometries or materials and without complicated resonant structures [16–19]. Recently, acoustic gradient-index (GRIN) ultrasonic lenses composed of microlattices have been shown to be capable of focusing plane waves in air [6, 7]. This is achieved by controlling the speed of sound by varying the beam thicknesses across the lattice structure. However, this mechanism should be adapted to account for the presence of the water and the distortion in the refractive index to work in water. Underwater focusing of ultrasonic waves with microlattice geometry has so far been proposed only with air as a filling agent [8]. However, this approach requires a closed lattice design, which suffers from high impedance mismatch at the lens surface and unwanted hydrostatic pressure differences. A more desirable approach for the design of ultrasonic lenses in underwater conditions relies on water-saturated microlattices that account for fluid-structure interaction.

Numerical tools for the design of complex, finite microlattices can be computationally intensive, especially when the lattices are immersed in a fluid. To simplify this process, finite-element representations of fluid-permeated elastic lattices can be replaced by numerical homogenization schemes, which provide an approximation

for the expected response. In the low or moderate frequency range, where wavelengths are much larger than the characteristic lengths of the porous medium, the wave propagation characteristics can be effectively estimated via Biot theory [12, 13]. In this long wavelength regime, fluid-filled cellular media can be considered as a homogenized medium characterized by a few effective physical properties, e.g., porosity, tortuosity, etc. [20–23]

In this chapter, we investigated the characteristics of water-saturated polymeric microlattices in the context of Biot theory and leveraged our findings to realize a fluid-filled GRIN lens. We explored the range of effective refractive index of different types of water-saturated microlattices based on continuum theory. We showed that the traditional Luneburg lens can be effectively configured as a discretized GRIN lens with modified index profile for underwater wave focusing. We verified our design numerically using a computationally efficient poroelastic model combined with a pressure acoustics study. We validated this design experimentally, by 3D printing a microlattice lens consisting of octet trusses with a spatially varying effective refractive index based on the simulated results. The pressure distribution on the output plane was measured and compared to the numerically estimated pressure intensity field. Both results showed good agreement, validating the proposed design approach.

4.3 Effective refractive index of the water-filled microlattices

Biot theory

Biot's theory of poroelasticity has been used for the prediction of the macroscopic behavior of acoustic waves traveling through fluid-saturated porous media at low or moderate frequencies [12, 13]. According to Biot, the speed and modes of the propagating elastoacoustic waves, which are the products of the coupling between elastic waves in solid and pressure waves in fluid, can be accurately identified. It was analytically predicted [12] and experimentally confirmed [24, 25] that the coupled compressional waves split into fast and slow pressure modes in the long wavelength regime. The balance between the boundary layer of Poiseuille flow and the characteristic size of the porous media plays a key role in determining the mode of wave propagation. For a steady, axisymmetric, viscous Poiseuille flow to be established, the boundary layer, also known as the viscous skin depth, $t_{vis} = \sqrt{2\eta/\omega\rho}$, must be greater than the radius of the pores of the solid skeleton, r . Below the 'critical Biot frequency', $\omega_{crit} = 2\eta/\rho r^2$, the Poiseuille flow condition holds and the solid and fluid move in phase by viscous locking, which causes the fast

compression wave to propagate [12]. Slow pressure waves are not supported, since the relative motion of fluid and solid cannot be sustained. If the forcing frequency exceeds ω_{crit} , the Poiseuille flow assumption is no longer valid and the viscous coupling is taken over by inertial coupling, resulting in the occurrence of both fast and slow pressure waves. Slow pressure waves are characterized by the large relative motion between solid and fluid, which makes the waves highly dissipative and difficult to measure experimentally [26]. The inertial coupling is valid below the 'viscous Biot frequency', $\omega_{vis} = \frac{\omega_{crit}}{\zeta^2}$, where ζ is a non-dimensional scaling constant of the order of 0.01 [27]. For the polymeric microlattices considered in this work, the viscous Biot frequency lies above 317 kHz.

Adopting finite element analysis for Biot theory

We implemented finite element models (FEM) (COMSOL[®] Multiphysics) to calculate Biot pressure wave speeds within water-saturated microlattices. The homogenized physical parameters for each structure were computed as in Krödel *et al* [10]. The characteristic equation of oscillating elastic lattices was numerically solved to obtain the speed of compressional and shear waves, c_p and c_s , in the long wavelength limit. The kinetics and kinematics of fluid through the open pores of the microlattices were investigated to calculate the tortuosity, α_∞ , and permeability, κ_o . These parameters were used as inputs for the coupled characteristic equations of water-saturated porous media to derive physical values, such as fast pressure wave speed c_{p1} , slow pressure wave speed c_{p2} , and critical Biot frequencies.

Poroelastic parameters

The poroelastic constants are required to solve the characteristic equations of fluid-saturated homogeneous porous medium under harmonic oscillation [12, 13]. The characteristics equations may be written as

$$\begin{aligned}\tau_{ij} &= [(P + Q - 2\mu)e_{kk} + (Q + R)\epsilon_{kk}]\delta_{ij} + 2\mu e_{ij}, \\ -\phi_p &= Qe_{kk} + R\epsilon_{kk},\end{aligned}\tag{4.1}$$

where τ_{ij} is the total stress of solid and fluid phases, p is the pore fluid pressure in terms of solid and fluid strains, e_{ij} and ϵ_{ij} , respectively, ϕ is the porosity of the porous medium, and μ is the shear modulus of the matrix. These constants can be numerically evaluated from several different models using the finite element method. Including the poroelastic coefficients, P , Q , and R , which are the combinations of

measurable quantities such as the bulk modulus of the solid and fluid materials K_s , K_f , the shear modulus of the solid μ , the drained bulk and shear modulus of solid frame K_m , μ_m , and the porosity ϕ [12], and can be explicitly expressed as

$$\begin{aligned} P &= \frac{\phi K_m + (1 - \phi)K'}{\phi'} + \frac{4}{3}\mu, \\ Q &= \frac{\phi K'}{\phi'}, \\ R &= \frac{\phi^2 K_f}{\phi'}, \end{aligned} \quad (4.2)$$

where

$$\begin{aligned} \phi' &= \phi + \frac{K'}{K_s}, \\ K' &= K_f(\chi - \phi), \end{aligned} \quad (4.3)$$

and $\chi = 1 - K_m/K_s$ is the Biot coefficient. The drained moduli of the solid skeleton are effective measures that can be derived in the long-wavelength limit. The eigenfrequencies of the given solid lattice structure are calculated at very small wavenumber. As a result, the speeds of compressive and transverse waves are calculated as the ratio of the eigenfrequencies to the input wavenumber. Assuming linear elasticity and material isotropy, one can derive the drained moduli, K_m and G_m , of the solid frame as

$$\begin{aligned} K_m &= (1 - \phi)\rho_s \left(v_{Pdry}^2 - \frac{4}{3}v_{Sdry}^2 \right) \\ \mu &= (1 - \phi)\rho_s v_{Sdry}^2. \end{aligned} \quad (4.4)$$

The aforementioned poroelastic coefficients can be expressed as functions of the derived moduli [28].

The other two important constants are tortuosity and permeability. The tortuosity of the lattice is a measure of how geometrically twisted the acoustic path of a solid structure is, that can be represented as

$$\tilde{\alpha} = \alpha_\infty \left(1 - i \sqrt{\frac{\omega_B}{\omega} \left(\frac{\omega_B}{\omega} + \frac{i}{2} \right)} \right), \quad (4.5)$$

which is a function of the critical Biot frequency,

$$\omega_B = \frac{\phi\eta}{k_0\alpha_\infty\rho_f}, \quad (4.6)$$

where α_∞ is the real-valued tortuosity, η is the fluid viscosity, and k_0 is the permeability of the matrix. The relation between the the dynamic tortuosity and the dynamic permeability, \tilde{k} , is

$$\frac{\tilde{\alpha}}{\alpha_\infty} = \frac{k_0 \omega_B}{\tilde{k} i\omega}. \quad (4.7)$$

Different definitions of tortuosity can be found in various literature [29–32]. For our calculation, we followed the one provided by Johnson *et al* [33]. The equations of motion with the assumption of harmonic oscillation can be expressed as

$$\begin{aligned} -\omega^2[(\rho_{11} + \rho_{12})\tilde{\mathbf{u}} + (\rho_{22} + \rho_{12})\tilde{\mathbf{U}}] &= \nabla \cdot \tilde{\boldsymbol{\tau}}, \\ \omega^2[\rho_{12}\tilde{\mathbf{u}} + \rho_{22}\tilde{\mathbf{U}}] &= \phi\nabla\tilde{p} \end{aligned} \quad (4.8)$$

where $\tilde{\mathbf{u}}$ and $\tilde{\mathbf{U}}$ are the amplitude of the displacements of the solid and the fluid, and the complex densities ρ_{11} , ρ_{12} , and ρ_{22} are written as

$$\begin{aligned} \rho_{11} &= (1 - \phi)\rho_s - \rho_{12}, \\ \rho_{22} &= \phi\rho_f - \rho_{12}, \\ \rho_{12} &= (1 - \tilde{\alpha})\phi\rho_f. \end{aligned} \quad (4.9)$$

By assuming an infinitely rigid frame, saturated with an incompressible Newtonian fluid, we solved the eigenfrequency at a small wavenumber to get the slow wave speed, c_{p2} , in the porous media. For non-viscous fluid, one can relate the slow pressure wave speed to the real-valued tortuosity as $\alpha_\infty = (c_w/c_{p2})^2$ where c_w is the speed of sound in water [10]. According to Darcy's law, $v = k\Delta P/\mu\Delta x$, the permeability determines how well a fluid under a pressure gradient can pass through porous media. In numerical simulations, we considered a periodic tessellation of identical unit cells, consisting of non-deformable trusses, subjected to a laminar flow condition. Under a known pressure drop, ΔP , across the finite domain, the average flow velocity, v , can be calculated by integration over the fluid area. The permeability

can then be derived knowing the dynamic viscosity of water, $8.9 \times 10^{-4} Pa \cdot s$, and the size of the unit cell. The Biot pressure wave speeds can be calculated by solving the dispersion relation for the squared compressional wave velocity $c^2 = (\omega/k)^2$

$$d_2 c^4 + d_1 c^2 + d_0 = 0, \quad (4.10)$$

by using standard decomposition techniques where

$$\begin{aligned} d_0 &= PR - Q^2, \\ d_1 &= -(P\rho_{22} - 2Q\rho_{12} + R\rho_{11}), \\ d_2 &= \rho_{11}\rho_{22} - \rho_{12}^2. \end{aligned} \quad (4.11)$$

Since

$$\begin{aligned} c_j^2 &= \frac{-d_1 \pm \sqrt{d_1^2 - 4d_0d_2}}{2d_2} \\ &= \left(\frac{\omega}{k_j} \right)^2, \end{aligned} \quad (4.12)$$

the phase velocities are computed from the solutions of the quadratic equation in complex wavenumbers k_j^2 as

$$c_{P_{1,2}} = \frac{\omega}{\Re(k_{1,2})}. \quad (4.13)$$

Fast and slow Biot pressure waves

The fast and slow pressure waves speeds, c_{p1} and c_{p2} , as well as the corresponding acoustic refractive indices n , are shown as a function of porosity for four different truss structures, e.g., octet, isotropic, diamond, and Kelvin trusses (Fig. 4.1). The range of porosity is chosen so that the lattice structures are in a manufacturable regime and their topology remains open-celled. The c_{p1} curves for the four different geometries almost overlap (Fig. 4.1a), whereas the c_{p2} curves show variations. The speed of the solid-borne waves, c_{p1} , generally depends on the effective elasticity of the porous media, which is a function of geometry [34]. However, at the manufacturable relative densities for these microlattices, the density-stiffness relation is

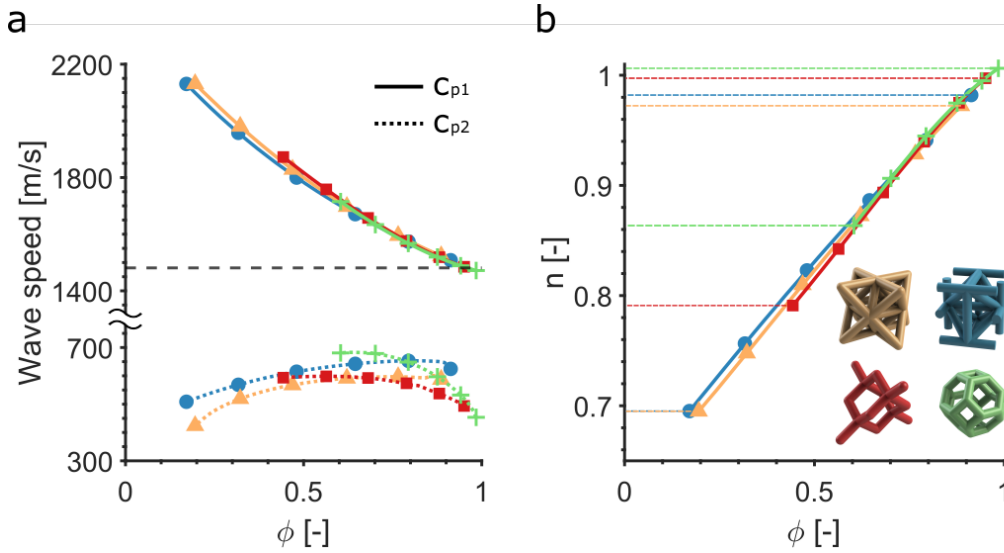


Figure 4.1: Wave speeds and refractive indices of water-saturated microlattices.

a, Fast pressure wave speed (c_{p1} , solid lines) and slow pressure wave speed (c_{p2} , dotted lines), and **b**, effective refractive index ($n = c_w/c_{p1}$) of water-saturated polymeric lattices with respect to porosity for different types of lattices: octet (yellow), isotropic (blue), diamond (red), and Kelvin (green) trusses. The speed of sound in water, $c_w = 1481$ m/s, is shown as reference in **a** (dashed black horizontal line). The excitation frequency of the acoustic wave is fixed at 300 kHz, which is below the estimated viscous Biot frequencies.

very similar across architectures [35, 36]. Especially when porosity is higher, c_{p1} is less sensitive to the moduli of the solid and the effect of the bulk modulus of the fluid becomes dominant [28]. Therefore, it is not surprising to observe that c_{p1} does not vary with the lattice geometry, especially at higher porosity range. On the other hand, the speed of fluid-borne waves, c_{p2} , depends on the fluid path and on the viscous coupling. Both quantities depend on the tortuosity and the permeability, which are the products of the lattice geometry [28].

The effective acoustic refractive index of a microlattice unit cell is defined as $n = c_w/c_{p1}$, where c_w is the speed of sound in water and c_{p1} is the speed of fast pressure wave through the porous media. A water-saturated polymeric foam only allows fast compressional waves to propagate due to attenuation of the slow pressure waves [10, 37]. In other words, the effective refractive index for different types of polymeric lattices is only a function of c_{p1} . As such, we expect that variations of refractive index among the different geometries can only be ascribed to their different porosities (Fig. 4.1b). Interestingly, the two bending-dominated lattices reach higher refractive index values, due to their smaller truss connectivity. With

higher connectivity, however, the stretch-dominated lattices can achieve larger ranges of refractive index variation. We can exploit these properties as design features for our acoustic lenses. We chose the octet truss as the fundamental building block for its large refractive index variability (Fig. 4.1b) and the ease of fabrication.

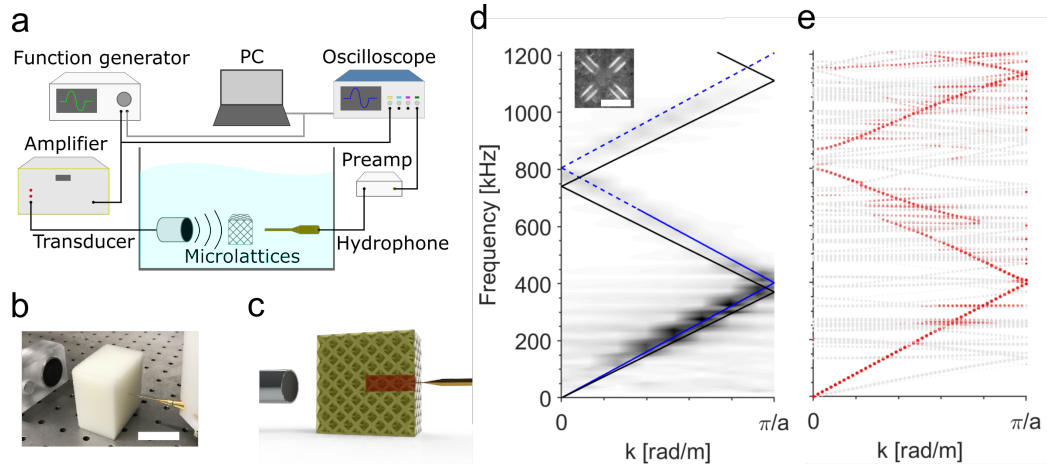


Figure 4.2: Experimental setup and analytical, numerical, and experimental dispersion curves. **a**, Experimental setup with **b**, the picture (scale bar: 5 cm) and **c**, the 3D model of the measurement system. The model represents the cut plane (yellow) and the drill hole (red) of the test sample. **d**, Experimentally reconstructed dispersion curve (grey-scale colormap, normalized between 0 and 1) with the prediction from Biot theory (solid blue line) extrapolated above the viscous critical frequency (dashed blue line). The linear dispersion curve of water wave (black line) is plotted as a reference. (Inset) The microscope image of the unit cell (scale bar: 1 mm). **e**, Numerically calculated dispersion relation with longitudinally polarized in-phase modes highlighted in red, others in gray.

4.4 Dispersion relation of the water-filled microlattices

Experimental reconstruction

To determine the acoustic characteristics of our samples, we experimentally reconstructed the dispersion relation of water-saturated microlattices and compared the results to a numerically calculated dispersion relation. We fabricated microlattices composed of octet structures using a high-resolution digital light processing (DLP) 3D printing technique (Autodesk[®] Ember) using PR48[™] acrylic photoresist, whose constituent properties are taken to be $E = 3.3$ GPa, $\nu = 0.39$, and $\rho = 1190$ kg/m³ [10]. The size of the unit cell is 2 mm along each side with the radius of the truss $r = 0.16$ mm. To ensure that the wave characteristics are well developed, we allowed more than 5 wavelengths along the travel distance, as a rule of thumb. To accommodate 10 wavelengths at 300 kHz, the lowest center frequency of interest, we

printed 25 cells along the wave propagation direction. To measure the acoustic wave propagation in the water saturated lattices, we immersed our structure in water and remove the air trapped in the sample with a vacuum pump. All the measurements were done in a $1.2\text{ m} \times 0.75\text{ m} \times 0.75\text{ m}$ water tank surrounded by 2 cm-thick acrylic walls (Precision Acoustics), see Fig. 4.2a. The tank was filled with deionized water at room temperature, with negligible variance between measurements. The lattice was positioned between a broadband ultrasonic transducer (V391-SU, 500 kHz) and a needle hydrophone (Precision Acoustics, 0.2 mm) (Fig. 4.2b). We drilled a hole (2 mm wide and 2 cm deep) in the center of the lattice (Fig. 4.2c), to accommodate the insertion of a hydrophone to measure pressure gradients within the sample. Signals were generated by an arbitrary function generator (Keysight Technologies, 33522B) connected to a radio-frequency amplifier (Amplifier Research, 75A220). Hann-windowed 1-cycle sinusoidal pulses were used to excite the lattices, at a central frequency $f = 300\text{ kHz}$. Three single-axis motorized stages (Velmex, BiSlide) were installed above the water tank to control the position of the hydrophone. We measured the transmitted pulse along the drilled hole with constant step increment (0.3 mm), allowing the characterization of the lattices' dispersive properties. A pre-amplifier (Precision Acoustics) connected to the hydrophone relayed the measured pressure signal to an oscilloscope (Tektronix, DPO 3014). The function generator, the oscilloscope, and the motorized stages were connected to a PC, which enabled the integration of signal generation, data acquisition, and positioning functionalities into a single MATLAB code. To reconstruct the dispersion characteristics of our samples, the measured pressure signal was 2D Fourier-transformed into the wavenumber-frequency domain (Fig. 4.2d).

Effects of the defects on the experimental measurement data

For the experimental measurements, we have drilled a hole into a microlattice sample, which might have affected the overall acoustic properties of the water-saturated microlattices. Moreover, we applied vacuum to a microlattice sample immersed in water to fully infiltrate the pores of the octet microlattices. There is a possibility that this process may have caused damage to the beams of the unit cells. It is challenging to investigate defects or their effects, particularly when the sample contains hundreds of unit cells. Despite this, we can safely assume that the defects did not significantly impact the overall acoustic properties of the water-saturated microlattices as (1) the size of the probe hole was small, (2) the wavelength of the input pressure waves was larger than the feature size of the unit cell, and (3) both

the Biot model and the FE model were compared to the experimental results for validation.

The size of the sample was $7 \text{ cm} \times 7 \text{ cm} \times 5 \text{ cm}$ and the probe hole was made on the larger face of the sample. The hole diameter ($\phi_{hole} = 2 \text{ mm}$) was chosen so that the needle hydrophone ($\phi_{hydrophone} = 0.2 \text{ mm}$) could probe inside the sample without making contact and affecting the measurements, while effectively removing a single line of unit cells at most along the depth direction. Since a line defect in acoustic metamaterials only affects amplitude of the signal without disturbing the overall wave properties, it is safe to assume that the hole has minimal influence to the measurement results [38]. The wavelength of input pressure waves at 300 kHz is 5 mm when they travel through water. Both the unit cell size ($a = 2 \text{ mm}$) and the diameter of the constituent beams ($d = 0.32 \text{ mm}$) are considerably smaller than the wavelength, so the possible influence of micro-cracks created from the vacuum process can be neglected. The experimentally reconstructed dispersion curve was thoroughly investigated by comparing results with other dispersion curves from the poroelastic model and the analysis 4.2d,e. Based on these evaluations, we can assure that defects do not significantly influence the acoustic properties of water-saturated microlattices.

2D FFT for the reconstruction of dispersion curve

The purpose of the Hann filter was to reduce any sudden change in amplitude, which may have led to overshooting of the output pressure. Outside the Hann window, the signal was zero-padded to minimize the interference with the previous signals. We stored the transmitted pressure signal measured at each point along the hole in the lattice as a function of time with sampling frequency $f_s = 1.25 \text{ GHz}$. To secure enough data points within a single wavelength ($\lambda \simeq 2 \text{ mm}$ at $f = 800 \text{ kHz}$) and to prevent aliasing, we set the step size between points as 0.3 mm. The measured data was collected in a 2D matrix of output pressure signal with respect to space and time. For the reconstruction of the dispersion curve, we 2D-Fourier-transformed the pressure matrix in space-time domain into the reciprocal wavenumber-frequency domain. We plotted the transformed data with $k \in [0, \pi/a]$ to show the dispersion relation in the first Brillouin zone.

Output normalization

We normalized the transmitted pressure intensity after the Fourier transformation, to compensate for the intensity variation among the frequency components of the

input signal. The reference pressure signal measured without the test sample shows pseudo-Gaussian distribution of amplitude, as shown in Fig. 4.3a. We used the reference pressure amplitude to normalize the transmitted pressure intensity measured with the sample (Fig. 4.3b).

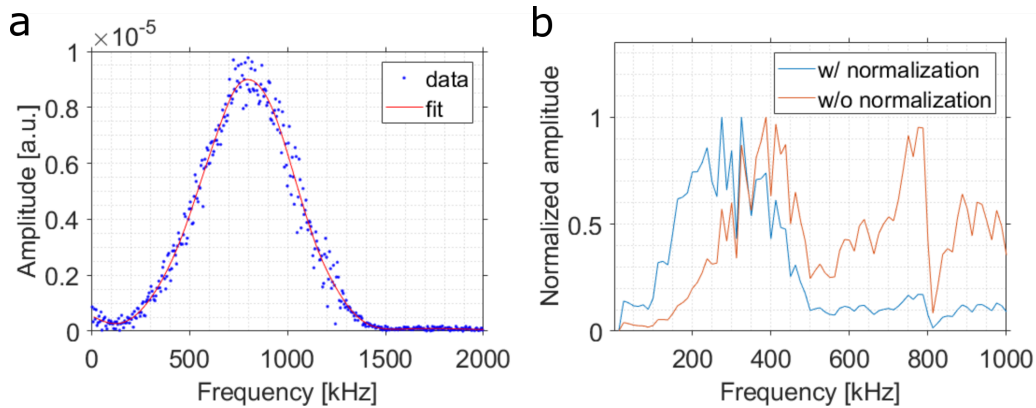


Figure 4.3: (a) Reference pressure amplitude with frequency centered at 800 kHz. (b) Pressure output before (red) and after (blue) normalization.

Numerical computation

We also investigated the elastoacoustic characteristics via numerical simulations. Finite element models of the water-filled microlattices were implemented to derive their dispersion relation. We studied the coupled acoustic and stress wave propagation in the [001]-direction under pressure equilibrium and Bloch-Floquet periodic boundary conditions. The acoustic behavior of octet microlattices under an incident plane wave is shown in Fig. 4.2e. The strong coupling between structural and acoustic modes results in various hybridized branches. The four main modes are two compressional waves, corresponding to one solid-borne and one water-borne pressure waves, and two degenerate shear modes of the elastic frame. We focus on the occurrence of the solid-borne longitudinal modes of the water-saturated polymeric lattices (red dots in Fig. 4.2e), as this mode dominates energy propagation of the ultrasonic waves [37].

Dispersion relation

We studied the dispersion relation of the water-saturated polymeric lattices in finite element simulations, by using the eigenfrequency solver in COMSOL[®] Multiphysics. We applied Bloch-Floquet periodic boundary conditions on the faces of the unit cell under plane wave input. To properly represent the curvature of the trusses and joints, we used a tetrahedral mesh with the radius of the truss and 1/8 of the

radius as the maximum and the minimum mesh size, respectively (Fig. 4.4a). We solved the resulting eigenvalue problems for varying wavenumbers selected within the first irreducible Brillouin zone, $[0, \frac{\pi}{a}]$, with a being the unit cell size.

To find the optimal mesh size, we evaluated the computation accuracy and time as a function of the number of degrees of freedom (DOF) (Fig 4.4c). We quantified the accuracy of the mesh by the average error of the computational results, compared to the predicted pressure wave speeds from Biot theory at very small wavenumber $k = 0.001 \times \frac{\pi}{a}$. We plotted the total computation time to obtain four eigenfrequencies along with the error curve, to show the efficiency of the mesh. The error decreases as the mesh gets more refined, which is counteracted by exponentially increasing computation costs. We concluded that 2.4×10^5 number of DOFs ensures accurate enough results with reasonable efficiency.

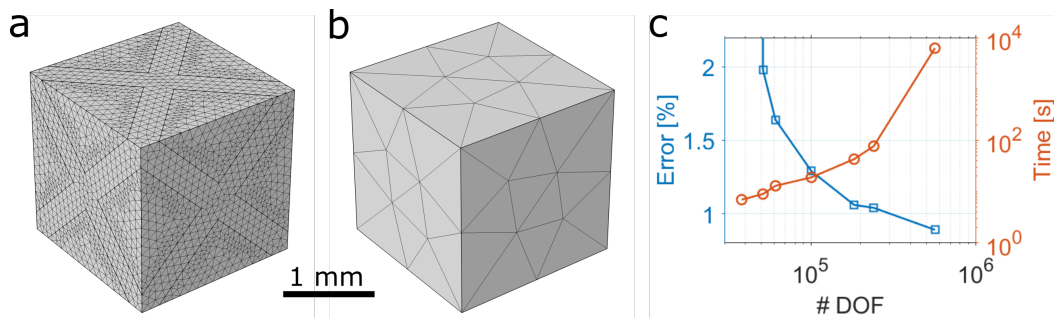


Figure 4.4: Convergence study. Discretized meshes of the numerical model for the unit cell of **a**, octet lattice with surrounding water and **b**, equivalent poroelastic medium. **c**, The error (blue) and computation time (orange) of the eigenfrequency solver of the water-saturated octet lattice as a function of number of DOFs. The error at $\text{DOF} = 38102$ is 2245.81 %, which is not shown in the plot.

To classify wave modes, we used several physical parameters, such as the volume-averaged displacement vectors of the solid frame, and the volume-averaged velocities of the solid and fluid field. We defined two classification criteria: (i) the polarization of the normal modes of the solid frame and (ii) the phase difference between the solid and fluid domain, according to the Biot theory. The polarization factor, p_1 , ranges from 0 to 1, with 1 being purely longitudinal and 0 being purely transverse. The phase-matching factor, p_2 , indicates the degree of mismatch between the oscillating directions of the solid and the fluid domain, and ranges from complete in-phase ($p_2 = +1$) to out-of-phase ($p_2 = -1$) modes. Using these classifications, we plotted the dispersion curve in Fig. 4.2e with longitudinally polarized in-phase modes highlighted as red, and others in gray.

Analysis of the dispersion curves acquired using different approaches

The experimental dispersion curve shows a linear, nondispersive response in the frequency range between the critical Biot frequency (61.2 Hz) and the viscous Biot frequency (611.8 kHz), marked by several regions of reduced transmission (Fig. 4.2d). These results agree well with finite-element simulations (Fig. 4.2e), which also show a dispersionless branch (red dotted line in Fig. 4.2e) crossed by localized modes with near zero group velocity. The slope of these branches corresponds to the sound speeds, which are 1641 m/s in the experiments and 1603 m/s in the simulations. A solid-dashed line (blue) overlaid on the experimental dispersion curve corresponds to the fast pressure wave solution of the Biot theory model. The analytical model shows dispersionless mode within an inertia-dominated regime at a constant wave speed of 1611 m/s. We extrapolated the prediction to the frequency region above the viscous critical frequency for a reference. We also plotted the dispersionless curve of water waves (black) as a reference.

The presence of localized modes, evident in the numerical dispersion curve (e.g., around 300 kHz in Fig. 4.2e), suggests an increased attenuation due to resonances within the microlattices [39]. The localized modes' frequency in the numerical simulations correspond to the region of reduced transmission in the experiments (Fig. 4.2d). However, the regions of reduced transmission are narrow band and do not significantly affect the overall signal transmission. This is evident in Fig. 4.3, which shows the transmission amplitude as a function of frequency.

At higher frequencies, around 600 kHz, the numerical dispersion curve shows veering of the two fast pressure modes, mixed with multiple localized modes, suggesting the presence of multiple hybridized modes. This manifests as a significant drop in the transmitted amplitude through the lattice at similar frequencies (Fig. 4.2d). A Bragg band gap is observed in both of the dispersion curves around 800 kHz, which leads to the bending of the branches near the forbidden band. At higher frequencies (above 850 kHz), the dispersion curve shows decreasing group velocity. The dynamic characteristics of the dispersion curve reconstructed from experiments agree well with the numerical simulations. We exploit these propagation properties to design an acoustic lens.

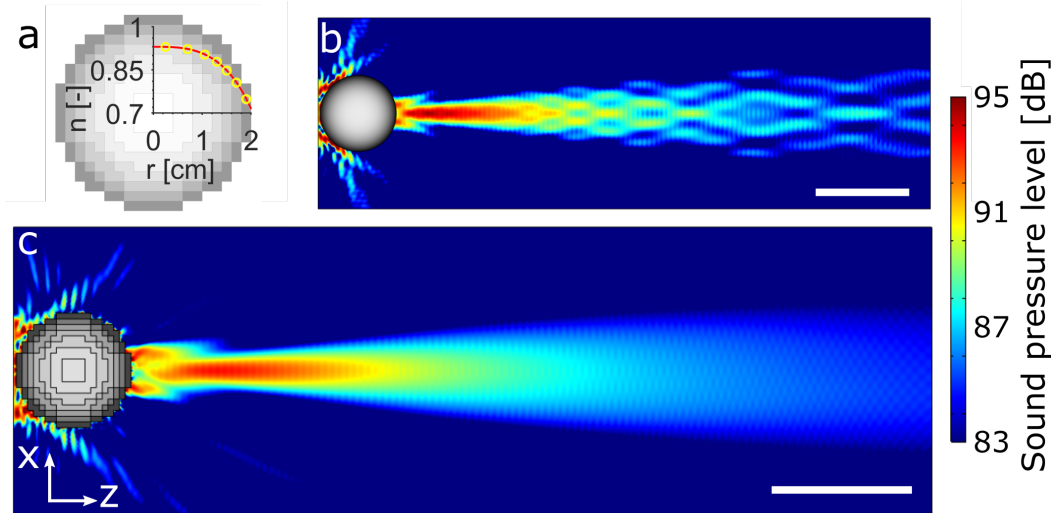


Figure 4.5: Pressure acoustics simulation for Luneburg lens. **a**, Discretized Luneburg lens with continuous (red curve) and discrete (yellow circles) refractive index profiles. Pressure acoustics simulations of Luneburg lens with **b**, the continuous profile, and with **c**, the discrete layers, with poroelastic properties corresponding to the effective refractive indices selected (scale bar: 5 cm).

4.5 Gradient-index Luneburg lens design

Determining the refractive index of the Luneburg lens

Based on the dispersion characterization of our water-filled polymeric microlattices, we designed a 2D Luneburg lens with a spatially discretized refractive index profile (Fig. 4.5a). In a conventional, continuous GRIN lens, the focal point resides on the lens' surface [40]. However, for most applications, it is useful to place the location of the focal point in a region at a finite distance from the lens surface. To spatially vary the focal distance in water, it is necessary to design an appropriate distribution of the refractive index profile within the lens [41, 42]. Moving the focal point outside the lens induces undesirable aberration in the focal region [43]. We minimized these aberrations by further modifying the refractive index distribution within our lens (Fig. 4.6). The original refractive index profile for the Luneburg lens is $n = \sqrt{2 - r_L^2/R_L^2}$, where r_L is the distance from the center of the lens, and R_L is the radius of the spherical lens [40]. However, for fluid-saturated polymeric lattices underwater, the refractive index must be smaller than 1 since c_{p1} is always greater than c_w (Fig. 4.2d). We introduced a modified Luneburg lens profile, $n = \sqrt{\frac{1+f_L^2-(r_L/R_L)^{a_L}}{b_L f_L}}$, with three nondimensional parameters, $a_L = 3.08$, $b_L = 1.40$, and $f_L = 1.2$ with $R_L = 2$ cm. The refractive index distribution of the modified Luneburg lens is shown as a continuous line in Fig. 4.5a. The refractive index

gradually varies from $n = 0.93$ at the core of the lens to 0.71 on the outer surface. This profile ensures that the speed of the acoustic waves is larger on the perimeter of the lens than at its center.

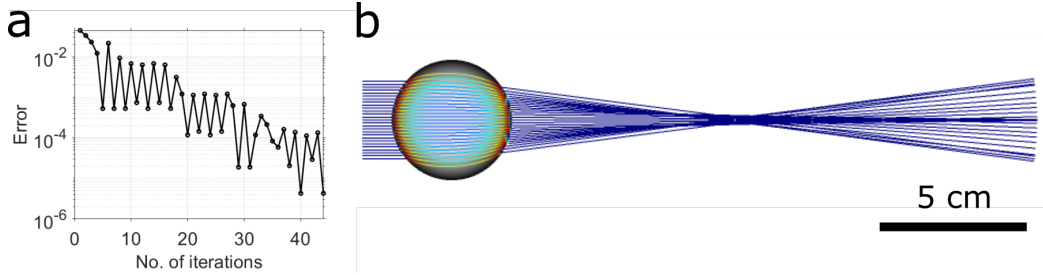


Figure 4.6: Optimization of Luneburg lens profile for underwater wave focusing. **a**, Spherical aberration minimization using adaptive gradient descent optimization. **b**, Ray trajectory simulation of underwater Luneburg lens with optimized refractive index profile.

Ray acoustics design

We modified the conventional Luneburg lens index distribution [40], $n = \sqrt{2 - (r_L/R_L)^2}$, by introducing three nondimensional parameters. These parameters enable the lens to have focal point outside the lens, instead of on the lens' surface, in underwater environment. We found the best values for the nondimensional parameters, a_L , b_L , and f_L in the modified refractive index profile, $n = \sqrt{\frac{1+f_L^2-(r_L/R_L)^{a_L}}{b_L f_L}}$ [43] via adaptive gradient descent method. The order of the $\frac{r_L}{R_L}$, a_L , determines the convergence of rays and must be greater than or equal to 2. A scaling parameter, b_L , adjusts the refractive indices below 1, which is the maximum refractive index achieved by water-saturated polymeric microlattices. f_L determines the approximate focal length of the lens and is fixed at 1.2 so that the focal point lies 8 cm behind the lens (double the width of the lens). We applied the gradient descent optimization to minimize the error (Fig. 4.6a), defined as the radius of the circle of confusion, and to minimize spherical aberration of the lens. As the results of the iterations under the constraints stated above, these parameters converge to $a_L = 3.0815$ and $b_L = 1.4045$, and the final ray trajectories are shown in Fig. 4.6b.

Verification of the Luneburg lens design

To verify our design scheme, we implemented COMSOL[®] simulations to compare the pressure acoustic profile of a continuous GRIN lens (Fig. 3b) with our discretized lens (Fig. 4.5c). First, we investigated a continuous Luneburg lens with modified refractive index distribution under incident plane waves at 300 kHz. We modeled

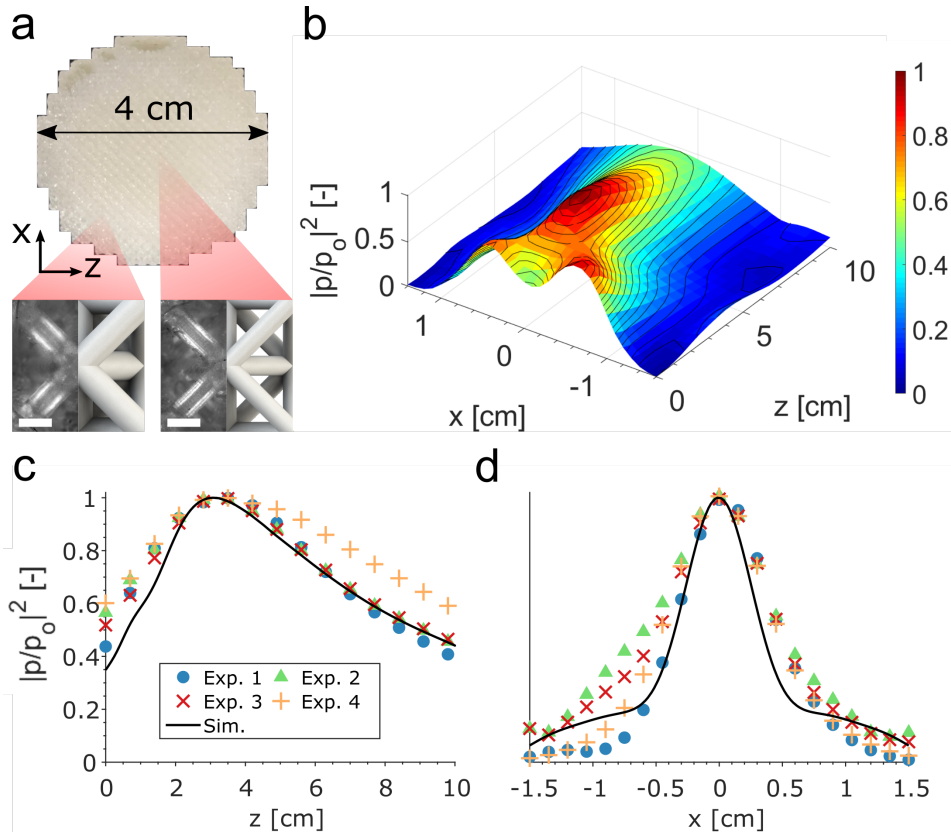


Figure 4.7: Experimental results of the 3D-printed GRIN Luneburg lens. **a**, Top-view photograph of the 3D printed Luneburg lens. The insets show optical microscopy images and corresponding models of unit cells from two different regions (scale bar: 0.5 mm). **b**, Normalized pressure intensity in the output plane, **c**, along the centerline, and **d**, across the focal point. Experimental data were measured from four different scan planes along the lens.

an acoustic domain with $\rho_w = 1000 \text{ kg/m}^3$ and $c_w = 1481 \text{ m/s}$ for underwater environment. Perfectly matched layers (PMLs) surround the external boundary of the acoustic domain to minimize unwanted reflections. We plotted the sound pressure level of the region of interest with ambient pressure as a reference. The continuous GRIN lens focuses plane waves in a localized region behind the lens (3.15 cm away from the surface).

To validate our discrete lens design, we performed the same finite-element simulation on a lens assembled with different layers of poroelastic media with finite thickness (Fig. 4.5c). A circular Luneburg lens, 4 cm in diameter, consists of total 7 layers of unit cells of $2 \text{ mm} \times 2 \text{ mm}$ size. We determined the refractive indices of the discretized layers by taking the mean value of the index along the radial direction. Within each layer, we derived the beam thickness of each unit cell from

the poroelastic parameters corresponding to the desired refractive index value (Fig. 4.5a).

Both simulations result in similar pressure distributions along the output plane, indicating that the poroelastic model captures effectively the acoustic characteristics of the GRIN lens. The homogenized models of the water-saturated lattices are significantly more computationally efficient than the fully discretized simulation with several hundreds octet lattice unit cells and solid-water interfaces (Fig. 4.4). The pressure distribution in both simulations highlight the presence of scattering and side lobes, resulting in signal transmission loss at the focus.

Pressure acoustics study using poroelastic waves module

Using the modified refractive index profile, we numerically predicted the pressure distribution under plane acoustic wave input. We studied both pressure acoustics model and poroelastic model to compare them, and to validate the use of poroelastic assumptions for the design of the GRIN lens (Fig. 4.5b,c). For both simulations, plane waves at 300 kHz travel from a line source on the left of the lens, forming output plane on the right. We adopted perfectly matched layers (PMLs) to create non-reflecting boundaries surrounding the acoustic field. For the mesh of the representative unit element, the maximum size and the minimum size are 1/5 of the wavelength and 1/10 of the unit cell size, respectively, as shown in Fig. 4.4b. We determined the mesh size so that there are effectively ~ 9 mesh elements within a single wavelength [44]. As a result, the poroelastic model has much coarser mesh than the water-coupled lattice model. For a single unit cell, the number of DOFs reduces from 240k for the water-saturated octet lattice to 1k for the homogenized model, which makes the poroelastic simulation computationally cheaper. The main difference between the ray trajectory simulation and the pressure acoustics study is a discrepancy in the focal distance. This was to be expected, since geometrical ray acoustics is less accurate in the low frequency limit [45]. Nevertheless, the ray trajectory study provides a good approximation for the initial design of the lens.

4.6 Underwater experiments of the Luneburg lens

Experimental setup

We 3D-printed a microlattice-based GRIN lens to validate the lens design experimentally (Fig. 4.7a). The size of each unit cell is 2 mm and the radius of the trusses ranges from 0.15 mm to 0.30 mm, with the thicker beams placed on the outer layers. We excited the lens with Hann-enveloped bursts, consisting of 5 sinusoidal cycles,

to achieve narrow bandwidth at the center frequency (300 kHz). To evaluate the focusing, we mapped the pressure field behind the lens with a 4 mm hydrophone (Fig. 4.2a). We recorded voltage outputs and normalize them by their peak amplitude. The typical scattered intensity field of the transmitted acoustic waves (Fig. 4.7b) shows the formation of a focal peak ca. 3 cm away from the lens' surface. Side lobes are evident just outside the lens, as predicted in simulations and reported in earlier studies [46].

Pressure scan

The scan plane is parallel to the top plane of the lens (Fig. 4.7a). We scan the pressure field in a rectangular area of dimensions 30 mm \times 100 mm with step sizes 1 mm and 5 mm, respectively, splitting the area into 651 data points. As the hydrophone moves to each location, we enforce a 2-seconds pause to avoid undesired vibrations to the needle hydrophone.

Measurement results

The results from 4 separate experiments (discrete points) are compared to the numerical predictions (solid black lines), along the directions parallel and perpendicular to the focal point (Fig. 4.7c,d). The results agree well, with only minor discrepancies among the experimental data arising from the finite height of the 3D printed lens. The focal length, measured from the back of the lens, and the full width at half maximum (FWHM) are evaluated from the results. The focal length of the poroelastic Luneburg lens is observed to be 3 cm, which is in good agreement with the numerical prediction (3.15 cm). We obtain $3.46 (\pm 0.3)\lambda$ for the FWHM of the 3D printed lens whereas the prediction is 2.8λ , due to higher amplitudes around the outer edge. The overestimation is caused by the diffraction of the incident wave traveling around the Luneburg lens. In the experiments, the ultrasound emitter had a finite width unlike the numerical simulations, which assume an incident planar wave front. In addition, the 3D printed lens had a finite height, which increased the diffraction from the top plane. We also ascribe this discrepancy to the limited prediction of the transmission property due to the use of a simplified poroelastic model and due to fabrication errors.

4.7 Conclusions

In summary, we investigated the impact of expanding the dimension of wave propagation to 2D, especially in water environment. The aim is to explore the possibility

of successfully controlling the direction of wave propagation by using microlattices with gradually varying beam diameters that are saturated with water. This chapter takes advantage of the theory of poroelasticity for the design of underwater Luneburg lenses featuring heterogeneous arrangement of polymeric microlattices filled with water. We have demonstrated that using poroelastic theory allows for the computationally cheaper and faster design of acoustic wave manipulation devices. This approach could be used for biomedical applications that require focused ultrasound including ultrasonography [47] and sonochemistry [48, 49].

*Chapter 5***3D WAVE PROPAGATION IN ACOUSTIC METAMATERIALS:
PLATE MICROLATTICES IN WATER ENVIRONMENT**

This chapter is adopted from:

G. Kim, C. Rabut, B. Ling, M.G. Shapiro, & C. Daraio. "Conformal Acoustic Window for the Skull Based on Microscale Metamaterials". *In preparation*.

CONTRIBUTIONS: Participated in the conception of the project, designed and characterized the models via finite element analysis, fabricated the samples, conducted the mechanical characterization both under quasi-static and dynamic loading, participated in the animal experiments, analyzed the data, and wrote the manuscript.

5.1 Chapter Summary

This chapter builds on the knowledge gained in previous chapters and delves into the study of wave propagation in 3D through acoustic metamaterials. The understanding of the fundamentals of wave propagation in acoustic metamaterials and the analytical skills gained in the first chapter have laid the foundation for this current chapter. Additionally, the research in the second chapter on Biot's theory of poroelasticity, as well as the design of an acoustic lens for ultrasound wave focusing using water-saturated microlattices, also contributed to this current study on wave propagation in 3D environment through acoustic metamaterials.

Functional ultrasound imaging enables sensitive, high-resolution imaging of neural activity in freely behaving animals and human patients. However, the skull acts as an aberrating and absorbing layer for sound waves, leading to most of the functional ultrasound experiments being conducted after skull removal. In pre-clinical settings, craniotomies are often covered with a polymethylpentene film, which offers limited longitudinal imaging, due to the film's poor conformability, and limited mechanical protection, due to the film's low stiffness. Here, we overcome these problems by introducing conformal plate skull replacements consisting of microlattice metamaterials with enhanced quasi-static mechanical properties and acoustic characteristics. A microscale 2-photon polymerization technique is adopted to fabricate a conformal acoustic window with high stiffness-to-density ratio and sonotransparency. We demonstrate the fitness of the metamaterial acoustic window in vivo via terminal

and survival experiments on small animals. Long-term biocompatibility and lasting signal sensitivity are demonstrated over a long period of time (> 4 months) by conducting ultrasound imaging in mouse models implanted with the metamaterial skull prosthesis.

5.2 Introduction

Functional ultrasound imaging (fUSI), the ultrasound analogue of functional magnetic resonance imaging (fMRI), enables the imaging of whole-brain activity with high spatio-temporal resolution and high sensitivity [1, 2]. Based on the power Doppler technique [3], fUSI records brain dynamics by measuring the variation of cerebral blood volume, indirectly coupled to cerebral activity through the neurovascular coupling. fUSI has been used in many different animal models from rodent [4, 5] to primate [6] and in humans [7, 8], and it can easily be combined with other brain recording technology such as optical [9] or electrical modalities [10]. Moreover, fUSI can easily be adapted for awake head-fixed or freely-moving animals [11] and it is suitable for pharmacological studies using functional connectivity as a readout [12].

To ensure high sensitivity to smallest blood volume variations, fUSI relies on high frequencies (typically between 5 MHz and 15 MHz), which are sensitive to bone's attenuation and aberration [13]. This is different from low-frequency focused ultrasounds (typically between 0.2 MHz to 1 MHz) used for therapeutic applications, where transcranial procedures are possible [14]. As a result, most fUSI applications require circumventing the skull, through open craniotomy [4, 6] or thinned skull procedures [15]. For chronic studies, the skull can be replaced with an acoustically transparent bio-polymeric cranial window, to preserve the integrity of brain tissue over multiple days [10, 16]. The literature has extensively reported the use of polymethylpentene (PMP) sheets to replace the skull for ultrasound imaging experiments (see Table S1). However, PMP sheets have a planar shape, making the replacement of complex skull geometry impossible. Furthermore, the Young's modulus of commercially available PMP sheets (< 2 GPa) is generally lower than that of the skull (3.5 GPa), which makes them compliant and easily deformable.

To optimize the quality and outcome of fundamental neuroscience studies relying on ultrasound imaging, the shape of a skull-replacement implant should (i) be adjustable, (ii) have a high stiffness-to-density and (iii) be sonotransparent. Therefore there is a clear need for a conformal acoustic window with enhanced quasi-static

mechanical properties and impedance matched acoustic characteristics.

Mechanical metamaterials (MMs) are rationally designed materials that derive their properties from the selection of their constitutive materials and from the geometry of their micro- and meso-structures. MMs have been shown to exhibit unprecedented mechanical properties, in both static and dynamic loading regimes. For example, MMs can have very high stiffness and strength at low density [17–19], or are capable of manipulating elastic and acoustic waves beyond naturally defined limits [20–22]. Acoustic metamaterials (AMMs) are the subset of MMs aimed at manipulating acoustic waves, capable of achieving selective transmission [23–35], cloaking [36, 37], or focusing and lensing [38, 39]. AMMs can achieve near perfect transmission via resonance²⁴, zero or negative density [29–31], narrow apertures [32, 33], impedance matching [34, 35], and overcome the presence of aberrating layers [24–27]. However, most of the proposed solutions only work within a narrow frequency bandwidth, which limits their applications for broader use [23–28, 32, 33]. Earlier works demonstrated the use of MMs to image through a stiff and lossy barrier [25, 26], however, these AMMs do not conform to a real skull geometry and do not account for the irregularities and inhomogeneities of bone. As such, existing designs are not readily applicable to solve in-vivo problems. Furthermore, previous studies only design AMMs for desired acoustic properties, without taking into consideration their quasi-static response to simultaneously function as a mechanical and protective barrier [23, 28–35].

Here, we focus on the realization of MMs that can be implanted as custom-formed skull replacements. These materials are intended to function both as a protective layer for the brain and as a transparent window for ultrasonic waves. They are designed to have a high stiffness-to-density ratio (comparable to bone), and can conform to arbitrary skull sections (Fig. 1a,b). We label these materials “Metaskulls”, or MSs.

Literatures using polymethylpentene (PMP) films for cranial window

PMP films have been widely used as a cranial window for ultrasound imaging for small animals due to its low attenuation properties at higher frequency range (> 10 MHz) [40, 41]. Some of the comprehensive literatures using PMP films are tabulated (Table 5.1).

Year	Journal	Author	Type	Animal model
2000	IEEE	Bloomfield, P. E. <i>et al.</i> [40]	Material characterization	
2011	Ultrasound med. biol.	Madsen, E. R. <i>et al.</i> [41]	"	
2015	Nature methods	Sieu, L.-A. <i>et al.</i> [10]	fUSI	Rat
2016	Neuroimage	Demene, C. <i>et al.</i> [42]	"	Rat
2018	eLife	Bimbard, C. <i>et al.</i> [5]	"	Ferret
2018	IEEE	Koekkoek, S. K. E. <i>et al.</i> [43]	"	Mouse
2018	Nature comm.	Bergel, A. <i>et al.</i> [16]	"	Rat
2020	Scientific reports	Rahal, L. <i>et al.</i> [44]	"	Rat
2021	Nature protocols	Brunner, C. <i>et al.</i> [45]	"	Mouse
2021	NeuroImage	Edelman, B. <i>et al.</i> [46]	"	Mouse
2022	Comm. biology	Reaux-Le-Goazigo, A. <i>et al.</i> [47]	"	Rat
2022	The Lancet	Demeulenaere, O. <i>et al.</i> [42]	"	Mouse
2022	Neurophotonics	Tournissac, M. <i>et al.</i> [48]	"	Mouse

Table 5.1: Literatures with the characterization of PMP, and PMP films as a cranial window.

5.3 Concept

To achieve both quasi-static mechanical robustness and acoustic transparency in the ultrasonic regime, we designed MMs with structural features in the micrometer scale, arranged in honeycomb plate lattices, which we fabricated using 2-photon polymerization (2PP, Fig. 5.1c). The inner structures of the metaskulls are designed to be impedance matched with biological tissue, to enable low loss transmission of ultrasonic waves for imaging brain activity in small animals (~ 15 MHz) [1]. To evaluate numerically the quasi-static and dynamic mechanical properties of the metaskulls, we implemented finite element (FE) models, which we verify with experiments. We conducted *in vivo* tests in mice, to evaluate the brain imaging quality using metaskulls with varying thickness, by measuring both the total intensity and signal-to-noise ratio (SNR) of the signal. To demonstrate the long-term stability of the metaskulls for brain imaging, we performed longitudinal experiments *in vivo* via Doppler ultrasound imaging with visual stimulation.

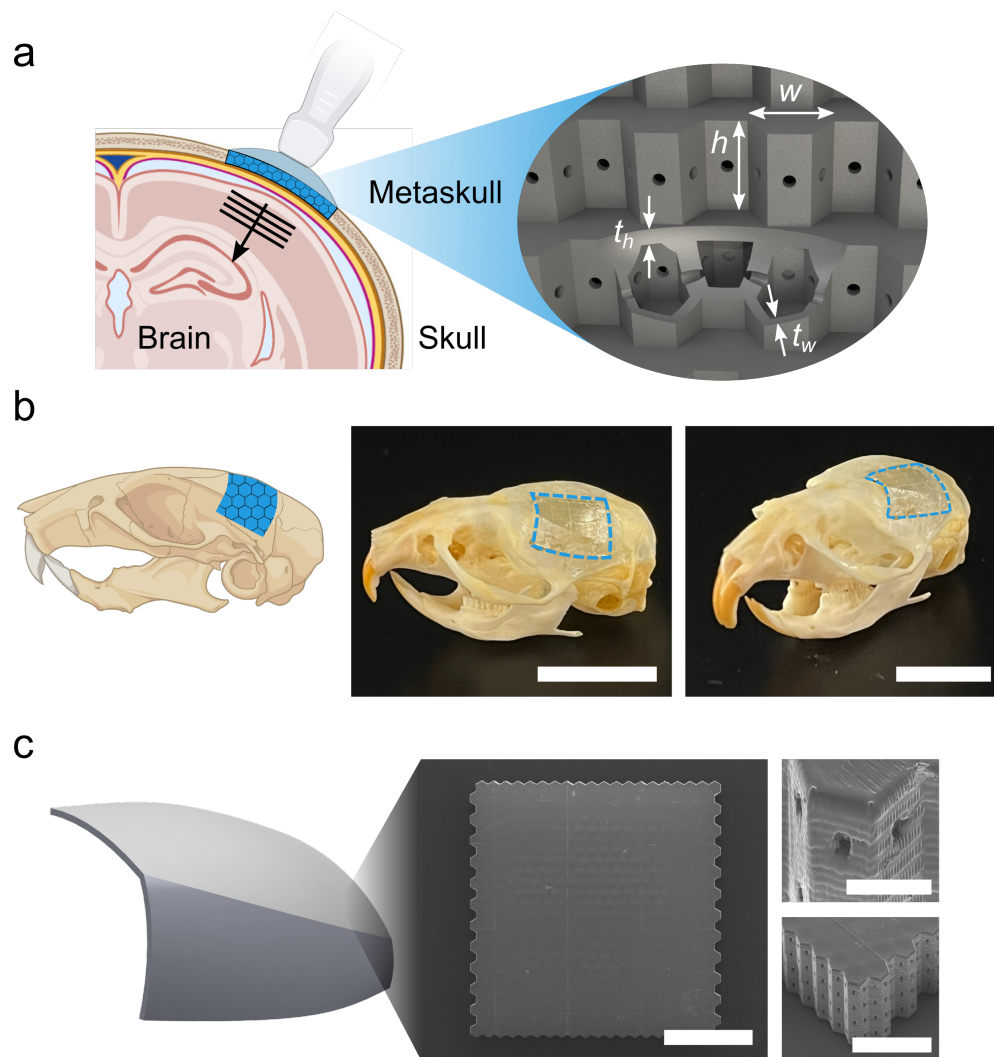


Figure 5.1: Design and structure of the metaskull. **a**, Concept schematic illustrating ultrasound brain imaging through the metaskull. A 3D model of the inner structures of the metamaterials shows a periodic tessellation of honeycomb unit cells, with $h = 37 \mu\text{m}$, $w = 32.3 \mu\text{m}$, $t_h = 7.5 \mu\text{m}$, and $t_w = 4.5 \mu\text{m}$. **b**, The metaskull can fit an arbitrarily shaped region in a curved parietal lobe of the mouse skull. **c**, The metaskulls are fabricated with a microscale 2-photon polymerization technique. SEM images of the sample of the metaskull from the top and isometric views. Scale bars: **b**, 1 cm; **c**, 200 μm (left), 100 μm (bottom right), and 20 μm (top right).

Mechanical metamaterials as a conformal cranial window

We designed the metaskulls which to be acoustically transparent to ultrasound waves around 15 MHz, to meet fUSI requirements, and to have a high compressive Young's modulus for minimal deformation in the vertical direction (Fig. 5.1a). To achieve a structured material's stiffness as close to its theoretical limit as possible, we constructed the unit cell of the metaskulls based on a honeycomb panel with

hexagonal lattices [49]. The microlattices are composed of polymerized IP-S, which is an acrylic polymer cured from its viscous liquid photoresist state, suitable for fabricating biocompatible microscale metamaterials with intricate inner structures [50]. The unit cell of the honeycomb microlattices consists of a cavity surrounded by an outer wall with horizontal drainage through holes (5 μm in diameter) (Fig. 5.1c). The cavities are filled up with air to match the MMs' acoustic impedance to that of the biological tissue ($Z_{\text{tissue}} = 1.5 \text{ MRayl}$). The 2PP method leaves uncured photoresist trapped inside the cavity of the unit cell, which increases the effective acoustic impedance of the metamaterials if it remains inside. We placed the through-holes in the vertical walls which allowed the trapped photoresist to escape from the cavities, leaving only air inside the metamaterials.

5.4 Quasi-static characterization of the metaskull

FEA for the mechanical characterizations

We performed the numerical mechanical characterization of the metaskulls under quasi-static or dynamic loading via FE analysis using a commercial FE software (COMSOL Multiphysics®) (Fig. 5.2b, 5.7a). The models used for the simulations consist of a 4-unit-cell thick metaskull with a 300 μm diameter circular face. Mimicking the compression experiment setup shown in Figure 5.2a, 50 μm X 50 μm square-faced punch was compressed against the plate-lattice domain. Assuming linear elasticity and geometric linearity, we computed the simulation to plot the von Mises stress distribution on xz - and yz -planes which shows the stress concentration along the drainage holes.

We numerically calculated the global response of the honeycomb plate-lattices under compression using a linear elastic model. The FE simulation is modeled after the experimental setup for the compression test (FemtoTools AG) for the computation of the deformation and stress distribution of the 4-unit-cell-thick, finite-sized honeycomb lattices (Fig. 5.2a). To minimize the boundary effect, we built the lattice model larger than the front face of the tip (Fig. 5.4). Compared and normalized against the 125- μm -thick PMP model with $E = 1.5 \text{ GPa}$, the compressive Young's modulus of the honeycomb metamaterials was calculated to be 3.08 GPa. As expected, the von Mises stress distribution of the model shows that the stress and deformations are concentrated below the compressed region, especially around the horizontal drainage holes (Fig. 2b). The presence of the horizontal holes decreases the effective stiffness of the honeycomb plate-lattices by 12.4%.

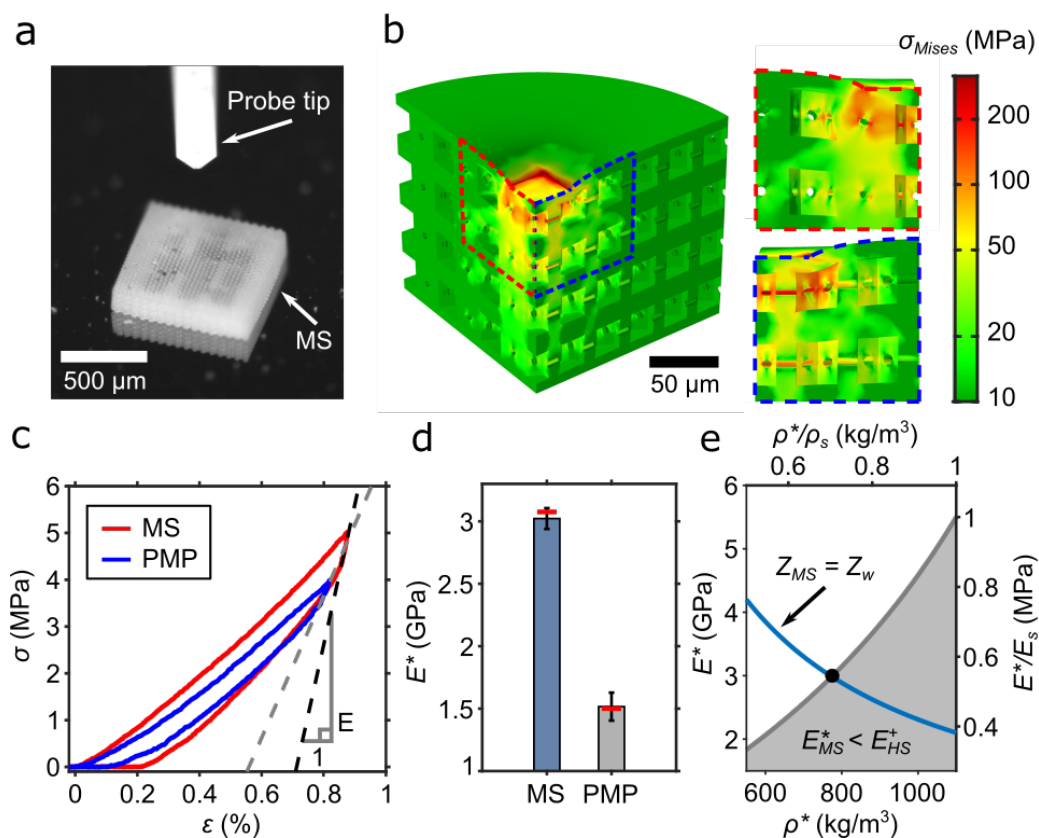


Figure 5.2: Quasi-static mechanical characterization of the metaskull meta-materials. **a**, Optical microscopy image of a metaskull sample for compression testing, along with the probe tip of the measurement system. **b**, Von Mises stress distribution within the FE model compressed with a $50\ \mu\text{m} \times 50\ \mu\text{m}$ square-faced probe tip. A quarter of the model is shown for the cross-sectional views. Side-view images show the stress concentration around the drainage holes. **c**, Stress-strain curves showing the single loading-unloading cycle of the honeycomb plate-lattices and a PMP film under indentation. Dashed lines indicate the slopes at the onset of the unloading curve, which are used to calculate the effective Young's moduli. **d**, The average and standard deviation of the Young's modulus obtained from experiments, for both the honeycomb plate-lattices and a PMP film. Red lines indicate the prediction from the numerical simulation or known material properties. **e**, The theoretical upper bound for the modulus of a two-phase, isotropic material (gray) crossed by an isoline matching the acoustic impedance of the brain (blue), both as a function of the Young's modulus and density of the constituent solid. The acoustic impedance of the brain is constant at 1.52 MRayl and follows a relation, $Z = \sqrt{\rho E}$. The normalized Young's modulus and relative density are normalized with the Young's modulus and density of IP-S, respectively.

Compression test results of the metaskull and a PMP film

We show the quasi-static compression data acquired from 5 independent measurements of the metaskull ($148\ \mu\text{m}$) and a PMP film ($125\ \mu\text{m}$) each (Fig. 5.3). All

the measurements were calibrated using the reference stiffness of the testing system ($k_{ref} = 28,000 \text{ N/m}$) [51]. We converted the force-displacement data to stress-strain data using the area of the probe tip and the thickness of the films under compression. The strain rate lower than 0.001 s^{-1} was applied to all the measurements. The slope at the start of the unloading curves shows the global response of the samples under compression, representing the effective compressive modulus.

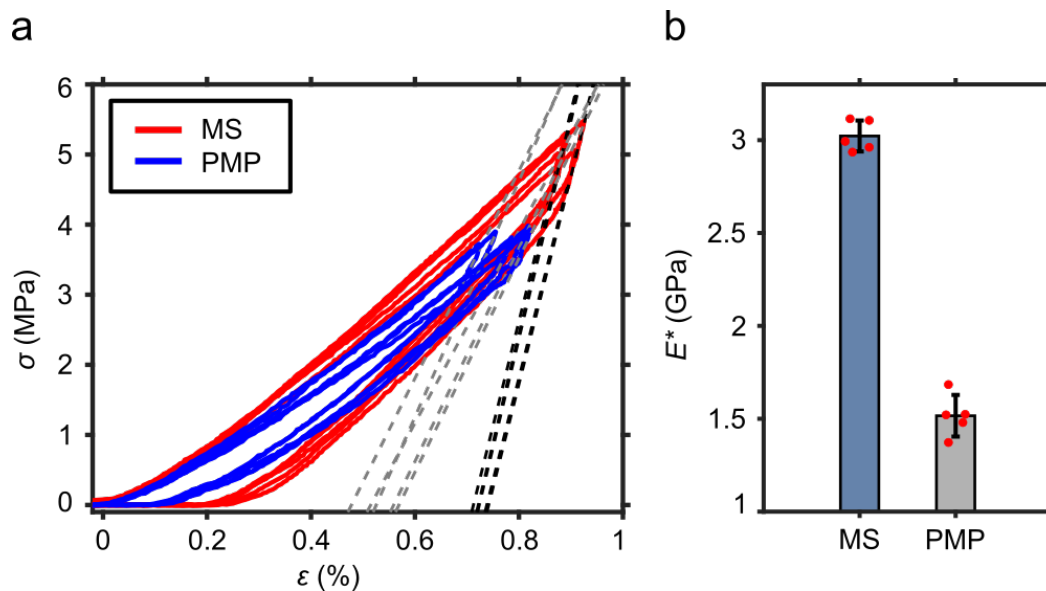


Figure 5.3: Quasi-static mechanical testing. **a**, Sets of 5 independent stress-strain curves of the metaskull ($148 \mu\text{m}$) and a PMP film ($125 \mu\text{m}$) tested with the indentation experiment setup. **b**, Bar graph shows the distribution, average, and standard deviation of the effective Young's modulus derived from the measurement data.

The mean effective compressive modulus measured from independent compression tests of the 3D-printed honeycomb plate-lattices is $3.02 \text{ GPa} \pm 83.4 \text{ MPa}$ (standard deviation), which is in good agreement with the numerical prediction (3.08 GPa) (Fig. 5.2d). As a reference, we also measured the compressive response of a PMP film, from which we extracted a Young's modulus of $1.52 \text{ GPa} \pm 112.1 \text{ MPa}$. The dimensions of the honeycomb plate-lattice unit cells were optimized so that the metaskull can be impedance-matched to biological tissue, while preserving the highest possible quasi-static stiffness. The stiffness of the honeycomb metamaterials lies on the edge of the theoretical limit, which is the Hashin-Shtrikman upper bound for two phase materials [52] (Fig. 5.2e).

Numerical simulation on the effect of the radius of the compressed model

The quasi-static finite element (FE) model consists of a square-faced probe tip for compression and a 125 μm thick PMP film ($E = 1.5 \text{ GPa}$), cut in quarters for computational and graphical purposes (Fig. 5.4a). The face of the probe tip is 50 μm X 50 μm large, hence a model wide enough in the lateral direction was required to properly mimic thin film compression tests without boundary effect. We conducted a parametric compression study as a function of the radius, r , on a monolithic, circular-faced PMP film model to determine the optimal size for the simulation. The radius was swept from 25 μm to 250 μm with progressively increasing step size. We calculated the Young's modulus of a film by dividing the reaction force with the area of the face of the probe tip, and also with the corresponding strain. The effective modulus increases as the diameter gets bigger before it saturates at the radius above 150 μm (Fig. 5.4b). Since the computation cost significantly increases with a bigger model size, the diameter of the model for the compression simulation was set as 150 μm . We further normalized the simulation results considering the structural factor to match the Young's modulus of the PMP.

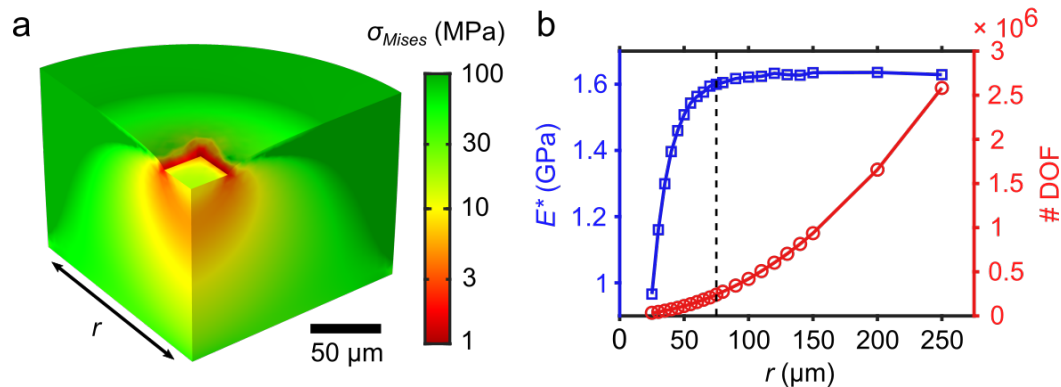


Figure 5.4: Characterization of the boundary effect. **a**, The FE model for the compression simulation of a monolithic PMP film. The von Mises stress distribution within the film under 1 μm indentation is shown on the cross sections of the model. **b**, Effective compressive modulus (blue, square), and the number of degrees of freedom (red, circle) as functions of the radius of the model. Beyond $r = 150 \mu\text{m}$ (black, dashed), the value of the modulus saturates while the computation cost increases significantly.

Compression simulation on the effect of the structural nonlinearity

We compared the quasi-static properties of the honeycomb plate-lattices with and without the geometric nonlinearity (Fig. 5.5). The linear response does not deviate from the nonlinear response by more than 0.7% when the applied stress reaches

4.5 MPa (Table 5.2), which is above the typical acoustic pressure range for the ultrasound imaging (0.1 - 4 MPa) [53]. In addition, the engineering strain is 0.14% for 148 μm thick lattices at $z = 0.2 \mu\text{m}$, which makes the material's deformation safely within the linear elastic regime. Based on the analysis, we show that linearity in both structure and materials can be assumed for expedited computation without compromising the accuracy of the FE models.

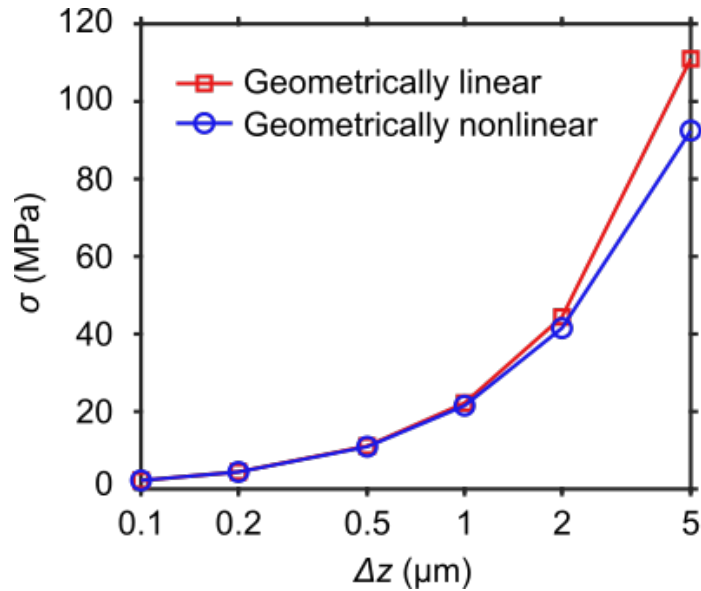


Figure 5.5: Characterization of the geometric nonlinearity. The applied stress as a function of deformation displacement for both geometrically linear (red, square) and nonlinear (blue, circle) cases. The discrepancy between two cases gets negligible for small deformation.

Δz (μm)	σ_{lin} (MPa)	σ_{nlin} (MPa)	<i>Error</i> (%)
0.1	2.22	2.23	-0.51
0.2	4.44	4.41	0.66
0.5	11.10	10.09	1.57
1	22.19	21.50	3.11
2	44.39	41.51	6.49
5	110.97	92.47	16.67

Table 5.2: Resultant stresses under compression. σ_{lin} and σ_{nlin} indicate the resultant stresses under the deformation, Δz , assuming geometric linearity and nonlinearity, respectively. The error is calculated as $Error = (\sigma_{lin} - \sigma_{nlin})/\sigma_{lin} \times 100\%$.

The effect of the presence of the drainage holes in the metaskull

The 2PP technique facilitates the rapid fabrication of complicated geometry with ease, however, drainage holes must exist to remove uncured photoresist from the inner cavities of the honeycomb plate-lattices. The effective mechanical properties and structural integrity are affected by the presence of the drainage holes, since we lose a mass that can withstand the applied load. As a result, the effective Young's modulus decreases from 3.51 GPa to 3.08 GPa, reduced by 12.4%. The drainage holes also weaken the structure by working as a stress concentration center when the load is applied [54]. The highest von Mises stress on the perimeter of the hole (dashed circle in blue in Fig. 5.6) reads 260 MPa, which is higher than the stress found in the same position of the intact structure (100 MPa).

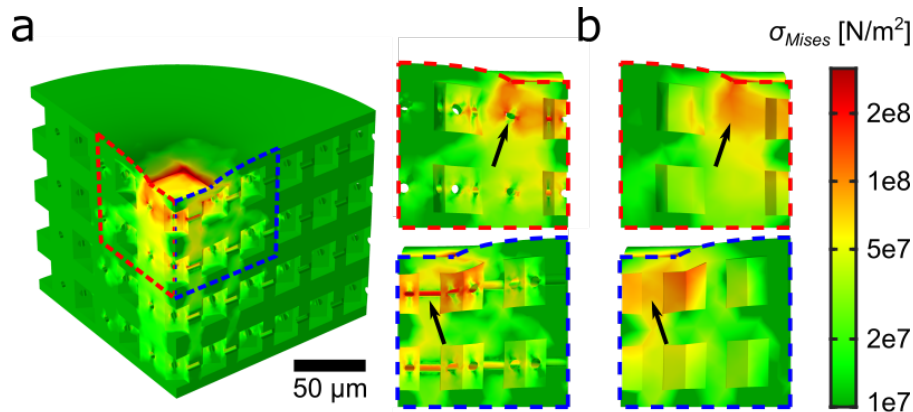


Figure 5.6: Effect of the drainage holes to the structural integrity. **a**, The FE compression model with horizontal drainage holes showing the von Mises stress distribution on the cross sections. **b**, The FE model without the drainage holes shows less concentrated stress within the metamaterials.

Micro fabrication process of the metaskulls

We adopted the microscale 2PP technique for the fabrication of the metaskulls with intricate inner structures (Nanoscribe GmbH & Co. KG). The photoresist, IP-S, in the form of highly viscous liquid becomes acrylic when cured under laser irradiation. After printing the desired metaskull geometry, we develop the metaskull using propylene glycol monomethyl ether acetate (PGMEA) and isopropyl alcohol (IPA). The presence of the drainage holes allows the remaining photoresist to be thoroughly removed from the cavities. We measured the mass of the metaskull samples before and after underwater tests to confirm that the cavities are saturated with air, trapped inside the structure due to surface tension. For microscopic images, only 25 X 24 X 4 arrays of unit cells were printed, which resulted in a sample with

outer dimensions of $590 \mu\text{m} \times 574 \mu\text{m} \times 148 \mu\text{m}$ (Fig. 5.2a). Since the single printing size of the Nanoscribe Photonic Professional GT ($300 \mu\text{m} \times 300 \mu\text{m} \times 300 \mu\text{m}$) is smaller than the final dimension, smaller blocks were stitched together to form a larger final structure.

Compression experiments on the metaskull samples

The quasi-static characterization was performed using a micromechanical testing tool (FemtoTools AG, FT-MTA02) (Fig. 5.2a). A displacement-controlled probe tip with a square end (FT-S100,000) was compressed against the metaskull sample composed of honeycomb unit cells for force measurement. The size of the sample used for testing ($700 \mu\text{m} \times 700 \mu\text{m} \times 148 \mu\text{m}$) was larger than the front end of the tip ($50 \mu\text{m} \times 50 \mu\text{m}$), so that boundary effects could be neglected (Fig. 5.4). The probe tip recorded the force signal as the measuring arm traveled downward $2 \mu\text{m}$ from the top surface. Calibration test against a rigid substrate surface was done prior to the measurements to offset the deformation of the measuring arm under given force. The reference stiffness of the measuring system, $K_{ref} = 28,000 \text{ N/m}$, was then used for the calibration. We took the sample's effective stiffness from the beginning of the unloading curve, which indicates the global response of the lattice.

5.5 Dynamic characterization of the metaskull

Calculation and visualization of the dispersion curves

Numerical simulations were performed using a commercial FE software (COMSOL Multiphysics®). The dispersion curves of the metaskulls were derived by numerically solving the characteristic equation of the honeycomb unit cell. Bloch-Floquet periodic boundary conditions were applied on all sides, assuming infinite periodicity. With evenly-spaced wavenumbers sweeping within the irreducible Brillouin zone, the eigenfrequencies below 50 MHz were calculated to best represent the behavior of the metamaterials around the operating frequency of fUSI for small animals ($\sim 15 \text{ MHz}$). With incident plane waves traveling in the z -direction, $\Gamma - A$, the volume-averaged displacements in each direction were normalized with the total volume-averaged displacement. We determined the longitudinal polarization of each normal mode based on the dominant direction of deformation. The longitudinal polarization factor is defined as $\frac{w}{\sqrt{u^2+v^2+w^2}}$ where u , v , and w are the displacements in x -, y -, and z - directions, respectively. If the longitudinal polarization factor of one normal mode is close to 1, the mode has dominant pressure wave behavior, as opposed to when the transverse mode is dominant and the polarization factor is

close to 0. With blue being purely longitudinal and red being purely transverse, the dispersion curves were plotted to indicate the polarization of the mode at each solution (Fig. 5.7b). The dispersion curves of the honeycomb unit cell in different wave directions were calculated by sweeping the Brillouin zone in the reciprocal domain. The wavenumber vectors $k = (k_x, k_y, k_z)$ parallel to $\Gamma - A$, $\Gamma - \beta L$, $\Gamma - \beta H$ with $\beta = 0.2, 0.5$, or 1 , are used for the dispersion curves.

We computed the dispersion curves in the $\Gamma - A$ direction in the Brillouin zone, to investigate the wave propagation characteristics of the metaskulls under plane acoustic waves, in the z-direction (Fig. 5.7b). We designed the geometry of the metaskull's unit cell so that the pressure waves have minimal transmission loss at 15 MHz. The proposed design has a linear longitudinal branch around 15 MHz, which allows dispersionless propagation of waves around the operating frequency. We further ensure that there is no hybridization between the longitudinal modes and shear modes. As a result, the energy loss due to transverse mode conversion from the longitudinal mode is minimized by avoiding normal-to-shear coupling [55]. We designed the metaskull to have a shear mode band gap between 11.4 and 20.2 MHz, leading to the suppression of shear waves' conduction through the skull of the subjects [56]. The acoustic impedance of the metaskulls is matched to biological tissue, to achieve zero reflection at the water-metaskull interface. At 15 MHz, the group velocity, c_g , of the longitudinal wave through the honeycomb plate-lattices is 1938.7 m/s with the effective density, ρ_{eff} , equal to 775.6 kg/m³, making the acoustic impedance of air-saturated plate-lattices along the vertical direction 1.504 MRayl.

Transmission simulation for the metaskull

In addition, we built the transmission models to assess the acoustic characteristics of the traveling pressure waves with respect to the frequency and the angle of incidence (Fig. 5.7a). The input and output pressure field, padded with perfectly matched layers, sandwich a column of honeycomb plate-lattices composed of a finite number of unit cells ($n = 3, 4, 5, 7$, and 9). We imposed the Bloch-Floquet periodic boundary conditions on the side faces to assume infinite periodicity in the lateral directions. The viscoelastic dissipation of the constituent polymer was incorporated by feeding an isotropic structural loss factor ($\eta = 0.075$) to the materialistic model [57]. We evaluated the amplitude of the traveling pressure waves in the output pressure field, and showed the transmission curves in dB, $10\log(P/P_{ref})$ (Fig. 5.7d).

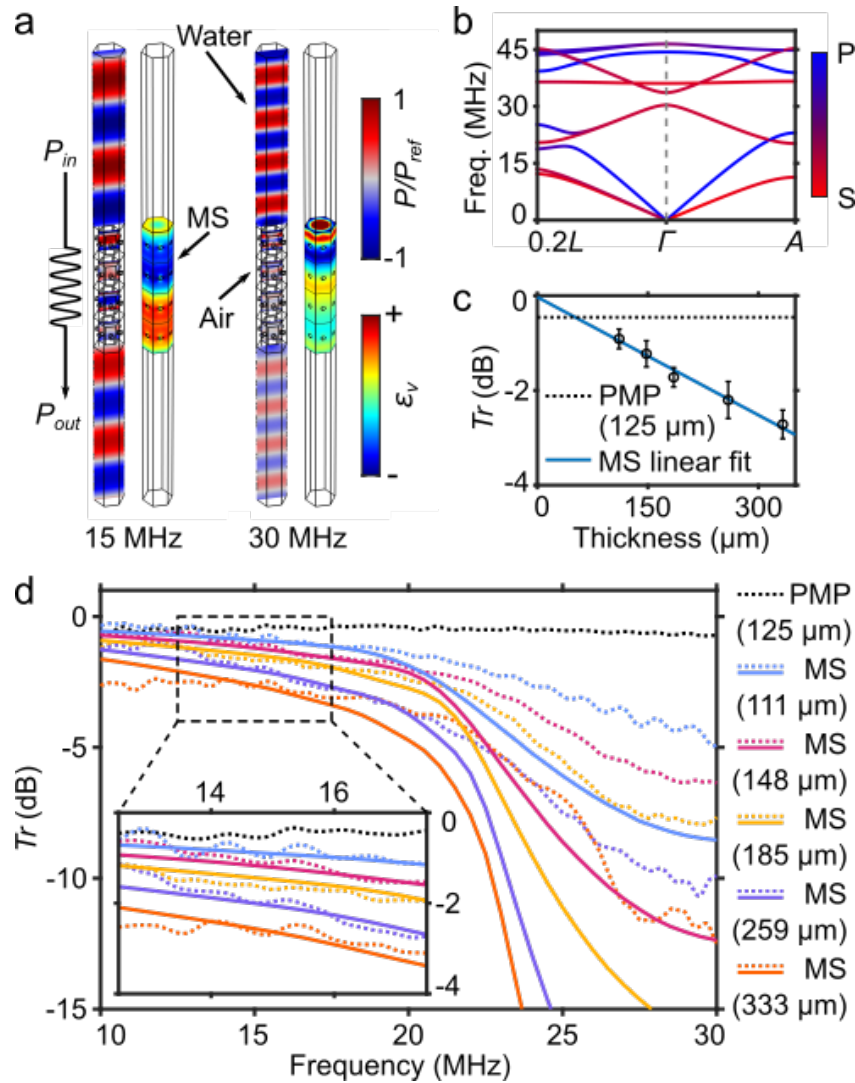


Figure 5.7: Characterization of dynamic mechanical properties of the metaskulls. **a**, FE model for the ultrasonic wave propagation at 15 and 30 MHz through 4 unit cells of the honeycomb plate-lattices in water. (Left) Pressure distribution within the water surrounding the metaskulls and the air inside the cavities. (Right) The volumetric strain distribution within the honeycomb metamaterials. **b**, The dispersion curves of the honeycomb metamaterials in both $\Gamma - A$ and $\Gamma - 0.2L$ directions. Curves' colors indicate the longitudinal polarization of each mode (blue: pressure mode, red: shear mode, and purple: hybridized mode). **c**, Experimental transmission coefficients of the metaskull samples with varying thickness averaged between 13.75 and 17.5 MHz, shown with error bars. The slope of the linear regression plot (blue, solid, $r^2 = 0.99$) is -83.0 dB/cm, whereas the attenuation coefficient of a 125- μm -thick PMP film (black, dashed) is -36.6 dB/cm. **d**, Both experimentally measured (dotted) and numerically derived (solid) transmission curves of a PMP film (black, dotted) and the metaskulls with varying thickness with respect to frequency.

Transmission simulation: Frequency dependent pressure & volumetric strain curve

We compared the acoustic pressure and volumetric strain distribution of the metaskulls at two different frequencies, 15 and 30 MHz. Both water and air pressures are normalized by the peak pressures in each medium. Unlike Figure 5.7, 9-unit-cell structures were modeled for comprehensive analysis of the strain distribution (Fig. 5.8a). For the quantitative evaluation of the attenuation, we plotted the pressure and strain profiles along the pressure fields and the metaskull, respectively, both as a function of traveling distance. Both the water and the air pressure amplitudes were self-normalized with their own maximum pressure for visualization (Fig. 5.7a). The pressure amplitude in the output field at each frequency is -2.73 dB at 15 MHz and -31.20 dB at 30 MHz. At 30 MHz, the input frequency lies within the Bragg band gap of the longitudinal mode (between 23.05 and 38.94 MHz), and as a result, the amplitude of pressure waves exponentially decays as they travel through the metaskull. At 15 MHz, the only source of attenuation originates from viscoelastic dissipation within the constituent solid which causes linearly attenuating amplitude (Fig. 5.8b).

We experimentally validated the numerical predictions for the acoustic properties of the metaskulls by measuring the transmission coefficient with respect to the input frequency (Fig. 5.7d). The metaskull samples with different thickness (111, 148, 185, 259, and 333 μm) were used for the transmission measurements. The discrepancy between the transmission coefficients at higher frequencies measured in experiments and simulations was due to the finite size of the metaskull samples and to boundary effects, leading to weaker attenuation. The transmission coefficients between 13.75 and 17.5 MHz for each sample were averaged and their values were linear-fitted, along with the attenuation coefficient of the 125- μm -thick PMP film, as a reference (Fig. 5.7c). The curve-fitted transmission loss data extrapolate to the origin, implying zero reflections at the water-metaskull interface, since the metaskulls are acoustically matched to biological tissue. The attenuation coefficient of the metaskulls, 83.0 dB/cm, is larger compared to that of the PMP film, 36.6 dB/cm, both at 15 MHz. This higher attenuation from the metaskull is caused by a larger number of interfaces from the additive manufacturing. However, we show in the subsequent sections that the fUSI qualities are acceptable even with the slightly increased attenuation.

We investigated the transmission characteristics of the metaskulls by numerically

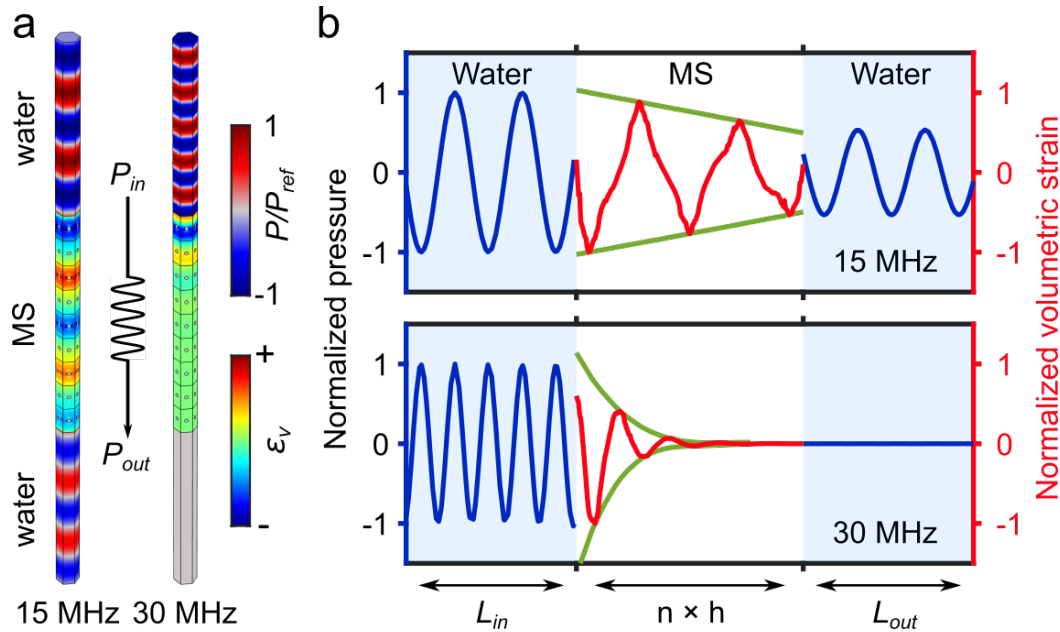


Figure 5.8: Frequency dependent pressure and volumetric strain distribution. **a**, The FE models for transmission simulation showing the input and output pressure fields, and the metaskull. The acoustic pressure and volumetric strain distribution at 30 MHz show more steep attenuation of the traveling waves. **b**, The pressure (blue) and volumetric strain (red) profiles along the vertical axis at 15 and 30 MHz. The envelopes (green) imply different attenuation characteristics at different frequencies.

analyzing the frequency dependent response (Fig. 5.7a). The attenuation through the 4-unit-cell metaskull at 15 MHz is 1.20 dB, which is significantly smaller than the attenuation at 30 MHz, by 90%. The volumetric strain distribution within the constituent solid as a function of the traveling distance shows that the amplitude of the traveling waves attenuates for both cases, but with much greater loss at the higher frequency (Fig. 5.8). The higher transmission loss at 30 MHz is attributed to the presence of a longitudinal band gap between 23.05 and 38.94 MHz, whereas the loss at 15 MHz arises from the viscoelastic dissipation of the polymer itself [57]. With gradually increasing frequency, the slope of the attenuation curve gets steeper and nonlinear as the frequency increases above 18 MHz, and the attenuation dramatically increases above 20 MHz (Fig. 5.7c).

Transmission simulation: Evaluation of the contribution of the viscosity of air, and the viscoelastic dissipation of solid

We investigated the contribution of the viscosity on the acoustic characteristics of the metaskulls by comparing the pressure and volumetric strain profiles (Fig. 5.9a). The models with and without the viscosity of air and the viscoelasticity of the

constituent polymer are built for the numerical simulation. To match numerical transmission curves to the experimental results, isotropic loss factor, η , at 0.075 is used for the models to account for the viscoelasticity of the solid [57]. The attenuation coefficients are evaluated for all 4 cases under the same conditions: $f = 15$ MHz, $n = 9$, and $\theta_i = 0^\circ$. The transmission loss of the vacuum-filled model in the absence of energy dissipation from the constituent materials is $-1.32 \cdot 10^{-4}$ dB, which is negligible. The model, including the effects viscosity from the constituent solid and air inside the cavities, loses the pressure wave energy by 2.73 dB. The result is the summation of each case.

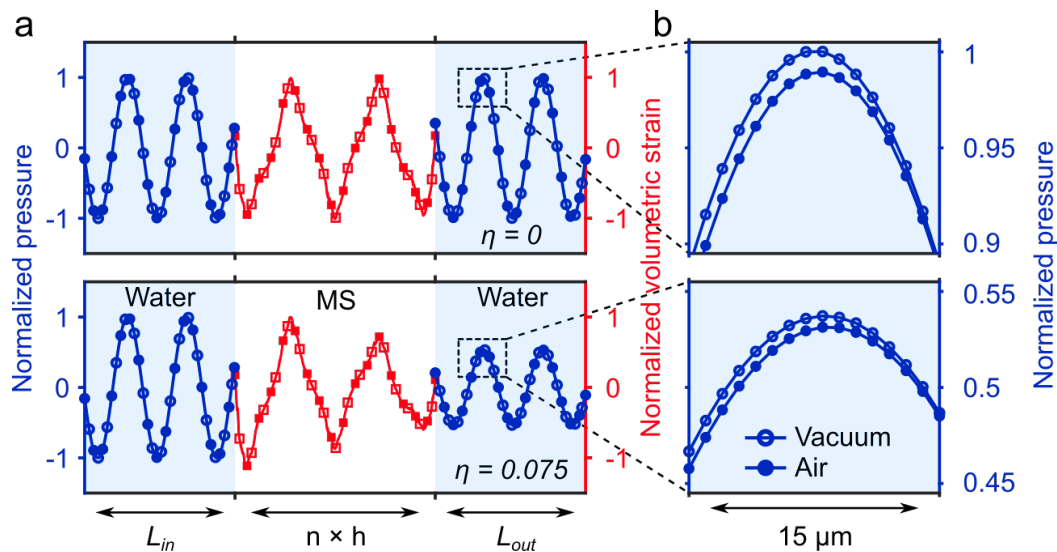


Figure 5.9: Effect of the viscosity of air and the viscoelasticity of the solid to the transmission. **a**, (Top) The acoustic pressure and the volumetric strain profiles when the viscoelasticity of the solid is ignored. (Bottom) The profiles with the isotropic loss factor, η , at 0.075. For both plots, the profiles with or without the air inside the cavity of the metamaterials are not distinguishable. **b**, The magnified views of the parts of the profiles from the left panel showing the attenuation due to the viscosity of air.

Transmission simulation: Advantage of the honeycomb plate-lattices with horizontal holes over vertical holes

The drainage holes can also be placed vertically in the unit cell of the metaskull as opposed to horizontally as shown in Fig. 5.10b. Nevertheless, the vertical through holes must be avoided for two reasons. First, we need to prevent biological fluid or external contaminants, such as bacteria or viruses, from traveling freely through the cranial window. Allowing direct passages to the brain may cause adverse inflammation that will undermine the purpose as a protective barrier. Another reason

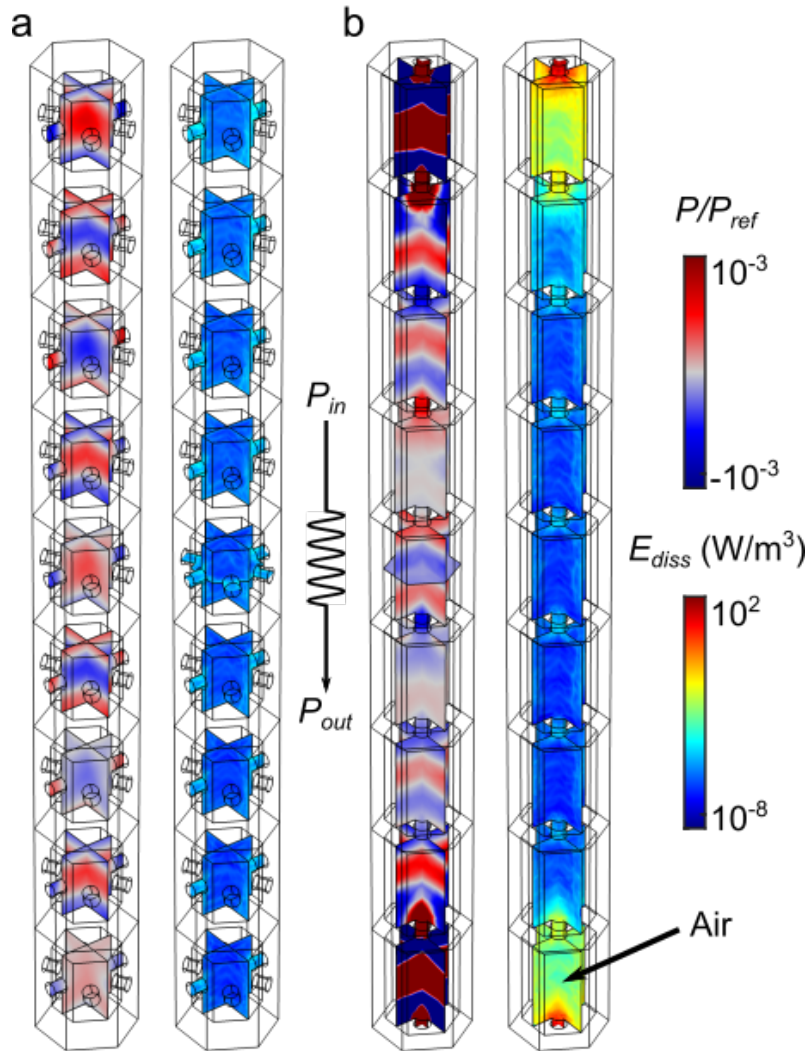


Figure 5.10: Thermoviscous dissipation with respect to the direction of the drainage holes. **a**, The acoustic pressure (left) and the thermoviscous energy dissipation (right) distributions within the air inside the cavities of the horizontally holed metamaterials. The pressure distribution is normalized by the pressure of the input waves. **b**, The acoustic pressure (left) and the thermoviscous energy dissipation (right) distributions within the air inside the cavities of the vertically holed metamaterials.

is that the viscous attenuation due to the horizontal holes is much smaller than the attenuation due to the vertical holes. A periodic placement of vertical through-holes across the metaskulls is structurally identical to micro perforated panels, which are known as good sound absorbing layers [58]. The pressure gradient along the cavities connected with the vertical holes results in viscous attenuation along the neck, which is orders of magnitude higher than the attenuation within the horizontal

holes. Ideally, there is little to no pressure gradient across the horizontal cavities, especially when the incident angle of the plane waves is 0° .

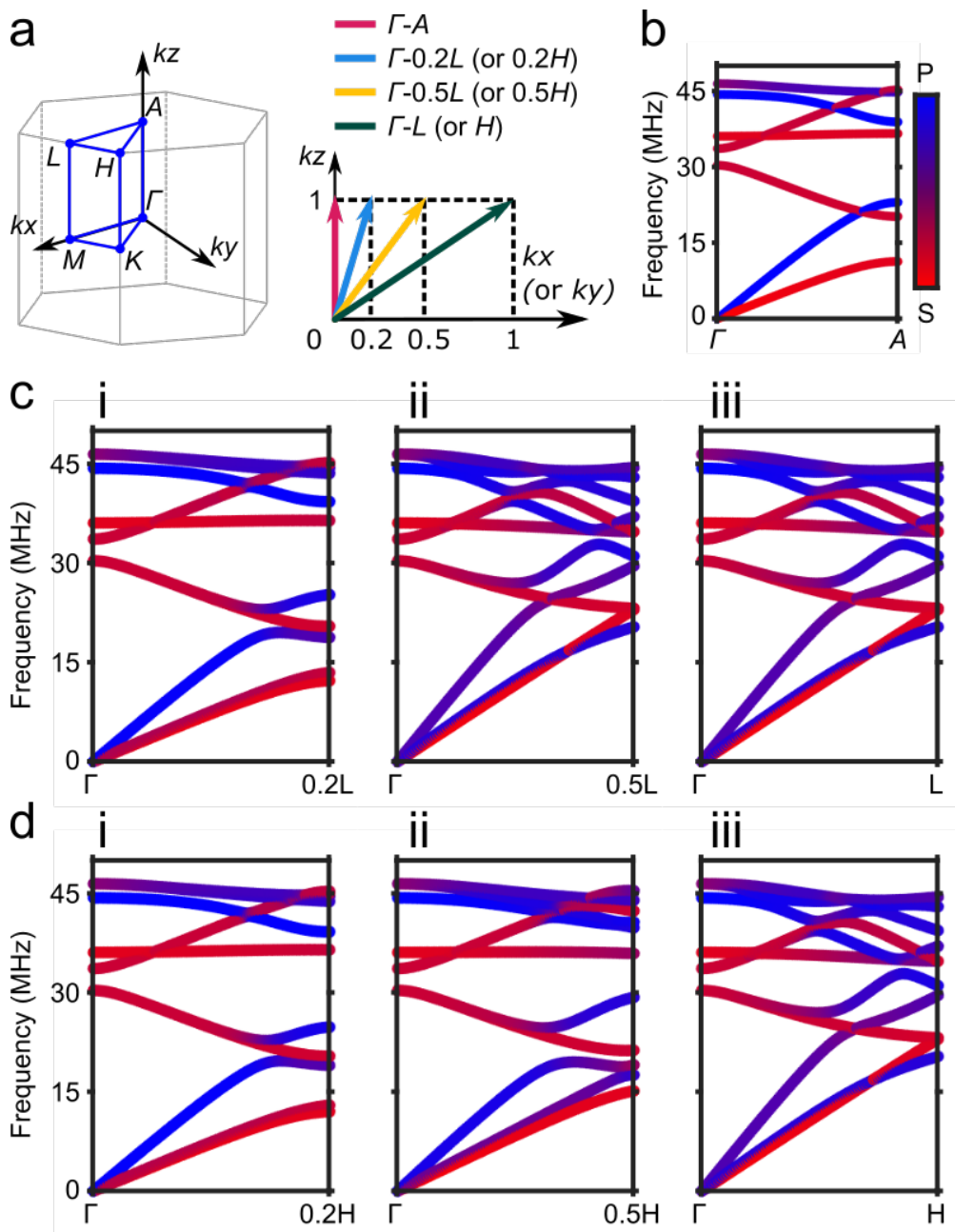


Figure 5.11: Angle-dependent dispersion curves of the metaskull. **a**, Wavevectors of the plane waves are shown with respect to the irreducible Brillouin zone of the honeycomb unit cell. **b**, The dispersion curve in the $\Gamma - A$ direction, parallel to the z -axis. **c**, The dispersion curves of the plane waves with gradually increased tilting against the z -axis toward the x -axis, and **d**, toward the y -axis.

Transmission simulation: Angle-dependent dispersion curves within the Brillouin zone

fUSI is based on the ultrafast transmission of plane acoustic waves in tissues to capture subtle blood flow changes caused by neurovascular coupling. To achieve maximum contrast, coherent compounding of tilted plane-waves was performed [59]. Typically for fUSI, four to ten angles between -10° to $+10^\circ$ are used to form a single coherently compounded image. We numerically investigated the sensitivity of the transmission performance of the metaskulls with respect to the incident angle of the plane acoustic waves (Fig. 5.12). We analyzed dispersion curves and transmission properties for various incident angles and directions of the incident waves front (Fig. 5.11). The incident angles were tilted in the xz -plane based on the Brillouin zone of a hexagonal lattice. Starting from $\Gamma - A$, the dispersion curves were computed with a gradually increasing incident angle toward the $\Gamma - L$ direction (Fig. 5.11a). With greater tilting angle, the longitudinal mode of the metaskulls gets more hybridized with the shear mode, making it less effective at transmitting the acoustic wave energy. We observe that the original dispersion behavior in $\Gamma - A$ remains relatively unchanged until $\Gamma - 0.2L$, which corresponds to a 14.8° tilting. Different angle-dependent responses between the metaskull models of different thickness is attributed to Bragg scattering. We quantitatively evaluated the angle-dependent attenuation using the transmission simulation at 15 MHz. The transmission curve of the 4-unit-cell metaskulls is almost flat up to 14.8° with only 0.16 dB reduction from 0° , but the curve shows steep decrease to -2.55 dB at 30° and to -5.81 dB at 40° (Fig. 5.12).

We investigated the effects of the incident angle and direction of the plane acoustic waves on the dispersion curves of the metaskulls (Fig. 5.11). The wavevectors of the incident waves follow the Brillouin zone notation as shown in Figure 5.11a, and their angles with respect to the z -axis are tabulated in Table 5.3. For example, $\Gamma - 0.2L$ corresponds to the wavevectors parallel to the vector from the point Γ to the point on the line $A-L$ splitting the line with 2:8 ratio. Up to $\Gamma - 0.2L$ and $\Gamma - 0.2H$, which correspond to 14.80° and 12.89° , respectively, the main design features of the dispersion curves at $\Gamma - A$ remain (Fig. 5.11b,c(i),d(i)). There exists a pure longitudinal mode which stays dispersionless, and the shear band gap opening from 13.48 to 20.49 MHz (or 12.98 to 20.42 MHz) can be observed at $\Gamma - 0.2L$ (or $\Gamma - 0.2H$). As the incident angle gets larger for both directions, the shear band gap narrows and shifts upwards, and the hybridized mode between the pressure mode and the shear mode emerges (Fig. 5.11c(ii),d(ii)). As the direction

vectors reach the edge of the Brillouin zone, the shear band gap completely closes and the pressure mode becomes dispersive (Fig. 5.11c(iii),d(iii)). The energy of the traveling longitudinal waves will be attenuated, while part of the energy will be converted to shear mode due to the hybridized mode. To conclude, the acoustic characteristics of the dispersion curves at $\Gamma - A$ stay undisturbed up to 13° , allowing wider angle for functional ultrasound examination.

Transmission: The frequency band gap and transmission as a function of the incident angle

We evaluated the transmission models and their pressure profiles as functions of wave propagating directions in the Brillouin zone at $f = 15$ MHz. As the incident pressure waves get more tilted with respect to the vertical axis, the amplitude of transmitted waves get more attenuated. The amount of transmission loss remains relatively constant until the incident angle reaches 15° , but increases dramatically as the incident angle gets larger (Fig. 5.12). The angle-dependent attenuation of the metaskull is due to the emergence of the hybridized mode and vanishing shear band gap with greater incident angle.

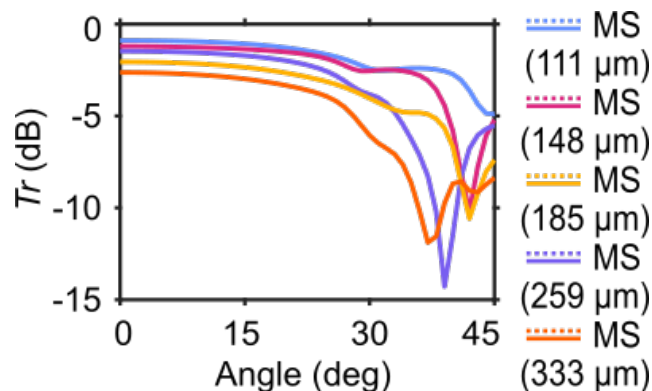


Figure 5.12: Angle-dependent transmission curves of the metaskull. Numerically calculated transmission curves of the metaskull with different number of layers at 15 MHz with respect to the incident angle of the pressure waves in $\Gamma - 0.2L$ direction.

Acoustic transmission experiments with the metaskull samples

We used zero-padded, Hann-windowed single-cycle sinusoidal bursts as the input waves for the underwater transmission tests. The signals centered at multiple different frequencies were sent through the metaskull samples using an immersion transducer (Olympus, V356-SU). The output signals were recorded by a hydrophone (Precision Acoustics, 0.2 mm needle) and Fourier-transformed for the evaluation in

Wavevector	θ ($^\circ$)	f_c (MHz)	Δf (MHz)	Tr. (dB)
$\Gamma - A$	0	15.79	8.89	-2.63
$\Gamma - 0.2L$	14.80	16.99	7.01	-2.97
$\Gamma - 0.5L$	33.45	-	-	-7.25
$\Gamma - L$	52.88	-	-	-8.05
$\Gamma - 0.2H$	12.89	16.70	7.44	-2.88
$\Gamma - 0.5H$	29.78	0	-	-5.60
$\Gamma - H$	48.85	0	-	-7.92

Table 5.3: Wavevectors in the Brillouin zone, corresponding angles, and the resulting transmission characteristics. A The wavevectors in the hexagonal irreducible Brillouin zone and the corresponding incident angles of the plane acoustic waves. The center frequency, f_c , and the bandwidth, Δf , are acquired from the dispersion curves in Fig. 5.11. The transmission coefficients are derived from the FE transmission models with 9-unit-cell metaskulls (Fig. 5.12).

the frequency domain. We plotted the transmission coefficients of the metaskulls with varying thickness (111, 148, 175, 259, and 333 μm) and a PMP film (125 μm) in Fig. 5.7b.

5.6 In vivo experiments for cranial window characterization

Animal surgeries for in vivo experiments

To validate the fitness of the metaskulls as a skull prosthesis to perform high sensitivity fUSI, we conducted in vivo imaging studies using a total of 6 mice. We tested four mice to compare the SNR performance of the power Doppler images of the brain through two types of cranial windows of varying thickness (Fig. 5.13), and two for the longitudinal monitoring of fUSI performance after cranial implantation of the metaskulls (Fig. 5.14).

All animal experiments were conducted under protocols approved by the Institutional Animal Care and Use Committee of the California Institute of Technology. The in vivo experiments presented were performed on C57BL/6J mice (Jackson Laboratory) aged between 6 to 8 weeks. No randomization or blinding were necessary in this study.

Side-by-side comparison of different skull replacement material

Four mice were used for the cranial window characterization study. Mice were anesthetized with 2–3% isoflurane with their heads fixed on a stereotaxic frame. After the incision and stabilization of the skin, the skull was exposed and rinsed with sterile saline. Ultrasound coupling gel is applied on top of the skull, then we

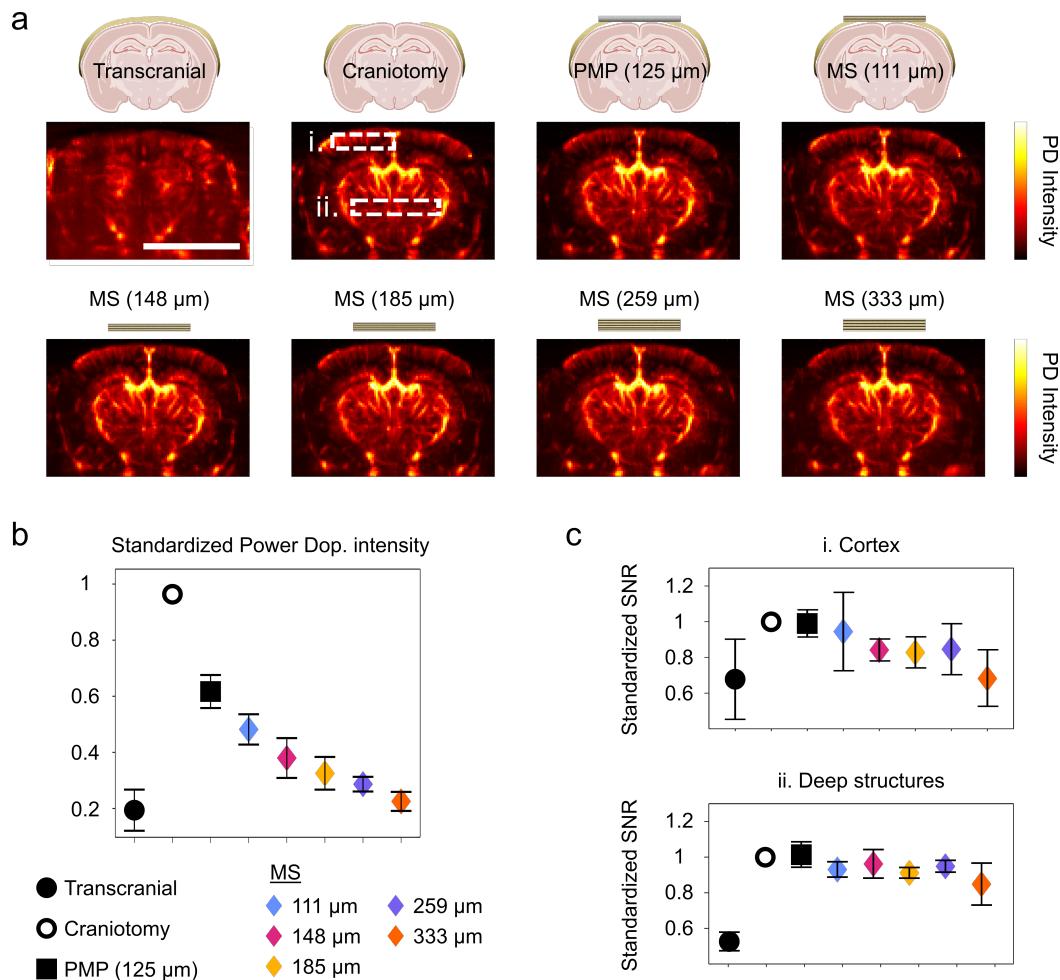


Figure 5.13: Side-by-side comparison of different skull replacement material for high sensitive cerebral power Doppler imaging in mice (N = 4). **a**, Cerebral power Doppler imaging of one mouse through the intact skull, after craniotomy without any material, and through a layer of PMP (125 μm) or metaskulls (111, 148, 185, 259, and 333 μm) (Representative mouse). **b**, Standardized total intensity of the power Doppler images with respect to the skull replacement material. **c**, Standardized SNR of the power Doppler in i. the cortex and ii. the deeper structures. Scale bar: 5mm. PD = Power Doppler.

acquired a first transcranial power Doppler image set (“Transcranial” case in Fig. 5.13a) following the parameters described in the fUSI acquisition section. A skull window (1 cm x 0.4 cm) was then removed by drilling (Foredom) at low speed using a micro drill steel burr (Burr number 19007-07, Fine Science Tools). Care was taken not to damage the dura and to prevent inflammatory processes in the brain. We acquired a second transcranial power Doppler image set where only ultrasound coupling gel is applied on top of the brain (“Craniotomy” case in Fig. 5.13a). Then, successive implant sheets for PMP and metaskull cases were positioned on top of

the brain for additional power Doppler acquisitions.

Surgical implantation of honeycomb lattices for chronic imaging of the brain in mice

Two mice were implanted with the metaskull and used for the longitudinal study. Mice were anesthetized with 2%–3% isoflurane, with their heads fixed on a stereotaxic frame. After the incision and stabilization of the skin, we removed a rectangular skull window (1 cm x 0.4 cm) by drilling at low speed using a micro drill steel burr. The window corresponds to the coronal planes from Bregma -2 mm to Bregma -2.5mm. Care was taken not to damage the dura and to prevent inflammatory processes in the brain. We dropped 20 μ l of artificial dura on top of the exposed brain to provide an aqueous layer between the brain tissue and the implant. A 1 cm x 0.5 cm metaskull window was sealed in place with the layer of acrylic resin. The surgical procedure took 45 min to 1 h. Animals recovered quickly, and after a conservative 10 days resting period, they were used for the data acquisition via fUSI.

fUSI acquisition

fUSI visualizes neural activity by mapping local changes in cerebral blood volume (CBV). CBV variations are tightly linked to neuronal activity through the neurovascular coupling and are evaluated by calculating power Doppler variations in the brain. fUSI was performed using a 15 MHz ultrasonic prob (L22-14vX, 15 MHz, 64 elements, 0.11 mm pitch, Verasonics) connected to a Verasonics Vantage ultrasound system (Verasonics) driven by custom MATLAB (MathWorks) transmission scripts. Each power Doppler image was obtained from the temporal integration of 300 compounded frames acquired at 500 Hz frame rate, using 5 tilted plane waves separated by 3° (-6°, -3°, 0°, 3°, and 6°) acquired at a 2,500 Hz pulse repetition frequency. Power Doppler images were then repeated every second (1 Hz image framerate). Each block of 300 images was processed using a SVD clutter filter to separate tissue signal from blood signal to obtain a final power Doppler image exhibiting CBV in the whole imaging plane.

SNR performance through different material and thicknesses shows the transmission characteristics

We first acquired a transcranial cerebral power Doppler image in anesthetized mice as a reference. We then performed a craniotomy to open a cranial window and to compare the fUSI performance through different skull replacement materials. The

metaskulls with varying thickness and a PMP film (125 μm) were positioned on top of the brain to cover the cranial opening. The size of the metaskull windows was 1 cm x 0.25 cm, consisting of 75,000 honeycomb unit cells per layer. All power Doppler images were acquired on the same coronal plane for all conditions (Bregma -2.5mm).

The standardized intensity maps obtained from the power Doppler using different types of windows were plotted side by side (Fig. 5.13a). We could observe the strong attenuation of the transcranial power Doppler signal relative to the image acquired after craniotomy. The main arteries were indiscernible, also showing poor in-depth signal. Without any covering after craniotomy, cortical vessels were clearly visible, as well as the deeper vessels in the thalamic regions. We then covered the brain with a PMP film or the metaskulls with different thickness, and no clear structural change from the acquired images was noticeable. The average intensity in the power Doppler images was the highest in the case of craniotomy and the lowest in the transcranial case (Fig. 5.13b). Taking the intensity from the craniotomy as a reference, the PMP case recovered 60% of the reference intensity, while the metaskulls showed gradual decrease from 50% (111 μm) to 20% (333 μm) of the reference intensity with increasing thickness.

We quantitatively assessed the signal sensitivity of the ultrasound images through the metaskulls by analyzing the SNR of the acquired blood vessel mappings. The normalized SNR in cortical regions and in deeper structures (defined by the white-dotted squares in Fig. 5.13a) are shown for all the cases (transcranial, craniotomy, PMP, and the metaskulls) (Fig. 5.13c). The transcranial SNR was evaluated as a reference, and one can again observe a major loss in SNR in the transcranial case (70% of the craniotomy signal in the cortical region, and 45% in the deeper structures). The SNR obtained after covering the brain with a PMP window was almost 95% of the craniotomy SNR, both in the cortical and deeper regions. Similarly, the metaskull only caused a slight decrease in SNR for the thinner case (92% at 111 μm) for both cortical and deeper structures, while the SNR gradually decreased to 70% as the thickness of the metaskull increased to 333 μm .

We showed that the metaskull induces more than 50% decrease in intensity (this decrease is around 40% for the PMP film) compared to the craniotomy case in the power Doppler images, but that the SNR remained above 80% of the craniotomy SNR.

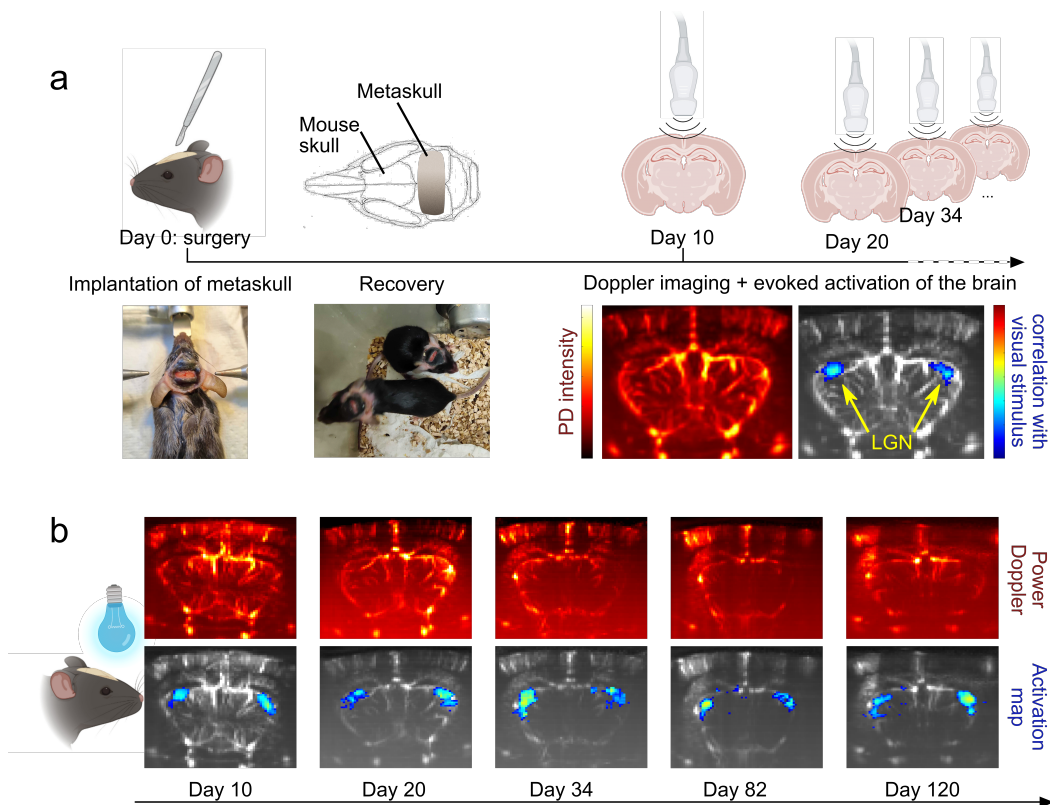


Figure 5.14: Longitudinal fUSI study in mice after metaskull implantation. a, Longitudinal study protocol: mice are implanted with the metaskull (148 μm) at day 0. They are then examined at day 10, 20, 34, . . . during which visually evoked activity is recorded. **b,** Power Doppler images are acquired around coronal plane B-2.2 mm showing the structure of the vascular network (top, hot colors) and the activated LGN following visual stimulation (bottom, cold colors)

5.7 Survival test

Longitudinal study confirms biocompatibility and functional signal conservation over time

We surgically implanted the metaskull in mice ($N = 2$) to evaluate the biocompatibility of the constituent polymer, and the conservation of the functional signal through the implant over a long period of time was observed (> 4 months). Power Doppler scans were performed at days 10, 20, 34, 82 and 120 after surgery, during which we stimulated the visual system to measure evoked activation in the lateral geniculate nuclei (LGN).

Functional activation of mice visual system

To evaluate the sensitivity of fUSI through the metaskull long-term, we stimulated the visual system of the metaskull-implanted mice over multiple days (day 10, 20,

34, . . .). We delivered visual stimuli using a blue LED positioned at 3 cm in front of the eyes of the mice. Stimulation runs consisted of periodic flickering of the blue LED using the following parameters: 30 s of rest followed by 30 s of a flicker.

Activation maps

Correlation maps were computed individually from the normalized correlation between each pixel's temporal signal with the visual stimulus patterns (Pearson's product moment) using MATLAB (MathWorks). At day 10 after the implantation, the power Doppler scan allowed visualization of the brain vessels with great sensitivity from the cortex all the way down to the amygdala. Visually evoked response was clearly visible as the two LGN were activated, which led to a higher volume of blood to flow. Throughout the study, the degradation of the power Doppler signal was observed, resulting in a shallower distinction of the blood vessels in the deeper structures (see Fig. 5.13 for definition of the deep structures). However, the activation of both LGN was distinguishable throughout the whole functional study from day 10 to day 120 with more than 50% correlation with the stimulation pattern.

5.8 Conclusions

In this chapter, we successfully implanted rationally designed acoustic metamaterials to living animals for ultrasound imaging. The proposed metamaterial cranial window, "Metaskull", allows for fUSI in small animal brains with long-term stability and lasting signal sensitivity over more than 100 days. The metamaterials' inner geometry was architected so that the metaskull can accomplish minimally attenuative transmission of ultrasonic waves at 15 MHz. At the same time, the stiffness of the metaskull reaches its theoretical limit, providing a robust protection layer to the brain. Our approach transcends other widely used materials for cranial windows, e.g., PMP, since complex shapes and curvatures of the skull can be easily duplicated with microscale additive manufacturing. The conformal metaskulls can replace any sections of skull geometry, which is impossible to accomplish with PMP films' inherent planar shape. Several limitations must be addressed in future studies to establish the wider applicability of the metaskulls as cranial windows for ultrasound brain imaging. First, drainage holes must exist due to the current 2PP fabrication process, which reduces the effective stiffness and may undermine the structural integrity of the metaskull. Advanced 3D printing technology, such as direct ink writing or mid-air 3D printing, that do not need photoresist and support materials can be further improved to solve the issue. In addition, the viscoelastic

attenuation from the constituent polymer can be reduced with pyrolysis, allowing the polymer to carbonize and form brittle structures. Pyrolyzed lattices would provide enhanced protection from external mechanical forces with increased stiffness. Further exploration should aim at incorporating functionalities to the metaskulls, which will make the metamaterial acoustic window more versatile for biomedical applications. The directions of research may involve the development of the metaskulls for ultrasonic wave focusing enabled by transformation acoustics [60], enhanced photoacoustic imaging for the brain [61], or acoustic wave front shaping for clearer images [62]. For example, local acoustic characteristics required to manipulate incident ultrasonic waves can be determined with transformation acoustics approach, so that the dimensions of the unit cells can be tuned to achieve desired properties and purpose.

References

1. Macé, E. *et al.* Functional ultrasound imaging of the brain. *Nature Methods* **8**, 662–664 (2011).
2. Deffieux, T., Demené, C. & Tanter, M. Functional Ultrasound Imaging: A New Imaging Modality for Neuroscience. *Neuroscience. Brain imaging* **474**, 110–121 (2021).
3. Rubin, J. M., Bude, R. O., Carson, P. L., Bree, R. L. & Adler, R. S. Power Doppler US: a potentially useful alternative to mean frequency-based color Doppler US. *Radiology* **190**, 853–856 (1994).
4. Gesnik, M. *et al.* 3D functional ultrasound imaging of the cerebral visual system in rodents. *NeuroImage* **149**, 267–274 (2017).
5. Bimbard, C. *et al.* Multi-scale mapping along the auditory hierarchy using high-resolution functional UltraSound in the awake ferret. *eLife* **7**, e35028 (2018).
6. Norman, S. L. *et al.* Single-trial decoding of movement intentions using functional ultrasound neuroimaging. *Neuron* **109**, 1554–1566.e4 (2021).
7. Imbault, M., Chauvet, D., Gennisson, J.-L., Capelle, L. & Tanter, M. Intra-operative Functional Ultrasound Imaging of Human Brain Activity. *Scientific Reports* **7**, 7304 (2017).
8. Baranger, J. *et al.* Bedside functional monitoring of the dynamic brain connectivity in human neonates. *Nature Communications* **12**, 1080 (2021).
9. Aydin, A.-K. *et al.* Transfer functions linking neural calcium to single voxel functional ultrasound signal. *Nature Communications* **11**, 2954 (2020).

10. Sieu, L.-A. *et al.* EEG and functional ultrasound imaging in mobile rats. *Nature Methods* **12**, 831–834 (2015).
11. Urban, A. *et al.* Real-time imaging of brain activity in freely moving rats using functional ultrasound. *Nature Methods* **12**, 873–878 (2015).
12. Rabut, C. *et al.* PharmacofUS: Quantification of pharmacologically-induced dynamic changes in brain perfusion and connectivity by functional ultrasound imaging in awake mice. *NeuroImage* **222**, 117231 (2020).
13. Krishna, V., Sammartino, F. & Rezai, A. A Review of the Current Therapies, Challenges, and Future Directions of Transcranial Focused Ultrasound Technology: Advances in Diagnosis and Treatment. *JAMA Neurology* **75**, 246–254 (2018).
14. Pinton, G. *et al.* Attenuation, scattering, and absorption of ultrasound in the skull bone. *Medical Physics* **39**, 299–307 (2012).
15. Urban, A. *et al.* Chronic assessment of cerebral hemodynamics during rat forepaw electrical stimulation using functional ultrasound imaging. *NeuroImage* **101**, 138–149 (2014).
16. Bergel, A., Deffieux, T., Dmené, C., Tanter, M. & Cohen, I. Local hippocampal fast gamma rhythms precede brain-wide hyperemic patterns during spontaneous rodent REM sleep. *Nature Communications* **9**, 5364 (2018).
17. Schaedler, T. A. *et al.* Ultralight Metallic Microlattices. *Science* **334**, 962–965 (2011).
18. Berger, J. B., Wadley, H. N. G. & McMeeking, R. M. Mechanical metamaterials at the theoretical limit of isotropic elastic stiffness. *Nature* **543**, 533–537 (2017).
19. Crook, C. *et al.* Plate-nanolattices at the theoretical limit of stiffness and strength. *Nature Communications* **11**, 1579 (2020).
20. Martínez-Sala, R. *et al.* Sound attenuation by sculpture. *Nature* **378**, 241 (1995).
21. Ma, G. & Sheng, P. Acoustic metamaterials: From local resonances to broad horizons. *Science Advances* **2**, e1501595 (2016).
22. Cummer, S. A., Christensen, J. & Alù, A. Controlling sound with acoustic metamaterials. *Nature Reviews Materials* **1** (2016).
23. Liu, Z. *et al.* Locally Resonant Sonic Materials. *Science* **289**, 1734–1736 (2000).
24. Shen, C., Xu, J., Fang, N. X. & Jing, Y. Anisotropic Complementary Acoustic Metamaterial for Canceling out Aberrating Layers. *Physical Review X* **4**, 041033 (2014).

25. Craig, S. R., Welch, P. J. & Shi, C. Non-Hermitian complementary acoustic metamaterials for lossy barriers. *Applied Physics Letters* **115**, 051903 (2019).
26. Craig, S. R., Welch, P. J. & Shi, C. Non-Hermitian Complementary Acoustic Metamaterials for Imaging Through Skull With Imperfections. *Frontiers in Mechanical Engineering* **6** (2020).
27. Wang, J., Allein, F., Boechler, N., Friend, J. & Vazquez-Mena, O. Design and Fabrication of Negative-Refractive-Index Metamaterial Unit Cells for Near-Megahertz Enhanced Acoustic Transmission in Biomedical Ultrasound Applications. *Physical Review Applied* **15**, 024025 (2021).
28. Li, Y., Liang, B., Zou, X.-y. & Cheng, J.-c. Extraordinary acoustic transmission through ultrathin acoustic metamaterials by coiling up space. *Applied Physics Letters* **103**, 063509 (2013).
29. Park, J. J., Lee, K. J. B., Wright, O. B., Jung, M. K. & Lee, S. H. Giant Acoustic Concentration by Extraordinary Transmission in Zero-Mass Metamaterials. *Physical Review Letters* **110**, 244302 (2013).
30. Lee, S. H., Park, C. M., Seo, Y. M., Wang, Z. G. & Kim, C. K. Acoustic metamaterial with negative modulus. *Journal of Physics: Condensed Matter* **21**, 175704 (2009).
31. Fleury, R. & Alù, A. Extraordinary Sound Transmission through Density-Near-Zero Ultranarrow Channels. *Physical Review Letters* **111**, 055501 (2013).
32. Zhang, X. Acoustic resonant transmission through acoustic gratings with very narrow slits: Multiple-scattering numerical simulations. *Physical Review B* **71**, 241102 (2005).
33. Lu, M.-H. *et al.* Extraordinary Acoustic Transmission through a 1D Grating with Very Narrow Apertures. *Physical Review Letters* **99**, 174301 (2007).
34. D'Aguanno, G. *et al.* Broadband metamaterial for nonresonant matching of acoustic waves. *Scientific Reports* **2**, 340 (2012).
35. Xie, Y., Konneker, A., Popa, B.-I. & Cummer, S. A. Tapered labyrinthine acoustic metamaterials for broadband impedance matching. *Applied Physics Letters* **103**, 201906 (2013).
36. Chen, H. & Chan, C. T. Acoustic cloaking in three dimensions using acoustic metamaterials. *Applied Physics Letters* **91**, 183518 (2007).
37. Zhang, S., Xia, C. & Fang, N. Broadband Acoustic Cloak for Ultrasound Waves. *Physical Review Letters* **106**, 024301 (2011).
38. Yang, S. *et al.* Focusing of Sound in a 3D Phononic Crystal. *Physical Review Letters* **93**, 024301 (2004).
39. Ambati, M., Fang, N., Sun, C. & Zhang, X. Surface resonant states and super-lensing in acoustic metamaterials. *Physical Review B* **75**, 195447 (2007).

40. Bloomfield, P., Lo, W.-J. & Lewin, P. Experimental study of the acoustical properties of polymers utilized to construct PVDF ultrasonic transducers and the acousto-electric properties of PVDF and P(VDF/TrFE) films. *IEEE Transactions on Ultrasonics, Ferroelectrics, and Frequency Control* **47**, 1397–1405 (2000).
41. Madsen, E. L., Deaner, M. E. & Mehi, J. Properties of Phantom Tissue-like Polymethylpentene in the Frequency Range 20–70 MHz. *Ultrasound in Medicine & Biology* **37**, 1327–1339 (2011).
42. Demené, C. *et al.* 4D microvascular imaging based on ultrafast Doppler tomography. *NeuroImage* **127**, 472–483 (2016).
43. Koekkoek, S. *et al.* *High Frequency Functional Ultrasound in Mice in 2018 IEEE International Ultrasonics Symposium (IUS)* (2018), 1–4.
44. Rahal, L. *et al.* Ultrafast ultrasound imaging pattern analysis reveals distinctive dynamic brain states and potent sub-network alterations in arthritic animals. *Scientific Reports* **10**, 10485 (2020).
45. Brunner, C. *et al.* Whole-brain functional ultrasound imaging in awake head-fixed mice. *Nature Protocols* **16**, 3547–3571 (2021).
46. Edelman, B. J. *et al.* High-sensitivity detection of optogenetically-induced neural activity with functional ultrasound imaging. *NeuroImage* **242**, 118434 (2021).
47. Réaux-Le-Goazigo, A. *et al.* Ultrasound localization microscopy and functional ultrasound imaging reveal atypical features of the trigeminal ganglion vasculature. *Communications Biology* **5**, 1–11 (2022).
48. Tournissac, M. *et al.* Cranial window for longitudinal and multimodal imaging of the whole mouse cortex. *Neurophotonics* **9**, 031921 (2022).
49. Wadley, H. N. Multifunctional periodic cellular metals. *Philosophical Transactions of the Royal Society A: Mathematical, Physical and Engineering Sciences* **364**, 31–68 (2006).
50. Moussi, K., Bukhamsin, A., Hidalgo, T. & Kosel, J. Biocompatible 3D Printed Microneedles for Transdermal, Intradermal, and Percutaneous Applications. *Advanced Engineering Materials* **22**, 1901358 (2020).
51. Krödel, S. & Daraio, C. Microlattice Metamaterials for Tailoring Ultrasonic Transmission with Elastoacoustic Hybridization. *Physical Review Applied* **6**, 1–9 (2016).
52. Hashin, Z. & Shtrikman, S. A variational approach to the theory of the elastic behaviour of multiphase materials. *Journal of the Mechanics and Physics of Solids* **11**, 127–140 (1963).
53. Dance, D., Christofides, S., Maidment, A., McLean, I. & Ng, K. *Diagnostic Radiology Physics: A Handbook for Teachers and Students* (IAEA, 2014).

54. Manouchehrian, A., Kulatilake, P. H. S. W. & Wu, R. Failure Mechanism of Rock Specimens with a Notched Hole under Compression—A Numerical Study. *Applied Sciences* **11**, 7797 (2021).
55. Tian, Y., Shen, Y., Qin, X. & Yu, Z. Enabling the complete mode conversion of Lamb waves into shear horizontal waves via a resonance-based elastic metamaterial. *Applied Physics Letters* **118**, 014101 (2021).
56. Salahshoor, H., Shapiro, M. G. & Ortiz, M. Transcranial focused ultrasound generates skull-conducted shear waves: Computational model and implications for neuromodulation. *Applied Physics Letters* **117**, 033702 (2020).
57. Ashby, M. *Materials selection in mechanical design* (Elsevier, 2017).
58. Tang, Y. *et al.* Hybrid acoustic metamaterial as super absorber for broadband low-frequency sound. *Scientific Reports* **7**, 43340 (2017).
59. Montaldo, G., Tanter, M., Bercoff, J., Benech, N. & Fink, M. Coherent plane-wave compounding for very high frame rate ultrasonography and transient elastography. *IEEE Transactions on Ultrasonics, Ferroelectrics, and Frequency Control* **56**, 489–506 (2009).
60. Cummer, S. in *Acoustic Metamaterials* (ed Craster, R. V.) 197–218 (Springer, 2013).
61. Wang, L. V. & Hu, S. Photoacoustic Tomography: In Vivo Imaging from Organelles to Organs. *Science* **335**, 1458–1462 (2012).
62. Yaqoob, Z., Psaltis, D., Feld, M. S. & Yang, C. Optical phase conjugation for turbidity suppression in biological samples. *Nature Photonics* **2**, 110–115 (2008).

*Chapter 6***SUMMARY AND OUTLOOK****6.1 Summary**

In this thesis, I discussed periodic acoustic metamaterials and the acoustic waves propagating through them in 1D, 2D, and 3D. I designed helical acoustic metamaterials that support wave propagation in 1D to study their unique dynamic mechanical properties and corresponding dispersion curves. I found that dispersion curves provide essential information about the wave properties of the periodic acoustic metamaterials. Leveraging these findings, I designed an acoustic metamaterial device with a gradient refractive index that can control the wave propagation direction in 2D to focus waves. Acoustic metamaterials are exciting not only from an academic point of view, but also from a practical aspect, as I demonstrated their ability to provide the brain with a sonotransparent protective layer for accessible ultrasound brain imaging by studying wave propagation in 3D.

In Chapter 2, I introduced basic concepts for understanding periodic acoustic metamaterials. I derived the characteristic equations for the simple models, which are essential for the dispersion relation analysis and for understanding the acoustic properties the dispersion relation implies. The dispersion curves were plotted for the graphical representation of the dispersion relation in the irreducible Brillouin zone, and the physical entities obtained from the curves were explained, e.g., phase velocity, group velocity, band gap, and normal modes. I further showed that the same analysis can be made also for the acoustic metamaterials in higher dimensions.

In Chapter 3, I studied 1D wave propagation in helical acoustic metamaterials with varying centro-asymmetry. I perturbed the degree of centro-asymmetry of the metamaterials to study the hybridization between the normal modes and its influence to the band gap structure. I investigated the HMMs using a theoretical model based on the ladder-like mass-spring chain using the physical quantities derived from long-wave approximation. The analytical dispersion curve matched with the FE analysis results, showing that greater centro-asymmetry led to increased coupling stiffness between originally independent modes. Stronger coupling in centro-asymmetric HMMs created multiple longitudinal band gaps that would block wave propagation. I validated both dispersion curves by experimentally measuring the transmission

coefficient along the 3D-printed HMM samples.

In Chapter 4, I investigated water-saturated microlattice metamaterials that can control wave propagation in 2D. The understanding of normal modes and dispersion curves from the previous chapter proved useful for the analysis of elastoacoustic coupling within water-saturated metamaterials. To simplify the problem and accelerate the computation process, I implemented Biot theory to analyze the water-saturated poroelastic microlattices and studied their acoustic behavior underwater. Based on this understanding, I fabricated a GRIN Luneburg lens, which enables underwater ultrasound wave focusing, and demonstrated its performance experimentally. I made a prediction model based on the poroelastic theory prior to the lens fabrication to determine the acoustic properties and corresponding geometry of each unit cell. I showed that using the poroelastic theory for homogenization allows for the computationally cheaper and faster design of acoustic wave manipulation devices.

In Chapter 5, I studied 3D wave propagation through acoustic metamaterials to develop skull-like material for ultrasound transmission. I demonstrated that rationally designed acoustic metamaterials can be used as a cranial window for ultrasound brain imaging. I designed and fabricated a conformal cranial window made up of honeycomb plate-lattice unit cells using microscale additive manufacturing. The metamaterial cranial windows with varying thickness were characterized *in vivo* to test its transmission performance and compatibility. I further showed that the proposed metamaterial cranial window enables long-term (> 4 months) fUSI in living small animal's brains with lasting signal sensitivity. This metamaterial cranial window can transmit ultrasonic waves at 15 MHz with small attenuation, while providing a robust protection to the brain with its stiffness close to the theoretical limit.

6.2 Open questions and future work

The HMMs, shown in Chapter 2, have many unexplored parameters that may be of interest to the acoustic metamaterials community. They exhibit two degenerate rotational modes, which were only briefly mentioned in the thesis. These modes can lead to unusual acoustic behaviors, such as nonreciprocal wave propagation, similar to diodes for electric signals. The rotational modes have two distinct rotations, clockwise and counter-clockwise, that arise from the chirality of the HMMs. They admit identical eigenfrequency solutions at lower frequencies, but diverge as frequency increases (Fig. 3.2). For example, the second branch of the counter-clockwise

rotational mode of the right-handed HMMs stops at the edge of the Brillouin zone, creating a large forbidden band. On the other hand, the clockwise rotational mode continues to transmit waves at higher frequencies. This chirality-driven degeneracy can be applied to block polarized acoustic waves in certain directions, thereby achieving nonreciprocity.

It has been shown that the Luneburg lens can be designed based on the theory of poroelasticity to focus ultrasound waves underwater as shown in Chapter 4. Although the biomedical application of this poroelastic Luneburg lens was not demonstrated in the thesis, it has the potential to be highly beneficial when used inside the human body to focus pressure intensity. Ingestible sensors are pill-sized devices that can reside in the gastrointestinal tract for extended periods to perform their functions. They are intensively studied as they can record direct physiological information and provide immediate medical treatment [1, 2]. However, controlling and activating body-embedded devices can be challenging as it is difficult to pinpoint the exact location of the devices. Moreover, if the sensor has a specific directionality for input stimulation, the problem becomes more complex as both the position and pointing direction of the device must be precisely controlled. However, such precise control may not be necessary if an omni-directional Luneburg lens can be incorporated into the ingestible devices to easily accomplish ultrasound wave focusing and perform necessary functionality.

Medical ultrasound probes are designed to have similar acoustic impedance to water, which enables clinicians to acquire clear sonograms and achieve lossless transmission of ultrasound waves inside the human body. Water-based couplants, such as hydrogels, are widely used to fill a thin air interface between the probe and the human skin to enhance ultrasonic wave transmission. However, current water-based couplants can be cumbersome, as they can flow down and need to be cleaned, and easily dehydrate within a few hours, making them undesirable for long-term, deep organ therapy [3]. Novel ultrasonic metamaterials can be developed that conform to the abdominal skin to enable daily liver stimulation and long-term monitoring of kidney diseases in individuals with chronic metabolic disorders. These metamaterials can be impedance-matched to water to minimize interfacial wave reflection and be permanently reusable without dehydration, as they are composed of non-water-based polymers (e.g., acrylics, polystyrene, and polyurethanes). This approach can pave the way for home health monitoring through improved accessibility to portable ultrasonic devices and further incorporated into

biomedical applications that require focused ultrasound, such as ultrasonography [4] and sonochemistry [5, 6].

Several limitations of the current fabrication process can be further improved to enhance the performance of the metaskull, shown in Chapter 5. The presence of drainage holes undermines the mechanical integrity of the metaskull by reducing the mass of the wall that can withstand loading stress and by creating concentrated stress points that can initiate cracks within the structure. Research on more advanced 3D printing techniques that can fabricate such fine-tuned geometries without the need for residual photoresist and supporting structures is necessary. Additionally, the polymeric structure contributes to transmission loss due to viscoelastic attenuation generated from its polymer chains. Thermal decomposition, i.e., pyrolysis, of the acrylic polymer will create a structure with high stiffness and brittleness, which would contribute to the protection of the brain with increased structural integrity [7]. The properties and behaviors of architected materials can be tuned by making the metaskulls with functional materials that are encoded with temporal/spatial degrees of freedom. Changes in temperature and chemical environment, and variations in electromagnetic fields can stimulate desired responses and topological transformations [8–10]. By precisely creating complex geometries and local inhomogeneities, it is possible to design metamaterial cranial windows capable of ultrasonic wave focusing enabled by transformation acoustics [11], enhanced photoacoustic imaging for the brain [12], or acoustic wave front shaping for clearer images [13].

References

1. Yang, S.-Y. *et al.* Powering Implantable and Ingestible Electronics. *Advanced Functional Materials* **31**, 2009289 (2021).
2. Mau, M. M., Sarker, S. & Terry, B. S. Ingestible devices for long-term gastrointestinal residency: a review. *Progress in Biomedical Engineering* **3**, 042001. (2023) (2021).
3. Wang, C. *et al.* Bioadhesive ultrasound for long-term continuous imaging of diverse organs. *Science* **377**, 517–523 (2022).
4. Sanches, J. M., Laine, A. F. & Suri, J. S. *Ultrasound imaging* (Springer, 2012).
5. Suslick, K. S. Sonochemistry. *Science* **247**, 1439–1445 (1990).
6. Yasui, K. in *Theoretical and Experimental Sonochemistry Involving Inorganic Systems* (Springer Netherlands, 2011).
7. Portela, C. M. *et al.* Supersonic impact resilience of nanoarchitected carbon. *Nature Materials* **20**, 1491–1497 (2021).

8. Popa, B.-I., Shinde, D., Konneker, A. & Cummer, S. A. Active acoustic metamaterials reconfigurable in real time. *Physical Review B* **91**, 220303 (2015).
9. Baz, A. Active nonreciprocal acoustic metamaterials using a switching controller. *The Journal of the Acoustical Society of America* **143**, 1376–1384 (2018).
10. Vangelatos, Z., Komvopoulos, K. & Grigoropoulos, C. P. Regulating the mechanical behavior of metamaterial microlattices by tactical structure modification. *Journal of the Mechanics and Physics of Solids* **144**, 104112 (2020).
11. Cummer, S. in *Acoustic Metamaterials* (ed Craster, R. V.) 197–218 (Springer, 2013).
12. Wang, L. V. & Hu, S. Photoacoustic Tomography: In Vivo Imaging from Organelles to Organs. *Science* **335**, 1458–1462 (2012).
13. Yaqoob, Z., Psaltis, D., Feld, M. S. & Yang, C. Optical phase conjugation for turbidity suppression in biological samples. *Nature Photonics* **2**, 110–115 (2008).